Computations of Unsteady Forces and Moments for a Transonic Rotor with Jet Actuation

by

Thomas Hans Novacek

B.S. Aerospace Engineering
Embry-Riddle Aeronautical University, 1995

Submitted to the Department of Aeronautics and Astronautics in partial fulfillment of the requirements for the degree of

Master of Science in Aeronautics and Astronautics

at the

MASSACHUSETTS INSTITUTE OF TECHNOLOGY

February 1997

Author .....
Department of Aeronautics and Astronautics
January 24, 1997

Certified by .....
Edward M. Greitzer
H. Nelson Slater Professor of Aeronautics and Astronautics
Thesis Supervisor

Accepted by .....
Professor Jaime Peraire
Chairman, Department Graduate Committee

Computations of Unsteady Forces and Moments for a Transonic Rotor with Jet Actuation

by

Thomas Hans Novacek

Submitted to the Department of Aeronautics and Astronautics
on January 24, 1997, in partial fulfillment of the
requirements for the degree of
Master of Science in Aeronautics and Astronautics

Abstract

A study has been made of unsteady forces and moments on transonic axial compressor blades subjected to jet actuation. Jet velocities of 1.5 and 2.0 times the free-stream velocity and jet angles of ±45, ±30, ±15, and 0 degrees were examined. Computations were carried out using a two-dimensional unsteady Navier-Stokes solver (UNSFLO) and using a quasi-steady momentum analysis. For the cases examined, it is found that the unsteady axial and tangential forces were largest at a jet angle of +45 degrees and least at a jet angle of zero degrees. This was also true for the unsteady moments. A quasi-steady momentum analysis can be used if the unsteady exit flow angle is accurately known; in this problem this means within 1 degree.

Thesis Supervisor: Edward M. Greitzer
H. Nelson Slater Professor of Aeronautics and Astronautics

Acknowledgment

I am indebted to many here at MIT for their support, instruction, and guidance which has helped me to complete this research project. I had the opportunity to work together with so many skilled, intelligent, and dedicated people who were always willing to help others. Therefore, I would like to thank all of those who made this thesis possible.

My advisor, Professor Edward M. Greitzer, has helped me with my completion of this project, and I thank him very much for his encouragement, guidance, instructions, and advice which navigated me through this first research experiment. Simply the opportunity to work with him was more then I could have imagined.

In the GTL lab, I had many valuable assistant, supporting conversation, and laughs. A special thanks goes to John N. Chi, who helped me during the first stage of learning the computer program. Also I want to thank him for having always a time for me when computer problems occur.

Also, I would like to thank Karsten Fels, Yuri Guinart, Jason Hardin, Carol Hermann, Manfredd Maier, Stefan Machaczek, Erika Podest, Andres Ramirez, Steve Routon, Terence Tay, and Nathalie Wolf who kept a wonderful relationship over the two years that I am here at MIT. I love you all my friends.

A very special and cordial thanks goes to a professor at Embry-Riddle Aeronautical University, Paul Hermann. He made the few "rainy days" here at MIT also a valuable

experience with his continues interest and encouragement. Thank you very much for all the calls and the letters which I received when I needed them most!

Finally, I would like to acknowledge the part my family played in this work. My parents, Elfriede and Johann Novacek, and grandparents, Leopoldine and Egon Zehrau, have supported me in whatever endeavors I looked on. Also, my brother, Andreas, and his wife, Petra, have understood why I needed to do this education. I thank them with all my heart for believing in me and giving me the love, encouragement, and financial support for the stay here at MIT. Most of all, I am indebted to my wife, Liliany. She has been her with me through this whole project, the good times and the bad times, remembering me of what is really important in Life. I could not have done it without her, and for her love, kindness, emotions, patience, and support I thank her with all my heart. Now it is time to go back home, Brazil or Austria wherever our destiny brings us.

Abschließend möchte ich mich bei dem Sigfried Ludwig-Fonds herzlich bedanken für die Zuerkennung des Stipendium während meines Auslandstudiums.

Table of Contents

List of Figures

List of Tables

Nomenclature

A	area of rotor cascade (m^2)
C	axial chord of the rotor blade (m)
V	velocity of the fluid (m/sec)
C_p	coefficient of pressure
c_p	specific heat capacity under constant pressure (J/kgK)
c_v	specific heat capacity under constant volume (J/kgK)
D	amplitude of fractional velocity defect
$d_{1,2,3}$	shape function describing the form of the velocity defect
e	internal energy per unit mass
$\mathbf{F}$	vector of the forces exerted by the body on the fluid (N)
$\mathbf{F}_{viscous}$	vector of the total viscous forces exerted on the control surface (N)
$\mathbf{f}$	vector of the net body forces per unit mass exerted by the fluid (N)
F	scalar force (N)
$f(\,)$	function of ( )
$\|G\|$	harmonic amplitude
h_{st}	stream-tube thickness (m)
h	enthalpy per unit mass (m^2/sec^2)
$N(\eta)$	periodic saw-tooth function
p	pressure (N/m^2)
Pr	constant Prandtl number
R	gas constant (J/kgK)
S	pitch (m)

t	time (sec)
u	velocity component in x direction (m/sec)
v	velocity component in y direction (m/sec)
V	control volume (m^3)
V_{rel}	relative velocity (m/sec)
V_x	difference of maximum to minimum relative inflow velocity (m/sec)
WS	rotor wheel-speed (m/sec)
W_{wake}	wake width (m)
x	distance in x direction (m)
y	distance in y direction (m)

Greek Symbols

α	absolute jet angle (degrees)
β	relative angle (degrees)
γ	ratio of specific heat
κ	constant number for exit angle prediction (degrees)
μ_s	viscosity given by Sutherland's law
μ	dynamic viscosity coefficient ($kg/msec^2$)
ρ	density (kg/m^3)
τ_{ij}	stress components (N/m^2)
ω	passing frequency of the rotor blade row through a disturbed segment (rad/sec)
$\tilde{\omega}$	reduced frequency

subscript

1	inlet flow
2	exit flow
Fst	flux averaged and steady flow
n	n = 0 fundamental harmonic, n = 1 first harmonic,...
ndim	non-dimensioned

r	rotor
rel	relative
wake	wake value at inlet boundary
s	stator
x	axial
y	tangential

Chapter 1

Introduction

To control rotating stall in a high-speed axial compressor, Berndt developed a jet actuator at the MIT Gas Turbine Laboratory [1]. A schematic of the jet actuator is shown in Figure 1.1. When this actuation system is implemented in a high-speed compressor, a problem of concern is the mechanical and aerodynamical forces and moments of the rotor blades. This thesis addresses the unsteady effects of a jet actuation on high-speed axial compressor blades in two dimensions by studying the axial forces, tangential forces, and moments of the rotor blades.

The following two sections give a background of the jet actuator and the unsteady flow calculation. After the background information, the objective, scope, and contribution of the research is presented followed by the outline of this thesis.

1.1 Information of Jet Actuator

Since compressor stages are being designed to operate closer to the upper limit of pressure rise, Epstein, Ffowcs-Williams, and Greitzer proposed in 1989 the idea of a dynamic-feed-back controlling system applied to turbomachine compressors which is documented in [3]. The objective is to sense small amplitude of perturbation in the compression system, apply a suitable control law with an actuation scheme, and extend the stable operating range of the machine, point B in Figure 1.4. As Figure 1.2 also indicates, the compressor surge line would

be moved to a lower mass flow by the implementation of this dynamic-feedback controlling system. Therefore, the stable operating range of the compression system would be extended to a higher pressure rise with an performance improvement. This new concept of controlling the compression system stability with its various application in turbomachine compressor evolved into the "Smart Engines: Concept and Application" at the MIT Gas Turbine Laboratory, documented in [4].

Many different actuation schemes have been developed to allow the pressure rise characteristic of an axial compressor to be altered. The scheme that is presented in this study is the jet injection upstream of the compressor. In general, a jet injection adds momentum and mass to the flow field that is upstream of the compressor blades. Also depending on the jet angle, the jet injection can result in a swirl upstream of the compressor blade. The three primary possibilities that allow the pressure rise characteristic of the compressor to alter are the change in mass flow, in upstream total pressure, and in upstream swirl. The first mechanism which changes the pressure rise is done by addition of mass flow through the jet injection. The second mechanism, which changes the pressure rise by changing the total pressure, is caused by the addition of axial momentum through the jet actuator. The third mechanism, which changes the pressure rise through changing the upstream swirl, is caused by the addition of tangential moment through the jet actuator.

1.2 Background of Unsteady Computation

There have been many attempts to understand and to compute the unsteady flow problem in the compression system. However, the 46th Propulsion and Energetics Panel Meeting of AGARD in 1975, and given in [4], marks a historical landmark for the computation and research of unsteady flow in compression systems. The first paper that was presented in [4] was a paper by Mikolajczak [5] who discussed the quasi-steady approximation to predict the stability margins of a compressor. It was concluded that for low reduced frequencies the compressors were expected to respond as the quasi-steady approximation, and for high values of reduced frequency it was concluded that the stability margin would be under predicted with the quasi-steady approximation.

The reduced frequency, as mentioned in the previous paragraph, is a parameter used to compare the time a fluid particle travels through the rotor passage to the time a rotor passes through a distorted segment of the flow. Therefore, the reduced-frequency parameter is defined by:

$$\tilde{\omega} \equiv \frac{\omega C}{V_x} \tag{1.1}$$

where ω is the passing frequency of the rotor blade row in units of rad/sec, C is the axial chord of the rotor-blade row, and V_x is the axial velocity of the fluid.

Two of the conclusions presented in [4] are directly relevant to the study presented in this thesis. These conclusions are the following:

- Unsteady flow has a strong impact on efficiency, aerodynamic stability, aero-elastic stability, and noise generation.
- Important contribution from unsteady flow occurs when the time scale for particle transport is comparable to the time scale of pressure fluctuations, which means a reduced frequency of order one.

1.3 Objective of Research

The objective of this research is to study the unsteady effects of a jet actuation on high-speed axial compressor blades. The results of this research are axial forces, tangential forces, and moments for different jet angles and jet velocities. A simple quasi-steady momentum analysis is also compared to the computed axial and tangential forces.

1.4 Scope of Research

The calculations carried out are for jet velocities of 1.5 and 2.0 times the free-stream velocity and jet angles of ±45, ±30, ±15, and 0 degrees at two radial positions, 88% span and 100% span. The jet velocities were chosen at these values since the jet actuation system of Berndt [1] injects a maximum jet-stream that is twice the free-stream velocity.

1.5 Contribution

Some of the contributions presented in this research are as following:

- Aerodynamic forces and moments on a rotor blade of a high-speed compressor subjected to a jet actuator with varying jet velocity and jet angle.
- Observation of axial pressure difference on a high-speed rotor blade as a function of jet velocity and jet angle.
- Development of a quasi-steady momentum analysis to predict the unsteady forces on a high-speed compressor blade.

1.6 Thesis Overview

The thesis is organized in the following manner:

Chapter 1: Introduction

Background, information, and concept of active feedback control with jet actuation is introduced. After this information, a short historical background of the computation of unsteady flow is given. This chapter ends with the presentation of the objective, scope, and contribution of this research.

Chapter 2: Numerical Procedure

The Computational Fluid Dynamic (CFD) program used for the numerical calculations is UNSFLO. This section describes the program. The rotor blade used was NASA Rotor Stage 35, documented in [6]. This section also gives the overall airfoil geometry, design parameters, and a comparison of the design performance with the lowest flow coefficient performance. At the inlet boundary of the compressor blade, the unsteady effects are caused by a jet actuation. Therefore, this section presents the velocity profile of an injector obtained in wind-tunnel testing for 100% span and 88% span and a comparison of the wind-tunnel result to the velocity profile used in the calculations.

Chapter 3: Quasi-Steady Momentum Analysis

This section describes a quasi-steady momentum analysis for forces and moments. A short discussion on the inlet flow parameters and exit flow parameters, and which parameters are prescribed for the quasi-steady momentum analysis, is also given. The section summarizes the assumptions needed to obtain the equations for computing the axial and tangential forces.

Chapter 4: Results and Discussion

The results of computed forces and moments are presented versus jet angle and reduced frequency. Comparisons are made with the quasi-steady model.

Chapter 5: Conclusions and Recommendations

A summary of the unsteady results is presented and recommendations for further work on unsteady loadings are given.

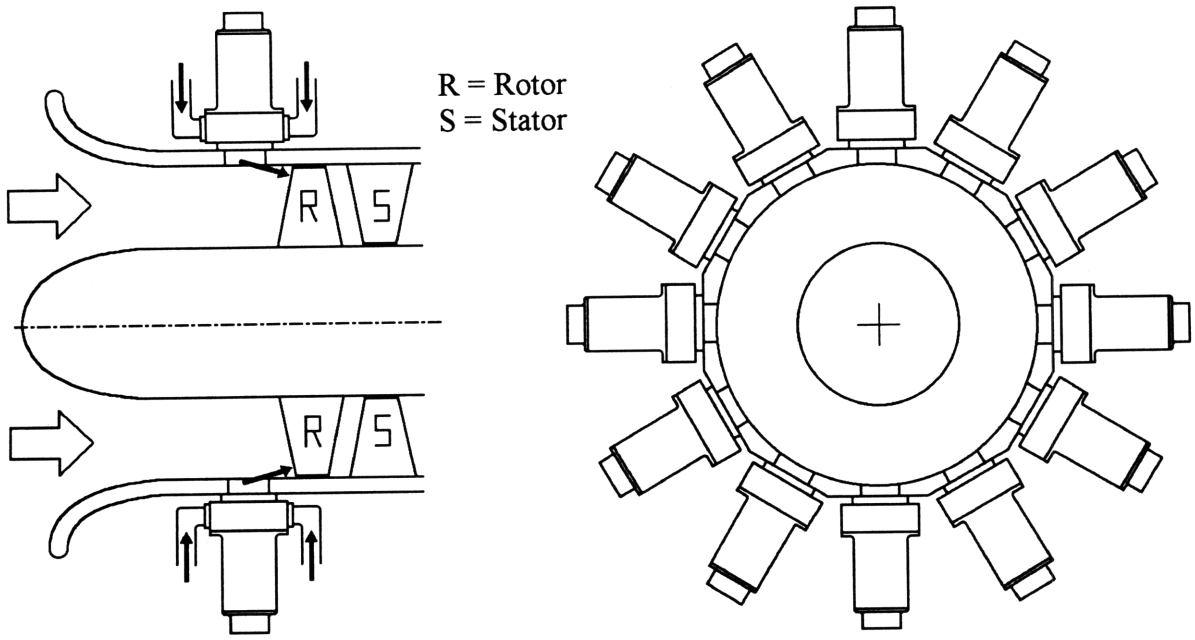

Figure 1.1: Schematic of the jet actuation in an axial compressor

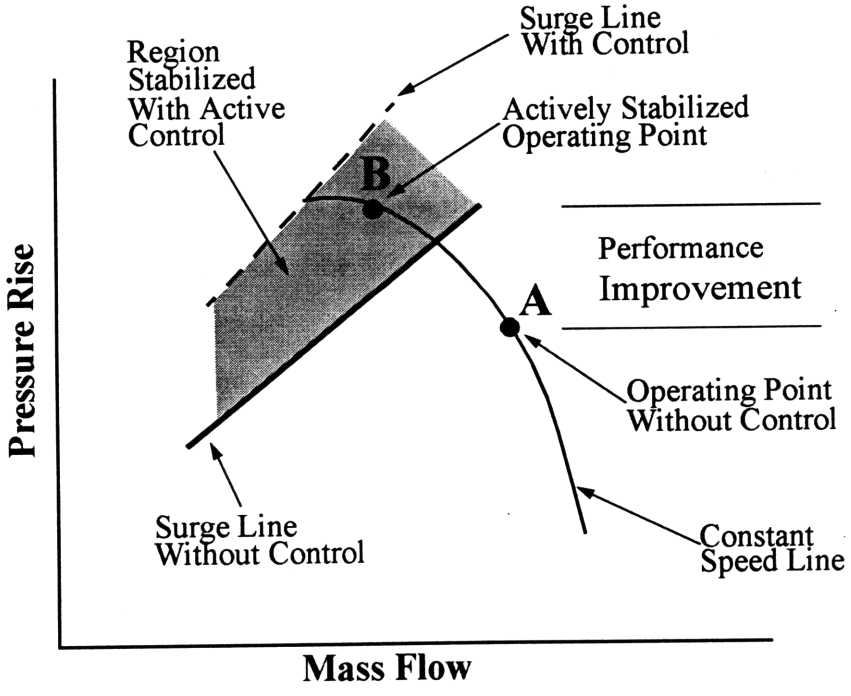

Figure 1.2: Performance improvement of the compression system through active compressor stabilization

Chapter 2

Numerical Procedure

The Computational Fluid Dynamic (CFD) program used to analyze the unsteady forces and moments on a rotor blade subjected to a jet actuation is UNSFLO, developed by Giles and documented in [7]. UNSFLO can treat steady and unsteady, inviscid or viscous, flows in two-dimensions or quasi three-dimensions. The general form of these governing equations of fluid motion are summarized in Appendix A. UNSFLO handles the following sources of unsteadiness:

- wake/rotor and potential/rotor interactions,
- stator/rotor interactions, and
- blade vibrations.

Several papers have been published on the algorithms in UNSFLO, and a user manual explaining the different parts of the program and the required inputs is found in [8]. There is also a comprehensive validation paper with a number of unsteady test cases collected in [9]. The non-dimensional analysis used in UNSFLO, the input variable needed for the computations, the file structure used by UNSFLO, and the programs needed to obtain the final plots of forces and moments used for this research are summarized in Appendix B.

A distinct feature of the code is the ability to treat arbitrary wake/rotor and stator/rotor ratios which can be computed on a multiple rotor passage. Another important feature is the non-reflecting boundary conditions, documented in [11], which minimizes non-physical

reflections at the inflow and outflow boundaries, and therefore, reduces the computational grid and time of computation.

The next two sections outline the salient features of the program to calculate and plot the unsteady forces and moments. After this description of the airfoil used for this analysis, the computational grid is given.

2.1 Computational Program: UNSFLO

UNSFLO uses an explicit Lax-Wendroff scheme to solve the two-dimensional unsteady and compressible Euler equations on an unstructured grid composed of triangles or quadrilateral cells. The Euler equations, presented in Appendix A as Equation (A.15) and (A.16), are reduced to their quasi three-dimensional form by including a varying streamtube thickness in the third dimension. The equations are

$$h_{st}\frac{\partial \mathbf{U}}{\partial t}+\frac{\partial (h_{st}\mathbf{F})}{\partial x}+\frac{\partial (h_{st}\mathbf{G})}{\partial y}-\mathbf{S}=\mathbf{0}, \tag{2.1}$$

where **U**, **F**, **G**, and **S** are four component vectors given by

$$\mathbf{U}=\begin{bmatrix}\rho\\ \rho u\\ \rho v\\ \rho e_t\end{bmatrix} \quad \mathbf{F}=\begin{bmatrix}\rho u\\ \rho u^2+p\\ \rho uv\\ (\rho e_t+p)u\end{bmatrix} \quad \mathbf{G}=\begin{bmatrix}\rho v\\ \rho vu\\ \rho v^2+p\\ (\rho e_t+p)v\end{bmatrix} \quad \mathbf{S}=\begin{bmatrix}0\\ p\frac{\partial h_{st}}{\partial x}\\ p\frac{\partial h_{st}}{\partial y}\\ 0\end{bmatrix}, \tag{2.2}$$

and h_{st} is the streamtube thickness. The pressure p is related to the total energy per unit mass e_t, density ρ, and velocity components u and v by

$$p=(\gamma-1)\rho\left[e_t-\frac{1}{2}(u^2+v^2)\right], \tag{2.3}$$

where a perfect gas with a constant specific heat ratio γ is assumed.

For the numerical solution of the unsteady Euler equations the Lax-Wendroff scheme is used. This Lax-Wendroff scheme is similar to that one used by Ni, documented in [12], but with the difference that UNSFLO can use a non-uniform grid. For a detailed derivation of the quadrilateral and triangular quasi three-dimensional Lax-Wendroff algorithm refer to [7].

The boundary condition at a solid wall allows no flow normal to the wall. The periodic boundary condition for steady and unsteady flow with the same stator and rotor pitch, S, is $\mathbf{U}(x, y, t) = \mathbf{U}(x, y + S, t)$, which states that the flow properties on one periodic boundary point is the same as the flow at the corresponding point on the other periodic boundary at the same time. When now the stator pitch is different from the rotor pitch or when a wake interacts with a rotor, then the inlet boundary condition satisfies a lagged periodic condition which is expressed by $\mathbf{U}(x, y, t) = \mathbf{U}(x, y + S_r, t + \Delta T)$. S_r is the rotor pitch, and the time lag, ΔT, is equal to the difference in pitches divided by the rotor wheel speed.

The interest here is in wake/rotor or jet/rotor interaction. The lagged periodic boundary condition is implemented in UNSFLO using a computational "time level" sloped in time. Mathematically this corresponds to coordinate transformation:

$$\begin{aligned} x' &= x \\ y' &= y \\ t' &= t - \left(\frac{\Delta T}{S_r}\right) y \end{aligned} \quad , \tag{2.4}$$

with the corresponding unsteady Euler equations resulting in

$$h_{st}\frac{\partial}{\partial t'}(\mathbf{U} - \lambda\mathbf{G}) + \frac{\partial (h_{st}\mathbf{F})}{\partial x'} + \frac{\partial (h_{st}\mathbf{G})}{\partial y'} - \mathbf{S} = \mathbf{0}, \tag{2.5}$$

where $\lambda = \Delta T / S_r$.

The non-reflecting far-field boundary conditions used are presented in [11]. These boundary conditions allow a far-field boundary location to be set closer to the rotor blades without affecting the flow in the neighborhood of the rotor blades. The approach is based upon the characteristics of the linearized Euler equations. For the algorithm implemented in UNSFLO

refer to [7], and for a formal derivation refer to [11]. The boundary condition for the unsteady incoming wake disturbance is presented in Section 2.2: Rotor Inlet Boundary Condition.

For many CFD programs the standard approach to viscous calculations is to use everywhere throughout the computational domain one numerical viscous algorithm. However, UNSFLO uses an alternative approach in which two numerical algorithms are used. The inviscid Lax-Wendroff algorithm as described earlier, and in a thin region around the blade the thin shear-layer approximation of the Navier-Stokes equations. (The size of thin region around the blade will be explained in Section 2.3.2: Computational Grid.) In this viscous region, UNSFLO uses an ADI algorithm, developed by Beam and Warming [13], but uses the upwind flux-difference splitting developed by Roe [14] to solve the Navier-Stokes equations to model the viscous effects within the boundary layers. The inviscid Lax-Wendroff algorithm, summarized in the previous paragraphs, is used for the rest of the fluid domain. The Navier-Stokes equations, presented in Appendix A as Equation (A.13) and (A.14), are reduced to their quasi three-dimensional form by including a varying streamtube thickness in the third dimension. The unsteady thin shear-layer approximation of the Navier-Stokes equations are

$$h_{st}\frac{\partial \mathbf{U}}{\partial t} + \frac{\partial (h_{st}\mathbf{F})}{\partial x} + \frac{\partial (h_{st}\mathbf{G})}{\partial y} - \frac{\partial (h_{st}\mathbf{V}_n)}{\partial n} - \mathbf{S} = \mathbf{0}, \tag{2.6}$$

where **U**, **F**, **G**, and **S** are the same as in the Euler equations, Equation (2.2), and $\mathbf{V}_n$ is the viscous flux vector given by

$$\mathbf{V}_n = \begin{bmatrix} 0 \\ \mu_s \dfrac{\partial u}{\partial n} \\ \mu_s \dfrac{\partial v}{\partial n} \\ \mu_s \dfrac{\partial}{\partial n}\left(\dfrac{1}{2}u^2 + \dfrac{1}{2}v^2 + \dfrac{1}{(\gamma-1)\,\mathrm{Pr}}c^2\right) \end{bmatrix}. \tag{2.7}$$

Pr is the constant Prandtl number, and μ_s is the viscosity given by the Sutherland law.

2.2 Rotor Inlet Boundary Condition

This research has a jet actuation as the unsteady disturbance, and the following subsections describe the wake models for the inflow velocity that can be specified in UNSFLO. A detailed description of the other unsteady boundary conditions can be found in [7]. The wake model chosen for this research is based on a review of experimental data taken by Berndt [1].

2.2.1 Wake Models from UNSFLO

The wake model that describes the shape of an incoming flow disturbance at the inflow boundary assumes that in the wake frame of reference the flow is parallel, the static pressure and total enthalpy are constant across the wake, and the prescribed velocity defect is a sinusoidal, Gaussian, or Hodson disturbance. These three flow disturbances can be modelled as

$$
\begin{aligned}
p_{wake} &= p_{Fst} \\
u_{wake} &= (1 - D \cdot d_{1,2,3})\, u_{Fst} \\
v_{wake} &= (1 - D \cdot d_{1,2,3})\, (v_{Fst} + V) \\
\rho_{wake} &= \frac{\gamma}{\gamma - 1} \frac{p_{Fst}}{h_t - \frac{1}{2}(u_{wake}^2 + v_{wake}^2)}
\end{aligned}
\qquad (2.8)
$$

where the subscript $_{wake}$ denotes the values of the wake at the inlet boundary and the subscript $_{Fst}$ gives the flux-averaged fluid flow values from steady calculation. D is the amplitude of the fractional velocity defect. The quantity $d_{1,2,3}$ is the shape function describing the form of the velocity defect. It is a function of $d(\eta)$ where η is defined as

$$
\eta = \left(y - \frac{v_{wake}}{u_{wake}} x \right) / S_{wake}, \qquad (2.9)
$$

where S_{wake} is the wake pitch. In general, two numbers identify the velocity disturbance: the maximum amplitude of the velocity defect, D, expressed as a fraction of the undisturbed velocity, and the width of the velocity defect, W_{wake} is the characteristic wake width expressed as a fraction of the pitch that generated the wake. For the width of the velocity defect there are three shape functions:

$$d_1(\eta) = \cos(2 \cdot \pi \cdot \eta)$$

$$d_2(\eta) = \exp\left(-\frac{N(\eta)^2}{2 \cdot W_{wake}^2}\right) \quad , \tag{2.10}$$

$$d_3(\eta) = \left\{max\left[0, 1 - \left(\frac{N(\eta)}{W_{wake}}\right)^{\frac{3}{2}}\right]\right\}^2$$

where $N(\eta)$ denotes the periodic saw-tooth function, shown in Figure 2.1.

2.2.2 Jet-Actuation Wake Model

As described in the previous section, three models have been proposed to simulate the unsteady effects of the incoming wake. These unsteady effects were obtained from wind-tunnel experiments, documented by Berndt [1], which measure the steady momentum-flux 63mm downstream of the injection center line, which corresponds to the compressor face location. The steady momentum-flux distribution for a sheet injector at maximum injection is shown in Figure 2.2 and the steady momentum-flux distribution for a three-hole injector at maximum injection is shown in Figure 2.3.

In Figures 2.2 and 2.3 the spatial axes correspond to the radial direction, from 0 to 80mm, and the circumferential direction, from -60 to 60mm, of the wind-tunnel which represent 1/12 of the annulus of area spanned by the jet actuator. In the circumferential direction, the jet extends about 70% of the annulus for both the sheet and the three-hole injection. In the radial direction, the jet extents about 15% of the annulus for the sheet injection and 40% of the annulus for the three hole injection. The maximum momentum flux ratio of the sheet injector is 4, indicating that the maximum jet velocity is about twice the free-stream velocity since the

momentum is proportional to the square of velocity. The maximum momentum flux ratio of the three-hole injection, however, is 2.2 which correspond to a velocity ratio of 1.5.

Since the sheet injection produces a higher velocity ratio than the three-hole injection, the velocity profiles generated by the sheet injection are used in the analysis of the aerodynamic forces and moments in this research. The velocity profiles at various radial locations for the sheet injector at maximum steady injection is given in Figure 2.4.

From Figure 2.4, it can be seen that a Gaussian wake model fits the wind-tunnel test results. As mentioned in Section 2.2.1: Wake Models from UNSFLO, two numbers identify the velocity disturbance which will be modeled by the Gaussian distribution: the maximum amplitude of the velocity defect, D, expressed as a fraction of the undisturbed velocity, and the characteristic wake width, W_{wake}, expressed as a fraction of the pitch that generated the wake. The Gaussian parameters required by UNSFLO for the two radial positions of 100% span and 88% span are given in Table 2.1 with the corresponding wake profile shown in Figure 2.5.

Radial Position	Amplitude of Velocity Defect, D		Characteristic Width, W_{wake}	
	for fractional wake velocity of 2.0	for fractional wake velocity of 1.5	for fractional wake velocity of 2.0	for fractional wake velocity of 1.5
100% span	-1.25	-0.75	0.19	0.19
88% Span	-1.05	-0.55	0.11	0.11

Table 2.1: Parameters for the Gaussian wake profile used in UNSFLO

The dashed lines in Figure 2.5 are the Gaussian distribution, and the solid lines are the wind-tunnel test results. The top two graphs in Figure 2.5 represent the inflow wake profiles at 100% span. The top-left graph shows the Gaussian distribution for a fractional wake velocity equal to twice the free-stream velocity, and the top-right graph shows the Gaussian distribution for a fractional wake equal to 1.5 times the free-stream velocity. From the top-left graph it can be seen that the Gaussian wake model from UNSFLO matches the experimentally determined wake model of the jet actuation.

The bottom two graphs in Figure 2.5 represent the inflow wake profiles at 88% span. Also here the Gaussian wake model from UNSFLO matches the experimentally determined wake model of the jet actuation.

2.3 Airfoil Geometry and Computational Grid

2.3.1 Airfoil Geometry

The compressor blade used for this research is the rotor blade of NASA Rotor Stage 35, documented in NASA Technical Paper 1338, [6]. The rotor has 36 rotor blades and a hub-to-tip radius ratio of 0.776 at the inlet and 0.801 at the exit. The aspect ratio is 1.19, the design pressure ratio is 1.82, and the tip speed is 454.5 m/sec. This rotor was chosen because Berndt's jet actuation [1] has been implemented in Rotor 35. The computations are carried out at the smallest flow coefficient for which test data are available for NASA Rotor 35. The smallest flow coefficient correspond to Reading 3976 in [6]. Table 2.2 compares the overall performance parameters for design with the lowest flow coefficient parameters.

Compressor Parameters	Design Overall	Reading 3976
Rotor Total Pressure Ratio	1.865	2.036
Stage Total Pressure Ratio	1.820	1.923
Rotor Adiabatic Efficiency	0.865	0.812
Stage Adiabatic Efficiency	0.828	0.737
Rotor Head Rise Coefficient	0.273	0.402
Flow Coefficient	0.451	0.340
Airflow at Orifice (kg/sec)	20.19	18.20
Rotative Speed (RPM)	17190	17220

Table 2.2: Comparison of overall performance between design and lowest flow coefficient

Table 2.3 summarizes the blade-element parameters of NASA Rotor 35 of the lowest flow coefficient for the two radial positions examined. The shape of the airfoil for 88% span and 100% span is shown in Figure 2.6.

Parameters (NASA Rotor 35)	88% Span	100% Span
Chord (mm)	56.0	56.1
Solidity	1.33	1.29
Rotor Stagger Angel (degrees)	54.5	65.7
Rotor Pitch (mm)	42.1	43.4
Total Pressure Ratio	2.035	2.092
Total Temperature Ratio	1.313	1.332
Inlet Relative Mach Number	1.415	1.412
Inlet Relative Inlet Angle (degrees)	69.4	73.6
Absolute Inlet Mach Number	0.498	0.399

Table 2.3: Blade-Element parameters at 88% span and 100% span

2.3.2 Computational Grid

UNSFLO uses an unstructured grid, with an advanced front-grid generator developed by Lindquist and Giles [16]. With this unstructured grid, each grid and its corresponding flow variables are associated with a particular index in a one-dimensional array. The program sweeps through the list of cells, gathers information from their corner nodes, performs the necessary calculations, and then distributes the appropriate changes of the flow variables back to the corner nodes.

The numerical grids for 100% span and 88% span are shown in Figure 2.7. For 100% span the grid for the inviscid Euler solver has 165 cells in the through-flow directions, 50 cells in the inflow and outflow boundary, and 48 cells between the cascade. For the viscous Navier-Stokes solver, the approximated thin viscous layer around the blade is about one to two cells of the inviscid grid. Furthermore, the viscous layer around the blades is divided in an inner region and outer region. The inner region close to the airfoil has 6 points and for the

inner and outer region 12 points are used. The inflow boundary is one-half of the airfoil chord upstream of leading edge and one-half of the airfoil chord downstream of trailing edge. For 88% span the inviscid and viscous grid points are the same as for 100% span.

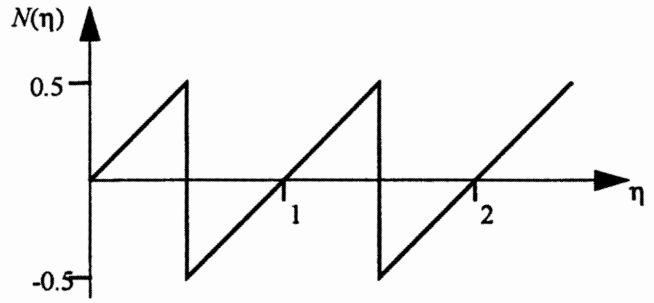

Figure 2.1: Definition of saw-tooth function $N(\eta)$

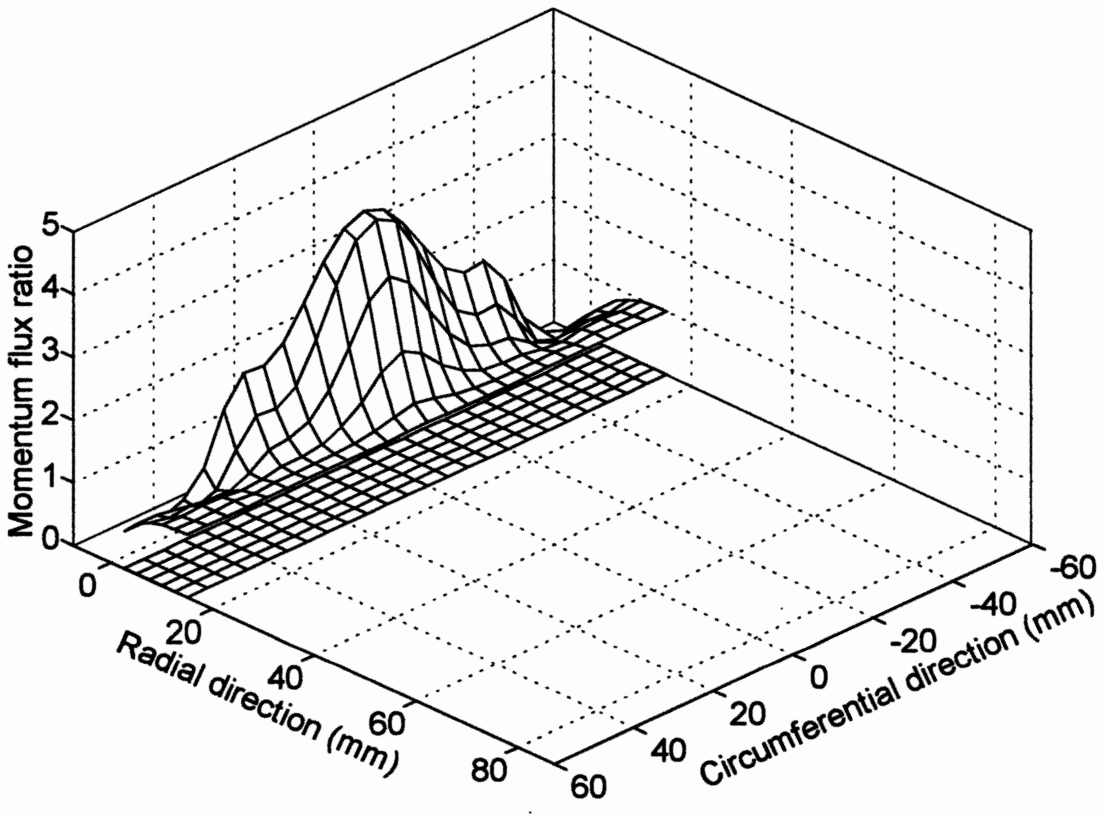

Figure 2.2: Steady momentum-flux distribution of the sheet injector

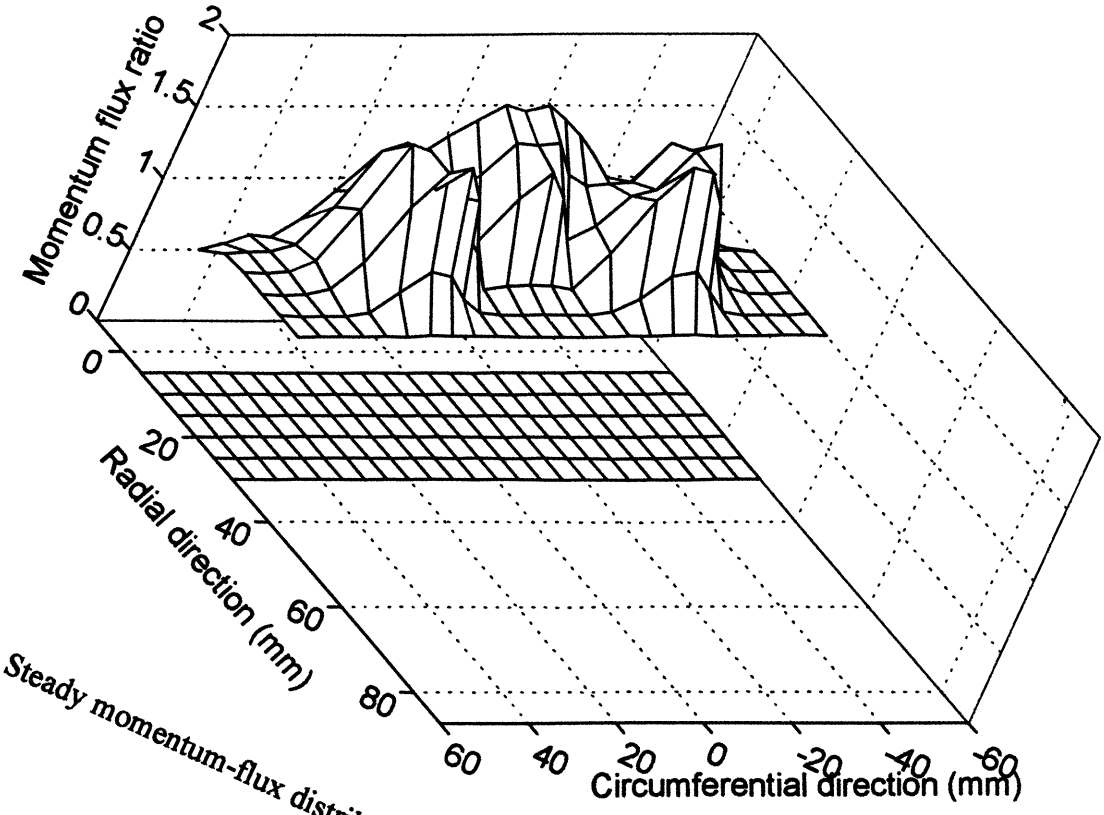

Figure 2.3: Steady momentum-flux distribution of the three-hole injector

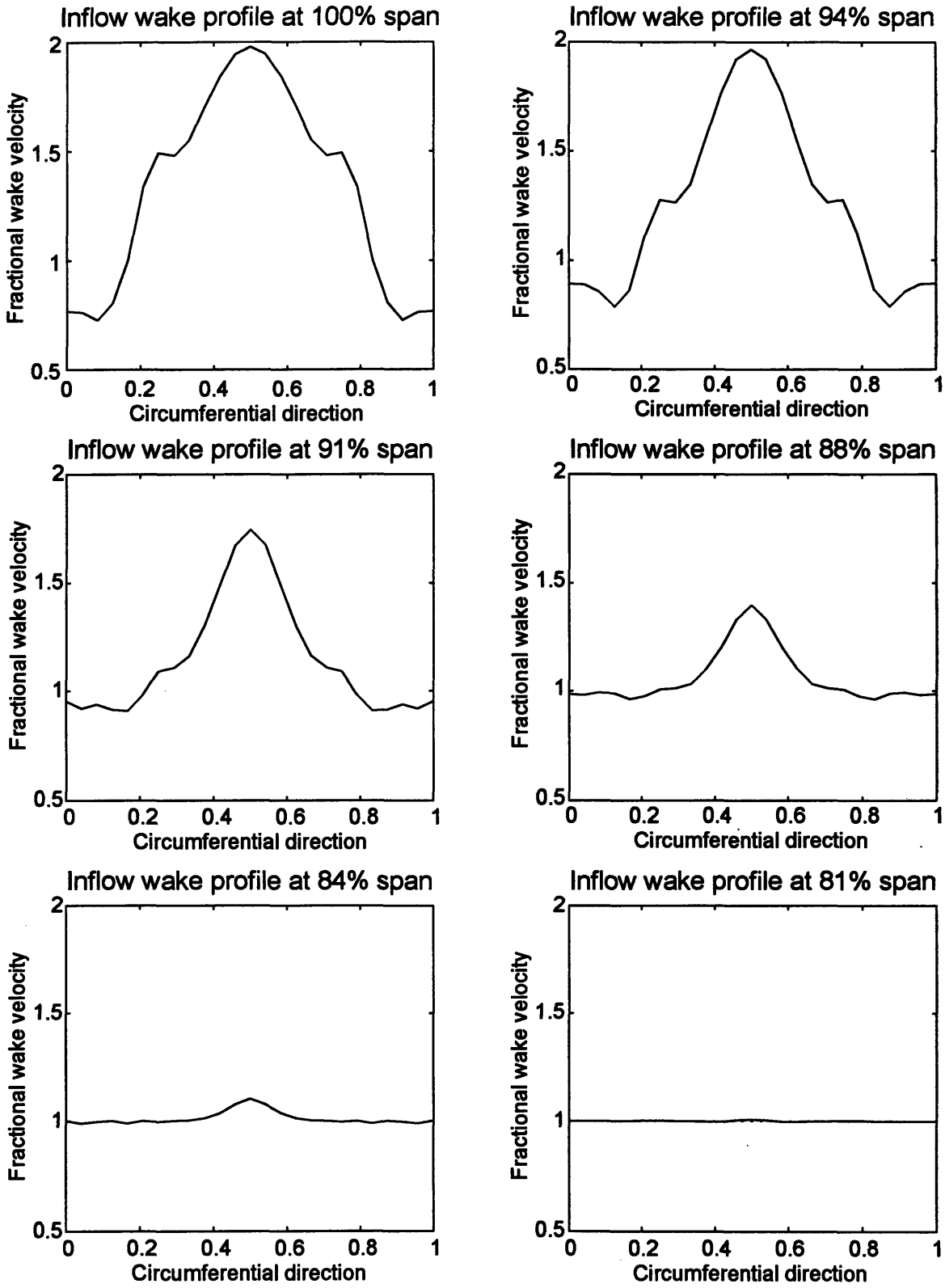

Figure 2.4: Inflow boundary velocity profiles at various locations for sheet injector at maximum injection (Circumferential direction is in percent of wake pitch.)

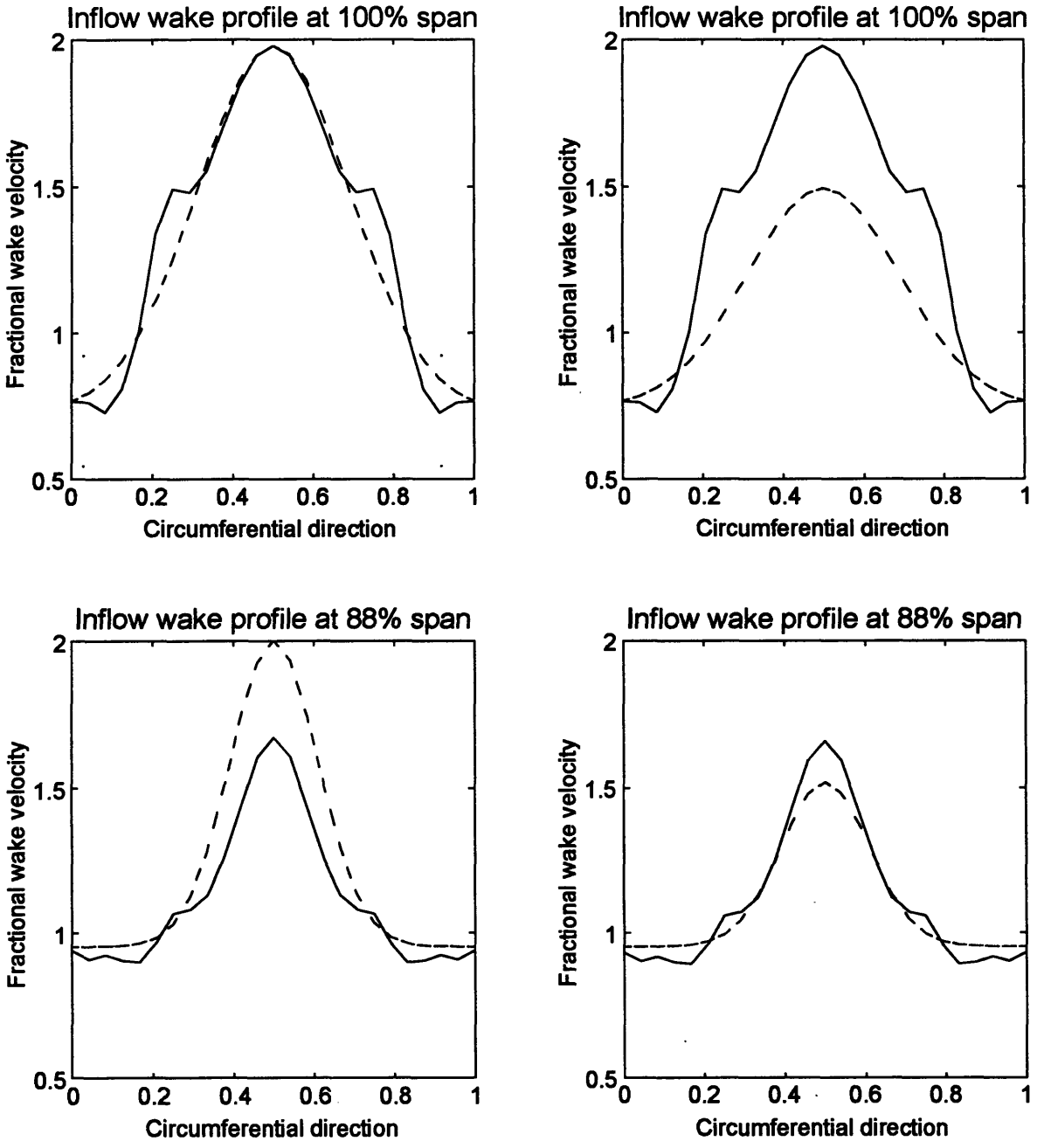

Figure 2.5: Gaussian wake profiles used in UNSFLO with an comparison to the wind-tunnel experiment (Circumferential direction is in percent of wake pitch.)

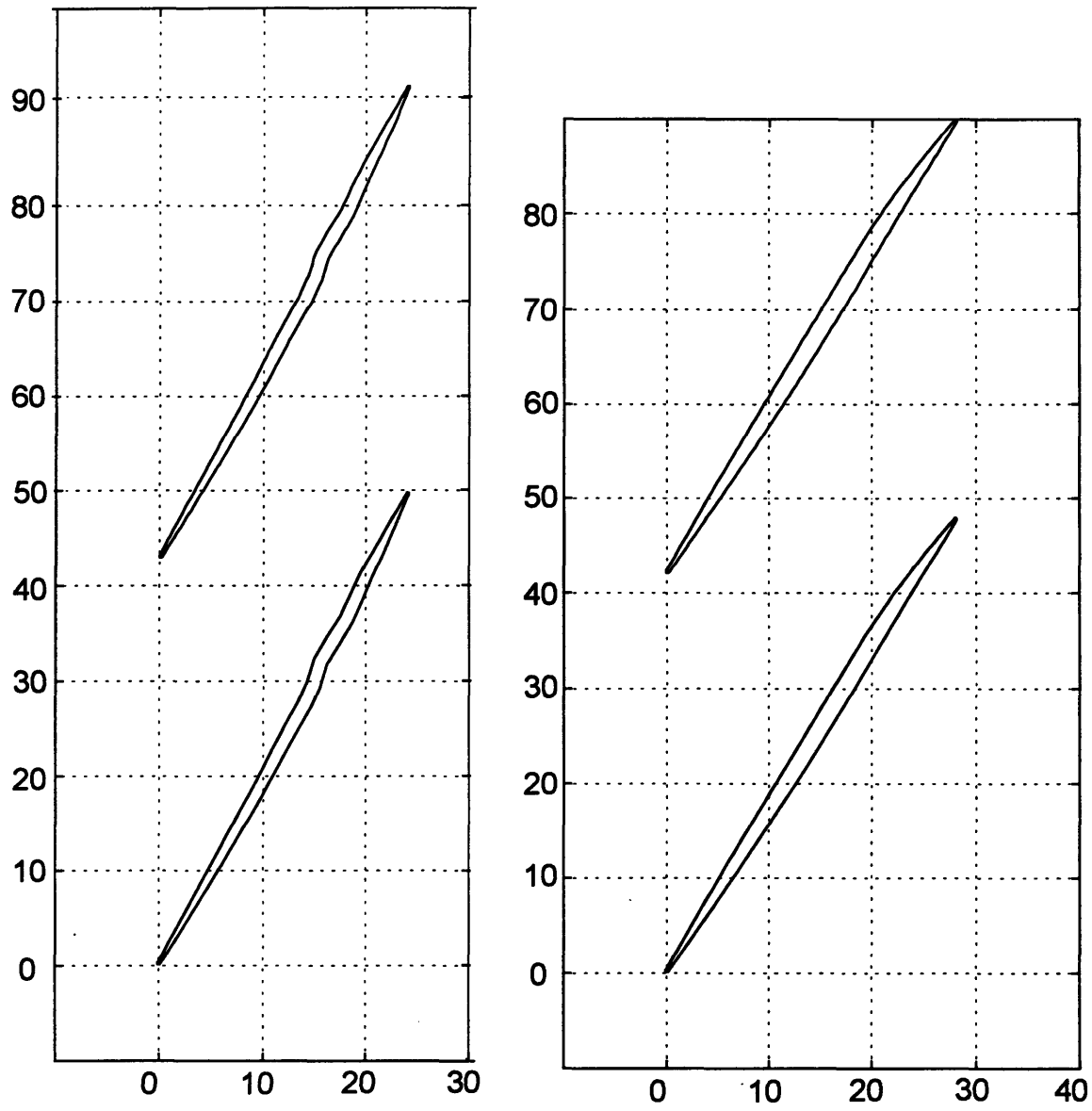

Figure 2.6: Airfoil shape at for radial position of 88% span and 100% span

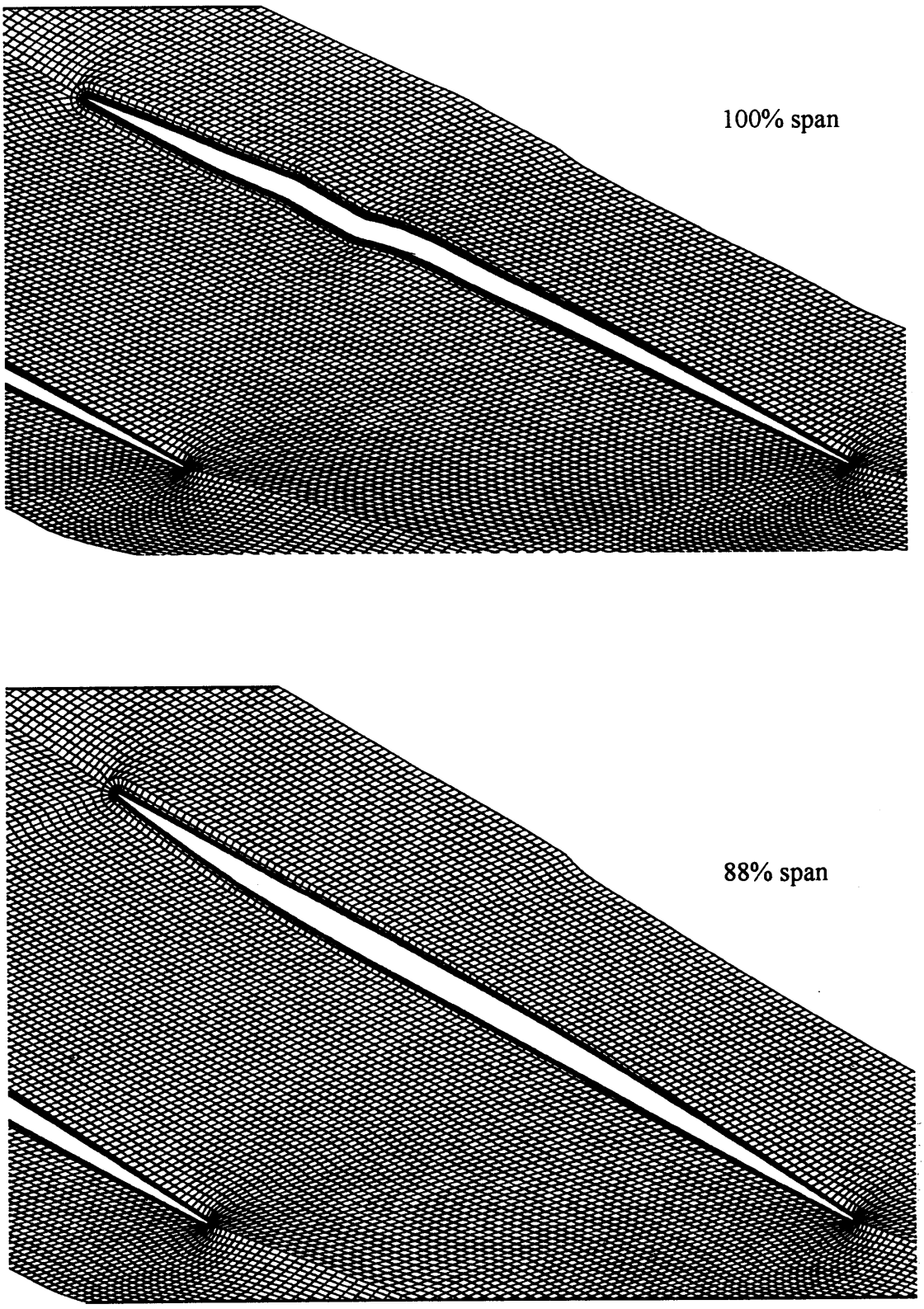

Figure 2.7: Computational grid for radial position of 88% span and 100% span

Chapter 3

Quasi-Steady Momentum Analysis

This chapter presents a quasi-steady analysis of unsteady blade forces. The inflow and outflow parameters, assumptions, and equations for the solution process are also given.

3.1 Inflow and Outflow Parameters with Velocity Triangles

3.1.1 Inflow Parameters for Rotor

To describe the flow that enters the rotor cascade, five parameters are needed: A_1, the inlet area (for the two-dimensional analysis equal to the rotor pitch at the inlet); p_1, the static pressure at the inlet; ρ_1, the density at the inlet; $V_{rel,1}$, the relative velocity at the inlet; and β_1, the relative angle at the inlet. The inlet rotor pitch is given by the geometry of the NASA Rotor 35. The pressure and density at the inlet are from given from the standard atmosphere. The relative velocity and relative angle at the inlet are a vector combination of the jet actuation attitude and free-stream velocity and rotor speed.

As described in Section 2.2.2: Jet-Actuation Wake Model, the wake model, which is used in the computer program UNSFLO to numerically analyze the rotor sections, is the Gaussian

model. The same equations that are used for the inlet boundary conditions of the numerical computer program in UNSFLO are also used for the quasi-steady momentum analysis.

As mentioned in Section 2.2.1, the three parameters that define the inflow wake model are the maximum amplitude of the wake angle, α_{wake}, the fractional velocity defect, D, and the shape function, d_2. This shape function is also a function of the characteristic wake width, W_{wake}, and the periodic saw-tooth function, N. However, for the quasi-steady momentum analysis, the periodic saw-tooth function is equal to zero, $N = 0$, to assure that the maximum value of the shape function is obtained. This means that the peak value of the unsteady disturbance is used and Equation (2.10) is now

$$d_2(\eta) = \exp\left(-\frac{0}{2W_{wake}^2}\right) = 1. \tag{3.1}$$

When the undisturbed velocity, entering the rotor cascade, is non-dimensioned with the free-stream inlet velocity, then one minus the fractional velocity defect, (1-D), represent the non-dimensioned combination of the inlet velocity and the jet velocity. The minus between the inlet velocity and the jet velocity comes from the definition of the jet velocity which represents the fractional velocity defect.

The axial and tangential components (vector combination of free-stream velocity, rotor speed, and jet velocity) are obtained by

$$(1-D)_{axial} = (1-D) \cdot \cos(\alpha_{wake}), \tag{3.2}$$

$$(1-D)_{tangential} = (1-D) \cdot \sin(\alpha_{wake}) + WS_{ndim}, \tag{3.3}$$

where α_{wake} is the jet angle with respect to the absolute free-stream velocity, and WS_{ndim} is the rotor wheel-speed which is non-dimensioned with the free-stream inflow velocity.

The relative inflow velocity for the combination of free-stream inlet velocity, rotor wheel-speed, and jet velocity is

$$V_{rel,1} = \sqrt{(1-D)_{axial}^2 + (1-D)_{tangential}^2}. \tag{3.4}$$

The relative inflow angle is

$$\beta_1 = \text{atan}\left(\frac{(1-D)_{tangential}}{(1-D)_{axial}}\right). \tag{3.5}$$

The relative inflow angles at radial positions of 88% span and 100% span are presented in Figure 3.1 and 3.2, respectively, for different jet angles and different jet velocities. The jet angles range from -45 degrees to 45 degrees, and the jet velocities range from 1.0 times the free-stream velocity to 2.0 times the free-stream velocity. (A jet velocity equal to 1.0 means that the jet-stream has the same velocity as the free-stream.) Starting from a jet angle of +45 degrees, the relative inflow angle decreases until a point, which is around -30 degrees of the jet angle, and increase at -45 degrees. This is because the cosine term in Equation (3.2) has the same result for positive and negative jet angles, which means that starting from a jet angle of +45 degrees, the cosine term increases until 0 degrees and then decreases for negative jet angles. On the other hand, the sine term in Equation (3.3) has a positive result for positive jet angles and a negative result for negative jet angles.

The relative inflow angles at the radial positions of 88% span and 100% span are plotted in Figure 3.3 and 3.4, respectively, for different jet angles and jet velocities. Both figures also include diagrams of velocity triangles for jet angles of -30 degrees and +30 degrees, and for three different jet velocities, namely, 1.0 times the free-stream velocity, 1.5 times the free-stream velocity, and 2.0 times the free-stream velocity.

3.1.2 Outflow Parameters for Rotor

To describe the flow that leaves the rotor cascade, five parameters are needed: A_2, the exit area (for the two-dimensional analysis equal to one times the rotor pitch at the exit); p_2, the static pressure at the exit; ρ_2, the density at the exit; $V_{rel,2}$, the relative velocity at the exit; and β_2, the relative angle at the exit. The rotor pitch for the exit is a parameter that is given by the geometry of the NASA Rotor 35 and was presented in Section 2.3.1: Airfoil Geometry.

There are five equations that describe the flow, continuity equation, momentum in x and y direction, energy equation, and isentropic equation. Together with the geometric parameters

from the NASA Rotor 35, this leaves six unknowns within the five equations. This six unknowns are the variables from the exit flow of the rotor cascade, except the exit area, and the two forces from the momentum equations in x and y direction. Therefore, one more variable needs to be prescribed. This variable is the exit angle, β_2. For a description of how this exit angle can be chosen, refer to Section 3.2: Equation and Solution Procedure for Quasi-Steady Momentum Analysis.

3.2 Equation and Solution Procedure for Quasi-Steady Momentum Analysis

3.2.1 Equations and Assumptions

This section gives the equations and assumptions to compute the axial force and the tangential force using the quasi-steady analysis. A detailed derivation with the assumptions applied to each step during the derivation is presented in Appendix C: Detailed Derivation of Quasi-Steady Momentum Analysis. The list of assumptions that were needed to derive the final equations for the quasi-steady momentum analysis are summarized in this section:

- the fluid flow is steady,
- no work is delivered through a shaft into the control volume,
- the fluid flow is adiabatic, a process in which no heat is added or taken away,
- the flow is reversible, a process in which no frictional or dissipative effects occur,
- the density, velocity, and pressure are uniform across the inlet area and exit area,
- the gas is calorically perfect, and
- the flow is 2-dimensional.

The combination of an adiabatic and reversible process result in an isentropic fluid flow. This assumption, specially the assumption of an reversible process, is justified by using the isentropic relationship and the results computed from UNSFLO. It is found that the computed isentropic results differ 3% from the results of UNSFLO. This calculation is carried out by

using the density for inlet and exit and the inlet pressure computed from UNSFLO and calculate with the isentropic relationship the exit pressure. This exit pressure is the compared to the results from UNSFLO.

With these assumptions the equations for the control volume (see Appendix C: Detailed Derivation of Quasi-Steady Momentum Analysis) are

continuity

$$A_2\rho_2 V_{rel,2}\cos\beta_2 - A_1\rho_1 V_{rel,1}\cos\beta_1 = 0, \tag{3.6}$$

momentum in x direction,

$$F_x = A_2\left[p_2 + \rho_2 (V_{rel,2}\cos\beta_2)^2\right] - A_1\left[p_1 + \rho_1 (V_{rel,1}\cos\beta_1)^2\right], \tag{3.7}$$

momentum in y direction,

$$F_y = A_2\rho_2 V_{rel,2}^2\cos\beta_2\sin\beta_2 - A_1\rho_1 V_{rel,1}^2\cos\beta_1\sin\beta_1, \tag{3.8}$$

the energy equation, which also includes the equation of state,

$$\rho_2 V_{rel,2}\cos\beta_2\left(\frac{p_2}{\rho_2}\frac{\gamma}{\gamma-1} + \frac{V_{rel,2}^2}{2}\right) = \rho_1 V_{rel,1}\cos\beta_1\left(\frac{p_1}{\rho_1}\frac{\gamma}{\gamma-1} + \frac{V_{rel,1}^2}{2}\right), \tag{3.9}$$

and the isentropic relationship,

$$\frac{p_2}{p_1} = \left(\frac{\rho_2}{\rho_1}\right)^{\gamma}. \tag{3.10}$$

Solving Equation (3.6), the continuity equation, for ρ_2 and substituting this equation together with Equation (3.10), the isentropic relationship, into Equation (3.7) to (3.9), the axial force is

$$\begin{aligned} F_x = {} & A_2\left[p_1\left(\frac{V_{rel,2}\cos\beta_2}{V_{rel,1}\cos\beta_1}\right)^{-\gamma} + \rho_1 V_{rel,1}\cos\beta_1 V_{rel,2}\cos\beta_2\right] \\ & - A_1\left[p_1 + \rho_1 (V_{rel,1}\cos\beta_1)^2\right] \end{aligned} \tag{3.11}$$

The tangential force is

$$F_y = A_2\rho_1 V_{rel,1}\cos\beta_1 V_{rel,2}\sin\beta_2 - A_1\rho_1 V_{rel,1}^2\cos\beta_1\sin\beta_1. \tag{3.12}$$

The energy equation is

$$V_{rel,2}^2 + V_{rel,2}^{1-\gamma}\left[\frac{p_1}{\rho_1}\frac{2\gamma}{\gamma-1}\left(\frac{\cos\beta_2}{V_{rel,1}\cos\beta_1}\right)^{1-\gamma}\right] = \frac{p_1}{\rho_1}\frac{2\gamma}{\gamma-1} + V_{rel,1}^2. \tag{3.13}$$

The axial force and tangential force in Equation (3.11) and (3.12) can be solved with the use of Equation (3.13) since the only other unknown is the relative exit velocity, $V_{rel,2}$. The iterative scheme for the solution and the choice of the relative exit angle is given in the next section.

3.2.2 Relative Exit Angle and Solution Process

Since the resulting equations, presented in Section 3.2.1: Equations and Assumptions, are non-linear, an iterative scheme is needed to calculate the forces. The choice of relative exit angle for the calculation of the forces is discussed in this section. The iterative scheme used to solve Equation (3.13) is the Newton-Raphson method because of its simplicity and fast convergence to the solution. This method is explained in detail in [21] and summarized here.

The Newton-Raphson scheme is an iterative method for solving the non-linear equation $f(V_{rel,2}) = 0$, where f is assumed to have a continuous derivative f'. The idea of this method is to approximate the graph of f by tangential lines; therefore, with the tangent defined by

$$f'({}^{i-1}V_{rel,2}) = \frac{f({}^{i-1}V_{rel,2})}{{}^{i-1}V_{rel,2} - {}^{i}V_{rel,2}}, \tag{3.14}$$

a new relative exit velocity is obtained by

$${}^{i}V_{rel,2} = {}^{i-1}V_{rel,2} - \frac{f({}^{i-1}V_{rel,2})}{f'({}^{i-1}V_{rel,2})}. \tag{3.15}$$

The left superscript denote the steps of iteration, where ${}^{0}V_{rel,2}$ is the initial guess and i goes from 1, 2, 3,... to convergence. From Equation (3.13) two solutions are possible, namely, a subsonic relative exit velocity and a supersonic relative exit velocity. Therefore, the choice of the initial guess is important and the converged solution from the Newton-Raphson scheme needs to be checked if the desired relative exit velocity is obtained.

During the derivation of the equations of fluid motion, derived in Appendix C and discussed in Section 3.1.2, it was assumed that the relative exit angle, β_2, is a parameter that is known before the forces of the fluid flow can be calculated. The following paragraphs discuss different possibilities for choosing the relative exit angle for the different jet velocities and different jet angles. The result of the tangential forces and axial forces for the different exit angles is presented in Section 4.2: Comparison of Unsteady Forces Computed with UNSFLO and Quasi-Steady Momentum Analysis.

The first possibility is to use a constant value for all the jet angles from -45 degrees to +45 degrees, but a different number for different jet velocities. This means that for the radial position of 88% span the relative exit angle for a jet velocity of twice the free-stream velocity must be smaller than 40 degrees, measured relative to the absolute free-stream velocity, for all the jet angles from -45 degrees to +45 degrees. This relative exit angle of less then 40 degrees is needed since the relative inflow angle is about 41 degrees at an jet angle of -45 degrees (Figure 3.1). Similarly, for a jet velocity of 1.5 times the free-stream velocity and a radial position of 88% span, the relative exit angle must be smaller than 55 degrees for all the jet angles. A constant number for all jet angles also means that the turning for a jet angle of +45 degrees will be 30 degrees but only 1 degrees for a jet angle of -45 degrees. This will result in an over-prediction of the forces at a jet angle of +45 degrees and an under-prediction of the forces at a jet angle of -45 degrees, and this idea is not very useful in the present context.

A second possibility is to use an angle, κ, that is subtracted from the relative inflow angle, $\beta_1 - \kappa$, where κ is different for different jet velocities. This means that the relative exit angle would follow the same shape as the relative inflow angle, as shown in Figure 3.1, but shifted by κ. For example, at a jet angle of zero degrees and a jet velocity of 1.5 times the free-stream velocity, the inflow angle is about 60 degrees and the exit angle is 50 degrees when κ is equal to 10. The angle κ is obtained from the difference of exit angle to inlet angle in the computa-

tion with UNSFLO at zero degrees jet angle for different jet velocities. This method is referred to as "Method 1" later in this section and in Section 4.2.

A third possibility is to choose the relative exit angle by using the result of the exit velocity for an incompressible fluid in a rotor cascade. For incompressible flow

$$C_p = 1 - \frac{(\cos\beta_1)^2}{(\cos\beta_2)^2}, \tag{3.16}$$

where C_p is the pressure coefficient which can be related to the exit and inlet pressure and the relative inflow Mach number given by

$$\frac{p_2}{p_1} = 1 + C_p \frac{\gamma M_{rel,1}^2}{2}. \tag{3.17}$$

Now, with the relative inlet angle, β_1, the relative inlet Mach number, $M_{rel,1}$, the inlet pressure, p_1, and the exit pressure, p_2, the relative exit angle, β_2, can be computed from the incompressible equation above. For this method the exit pressure need to be known or calculated before it can be used in Equation (3.17). In the analysis the following process is used:

1. use the relative exit angle that was obtained from Method 1 and calculate the exit pressure with the Newton-Raphson scheme,
2. use the same relative exit angle as in step 1 and calculate the incompressible exit pressure with Equation (3.16) and (3.17),
3. calculate the average of the exit pressure obtained from step 1 and step 2, and
4. calculate the relative exit angle with the incompressible equations given by Equation (3.16) and (3.17).

With the new relative exit angle, the new exit pressure can be computed with the Newton-Raphson scheme. This method is referred as "Method 2" in Section 4.2.

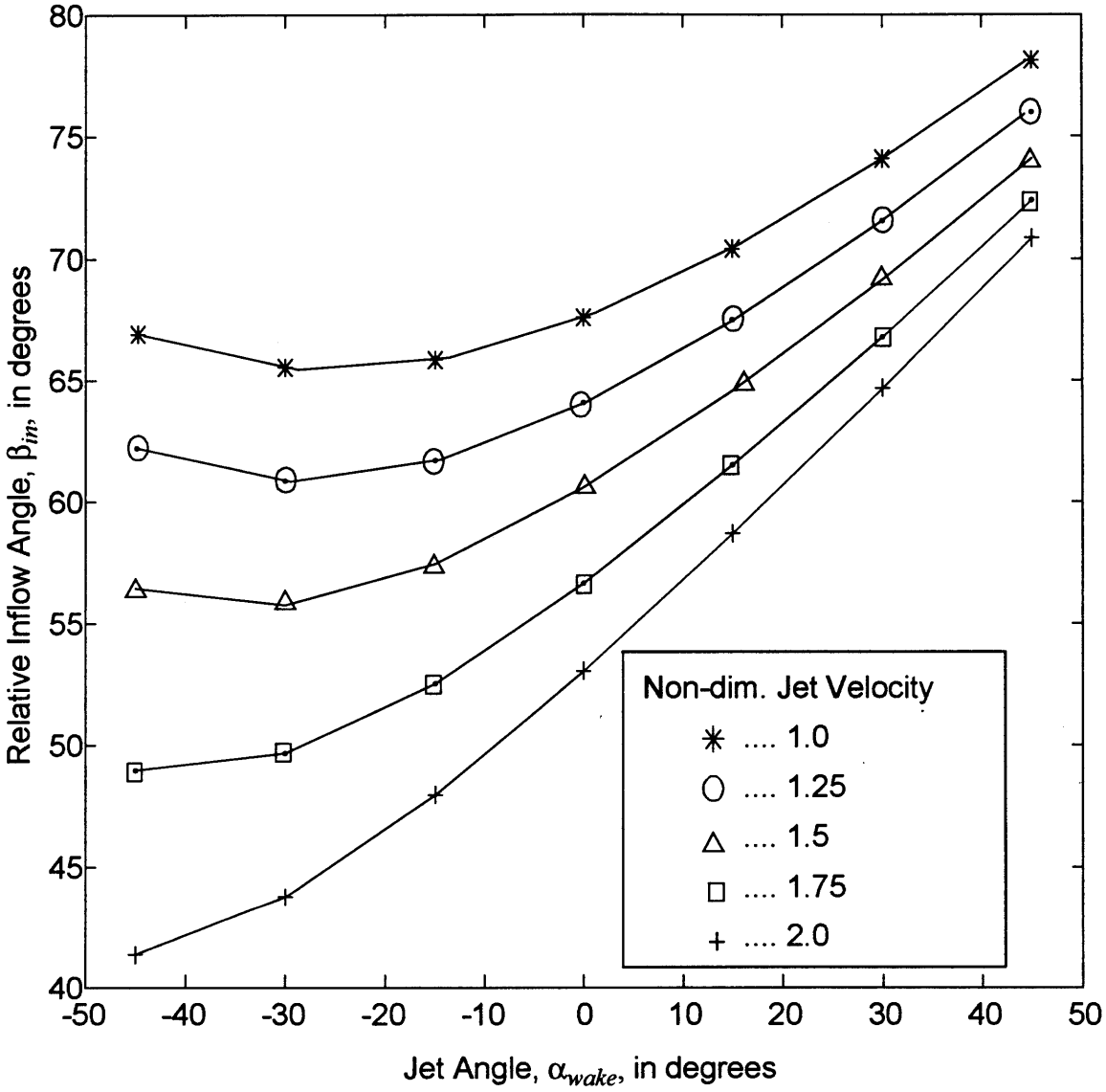

Figure 3.1: Relative inflow angle versus jet angle for different jet velocities at a radial position of 88% span

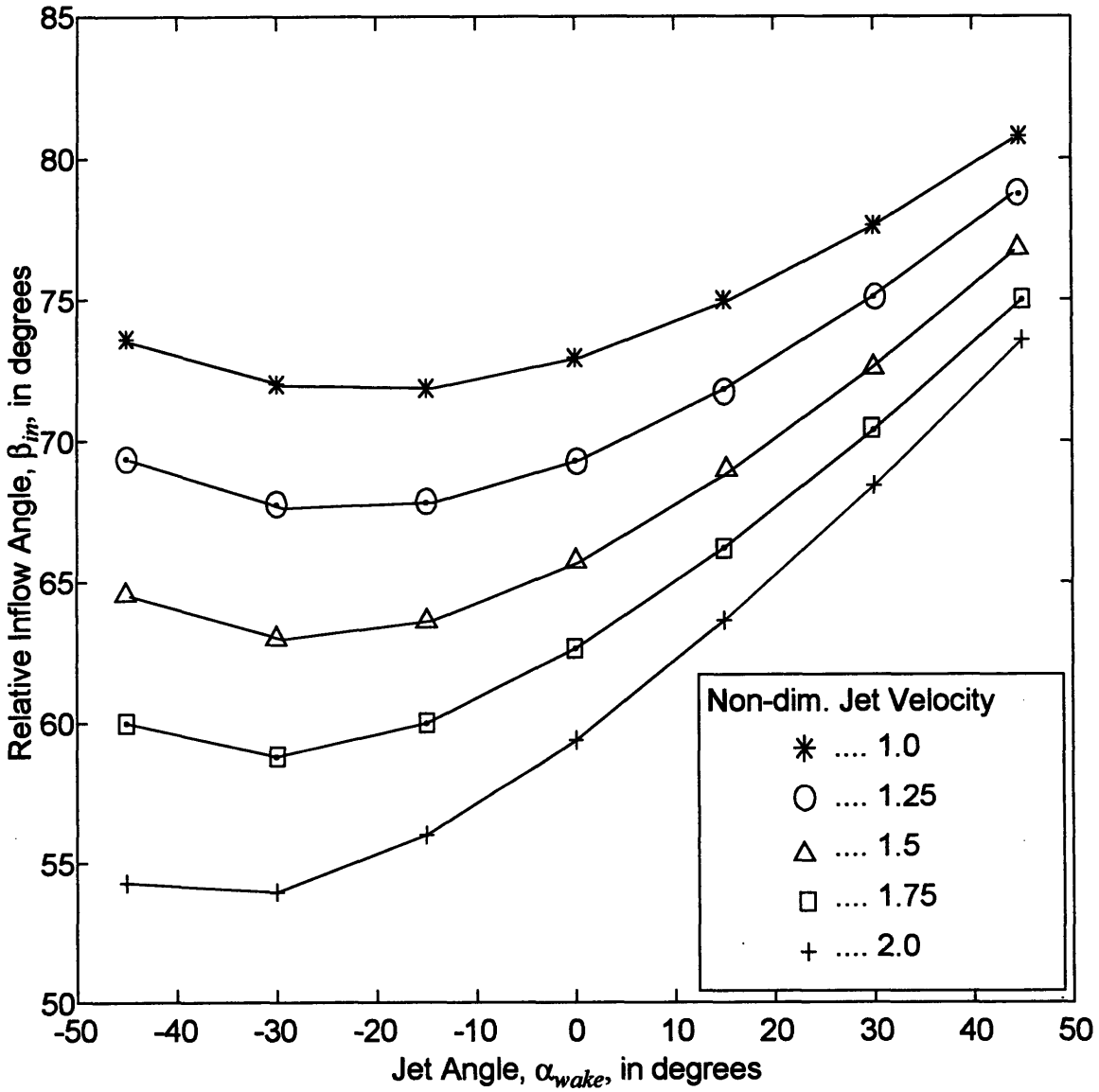

Figure 3.2: Relative inflow angle versus jet angle for different jet velocities at a radial position of 100% span

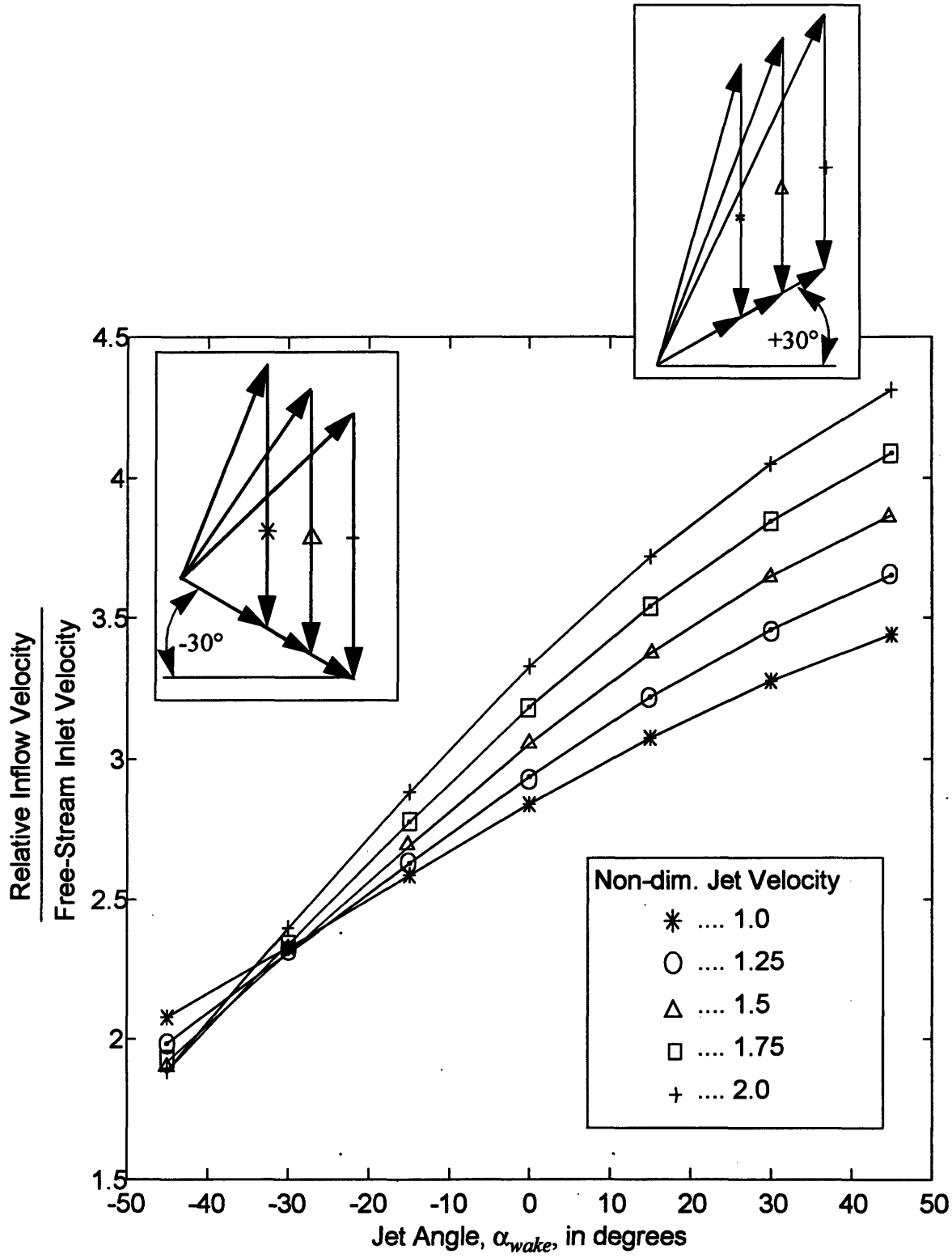

Figure 3.3: Relative inflow velocity versus jet angle for different jet velocities at a radial position of 88% span

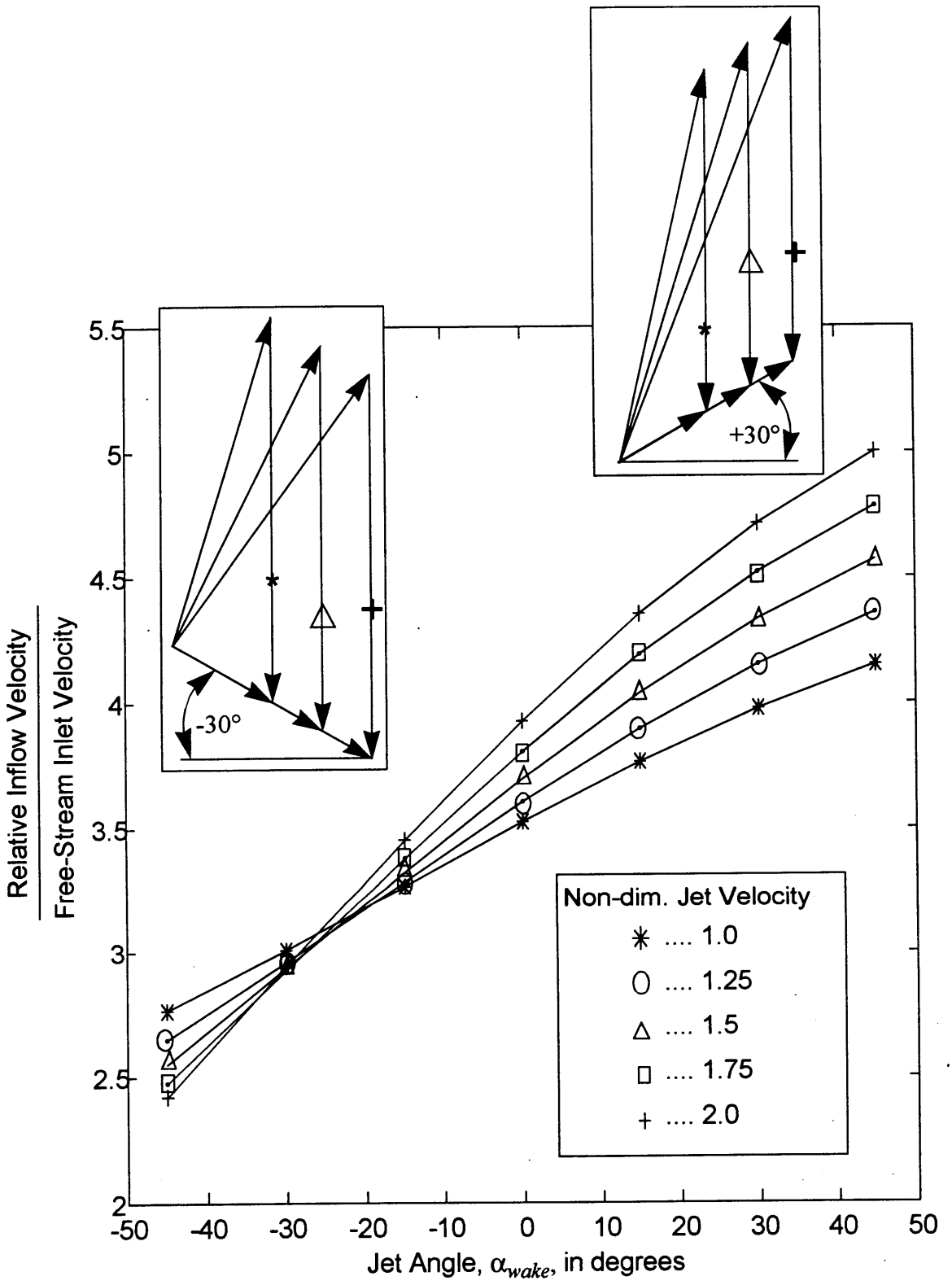

Figure 3.4: Relative inflow velocity versus jet angle for different jet velocities at a radial position of 100% span

Chapter 4

Results and Discussion

This chapter presents the results of the unsteady forces and unsteady moments computed using UNSFLO. It is divided into four sections. First, the results are presented with figures of the difference in maximum to minimum of the unsteady forces, in x and y direction, and unsteady moments for each of the radial positions, 88% span and 100% span. Second, the results of the difference in maximum to minimum of the unsteady forces, in x and y direction, computed with UNSFLO are compared with the quasi-steady momentum model for the two radial positions, 88% span and 100% span. Third, from the results from UNSFLO, the averaged first, second, and third harmonic amplitudes of the unsteady forces, in x and y direction, and unsteady moments for each of the radial positions, 88% span and 100% span, are produced. Fourth, the pressure difference between rotor inlet and exit is given for each of the radial positions, 88% span and 100% span. The results on which the discussion in this chapter is based are collected in Appendix D: Computed Results from UNSFLO.

Table 4.1 shows the magnitude of the steady flow results from the axial forces, tangential forces, and moments for the two radial positions, 88% span and 100% span. The forces of Table 4.1 are non-dimensioned with the density, the square of relative inflow velocity, and the

aerodynamic chord. The moments of Table 4.1 are non-dimensioned with the density, the square of relative inflow velocity, and the square of aerodynamic chord.

	Axial Force $\frac{F_{x,\,steady}}{\frac{1}{2}\rho V_{rel}^2 C}$	Tangential Force $\frac{F_{y,\,steady}}{\frac{1}{2}\rho V_{rel}^2 C}$	Moment $\frac{M_{steady}}{\frac{1}{2}\rho V_{rel}^2 C}$
100% Span	0.378	0.189	0.159
88% Span	0.343	0.172	0.153

Table 4.1: Magnitudes of steady flow forces and moments at two radial positions

4.1 Unsteady Forces and Unsteady Moments

This section presents and discusses the results of the unsteady forces, in x and y direction, and unsteady moments for each of the radial positions, 88% span and 100% span. These results are plotted versus jet angle α_{wake}.

Figure 4.1 and 4.2 give the axial forces computed using UNSFLO for different jet velocities plotted against jet angles for radial positions of 88% span and 100% span, respectively. Figure 4.3 and 4.4 give the tangential forces for different jet velocities plotted against jet angles for the radial positions of 88% span and 100% span, respectively. Figure 4.5 and 4.6 give the moments for different jet velocities plotted against different jet angles for the radial positions of 88% span and 100% span, respectively. The unsteady forces are non-dimensionalized with the density, ρ, the square of relative inflow velocity, V_{rel}^2 , and the aerodynamic chord, C. The unsteady moments of these figures are non-dimensioned with the density, ρ, the square of relative inflow velocity, V_{rel}^2 , and the square of aerodynamic chord, C^2. The results for the non-dimensional jet velocity of 2 are shown with the symbol -⊟-, and the results for the non-dimensional jet velocity of 1.5 are shown with the symbol -✕-.

For both radial positions, 88% span and 100% span, and for both non-dimensional jet velocities, the highest axial force, tangential force, and moment is at +45 degrees jet angle, and the lowest axial force, tangential force, and moment is at 0 degrees jet angle. The axial

force, tangential force, and moment for the negative jet angles increase until an angle of -30 degrees and then decreases. This can be explained by looking at Figure 3.1 where the relative inflow angle is plotted against the jet angle. From this figure it can be seen that the jet angle of -15 degrees and -45 degrees have approximately the same relative inflow angle, but the relative inflow angle for a jet angle equal to -30 degrees is lower.

Another examination can be done when the axial forces, tangential forces, and moments can be obtained when the forces and moments are non-dimensionalized with the relative inflow velocity multiplied by the change of relative inflow velocity. This change of relative inflow velocity, V_X, is defined as the difference of maximum to minimum relative inflow velocity times a constant number equal to four so that the plot is between zero and one. Figure 4.7 and 4.8 give the axial forces for different jet velocities plotted against jet angles for the radial positions of 88% span and 100% span, respectively. Figure 4.9 and 4.10 give the tangential forces for different jet velocities plotted against jet angles for the radial positions of 88% span and 100% span, respectively, and Figure 4.11 and 4.12 give the moments for different jet velocities plotted against jet angles for these radial positions. The results for the non-dimensional jet velocity of 2 are shown with the symbol -⊟-, and the results for the non-dimensional jet velocity of 1.5 are shown with the symbol -✕-.

The results from the two non-dimensional jet velocities collapse into one line for the axial forces, tangential forces, and moments at the radial positions of 88% span and 100% span. The largest difference is less then 10%.

Using the collapsed resulting figures, it can be seen for a radial position of 88% span that the unsteady force (axial and tangential) computed for +15 degrees jet angle are 1.2 times larger, for +30 degrees jet angle are 1.6 times larger, and for +45 degrees jet angle are 2.5 times larger compared to the results at zero degrees jet angle. The unsteady moment for +15 degrees jet angle is 1.2 times larger, for +30 degrees jet angle is 1.9 times larger, and for +45 degrees jet angle is 3.6 times larger then the unsteady moment at zero degrees jet angle.

For a radial position of 100% span, the unsteady force (axial and tangential) computed for +15 degrees jet angle are 1.4 times larger, for +30 degrees jet angle are 1.8 times larger, and for +45 degrees jet angle are 2.7 times larger then the unsteady forces at zero degrees jet angle. The unsteady moment for +15 degrees jet angle is 1.4 times larger, for +30 degrees jet

angle is 1.9 times larger, and for +45 degrees jet angle is 3.4 times larger than the unsteady moment at zero degrees jet angle.

For the negative jet angles, the results are that for a radial position of 88% span the unsteady force (axial and tangential) computed for -15 degrees and -45 degrees jet angle are 1.4 times larger and for -30 degrees jet angle are 2.0 times larger than the unsteady forces at zero degrees. The unsteady moment for -15 degrees and -45 degrees jet angle is 1.3 times larger and for -30 degrees jet angle is 2.2 times larger than the unsteady moment at zero degrees. For a radial position of 100% span, the unsteady forces (axial and tangential) for -15 degrees and -45 degrees jet angle is 1.6 times larger and for -30 degrees jet angle is 2.2 times larger than the unsteady forces at zero degrees jet angle. The unsteady moments for -15 degrees and -45 degrees jet angle is 1.3 times larger and for -30 degrees jet angle is 2.3 times larger than the unsteady moment at zero degrees jet angle.

As mentioned in Section 1.2, the reduced frequency is a parameter which can be interpreted as a ratio of the time it takes for a fluid particle to travels through the rotor passage to the time it takes the rotor to pass through a distorted segment of the flow. The unsteady forces, in x and y direction, and unsteady moments can be plotted against reduced frequency, $\tilde{\omega}$, with

$$\tilde{\omega} \equiv \frac{\omega C}{V_x} = \frac{2\pi \, \mathrm{WS}}{R_{wake,\,r}\, S_r} \frac{C}{V_x}, \tag{4.1}$$

The parameter ω is the rotor passing frequency, C is the axial chord of the rotor, V_x is the axial flow velocity, WS is the rotor wheel-speed, $R_{wake,r}$ is the wake-to-rotor pitch ratio, and S_r is the pitch of the rotor blade row.

Figure 4.13 and 4.14 give unsteady axial forces for different jet velocities, plotted against reduced frequency, for 88% and 100% span, respectively. The unsteady axial forces of these figures are non-dimensioned with the density, ρ, the square of relative inflow velocity, V_{rel}^2, and the aerodynamic chord, C. The results for the non-dimensional jet velocity of 2 are shown with the symbol -⊟-, and the results for the non-dimensional jet velocity of 1.5 are shown with the symbol -✕-.

The reduced frequency at 88% span is roughly between 2.2 and 3.7 for both jet velocities. For 100% span and both non-dimensional jet velocities, the reduced frequency varies roughly

from 2.3 to 3.3. For both radial positions of 88% span and 100% span and both non-dimensional jet velocities, the highest reduced frequencies correspond to a jet angle of -45 degrees, and the lowest reduced frequency correspond to a jet angle equal to +45 degrees.

4.2 Comparison of Unsteady Forces Computed with UNSFLO and Quasi-Steady Momentum Analysis

This section gives the result of the comparison between the unsteady forces computed with UNSFLO and the forces computed with the quasi-steady momentum model. The unsteady forces from UNSFLO are shown with the symbol -x- and the forces computed with the quasi-steady model are shown with the symbol -o-. As discussed in Section 3.2, there are two methods (Method 1 and Method 2) for obtaining the relative exit angle. The first is to compute the relative exit angle, β_2, using a constant angle subtracted from the relative inflow angle, β_1; $\beta_2 = \beta_1 - \kappa$. This angle is equal to 12 for non-dimensional jet velocity of 1.5 and equal to 6 for non-dimensional jet velocity of 2.0. These values were obtained from the computation with UNSFLO of the unsteady forces at zero degrees jet angle for non-dimensionalized jet velocity of 1.5 and 2.0, respectively. The resulting relative exit angles are shown in Figure 4.15 to 4.18 with the corresponding numbers on the right axis of the plot. Figure 4.15 and 4.16 give the axial forces from UNSFLO and quasi-steady analysis plotted against jet angles at radial positions of 88% span and 100% span, respectively. Figure 4.17 and 4.18 give the tangential forces from UNSFLO and quasi-steady analysis plotted against jet angles for the radial positions of 88% span and 100% span, respectively. The difference between the forces computed from UNSFLO and the quasi-steady analysis range from 8% to 40%.

The second method is to compute the relative exit angle, β_2, and exit pressure, p_2, by using the incompressible equations, Equation (3.16) and (3.17), and results from UNSFLO. The resulting relative exit angles are shown in Figure 4.19 to 4.22 with the corresponding numbers on the right axis of the plot. Figure 4.19 and 4.20 give the axial forces from UNSFLO and quasi-steady analysis plotted against jet angles for 88% span and 100% span,

respectively. Figure 4.21 and 4.22 give the tangential forces from UNSFLO and quasi-steady analysis plotted against jet angles for 88% span and 100% span, respectively.

Using Method 2, the difference between the forces computed from UNSFLO and from the quasi-steady analysis range from 0.5% to 10%. The difference in exit angles, β_2, between the two methods range from 2%.

4.3 First, Second, and Third Harmonic Amplitudes of Unsteady Forces and Unsteady moments

As mentioned in the introduction, when the jet actuation is implemented in the high speed compressor, a problem of concern is the mechanical and aerodynamical forces and moments of the rotor blades due to the jet actuator attitude. Therefore, this section will present the averaged first, second, and third harmonic amplitudes of the unsteady forces, in x and y direction, and the unsteady moments.

The procedure to compute the harmonic amplitude and phase is outlined in Meirovitch, [23], "Elements of Vibration Analysis" and is reviewed here. The harmonic amplitude and phase for an unsteady force or moment can be computed by

$$|G|_n = \sqrt{\mathrm{Re}(G)_n^2 + \mathrm{Im}(G)_n^2} \qquad \phi_n = \mathrm{atan}\left[\frac{-\mathrm{Im}(G)_n}{\mathrm{Re}(G)_n}\right] \tag{4.2}$$

with

$$\mathrm{Re}(G)_n = \frac{1}{L}\int_{-L}^{L} F(t)\cos\left(\frac{\pi n t}{L}\right)dt \qquad \mathrm{Im}(G)_n = \frac{1}{L}\int_{-L}^{L} F(t)\sin\left(\frac{\pi n t}{L}\right)dt \,, \tag{4.3}$$

where $L = p_L/2$ and p_L is the period of the blade passing by the jet velocity wake, $F(t)$ can be the axial force, tangential force, or moment at a different time t, and n is equal to *1* for the first harmonic, equal to *2* for the second harmonic, and equal to *3* for the third harmonic.

Figure 4.23 to 4.28 show the harmonic amplitude and phase for the non-dimensional jet velocity of 1.5 and for different jet angles at radial positions of 88% span and 100% span. Figure 4.23 and 4.24 give the amplitude and phase of the axial forces for different jet angles versus frequency mode for 88% and 100% span, respectively. Figure 4.25 and 4.26 give the amplitude and phase of the tangential forces for different jet angles versus frequency mode for 88% and 100% span, respectively. Figure 4.27 and 4.28 give the amplitude and phase of the moments for different jet angles versus jet frequency mode for the radial positions of 88% span and 100% span, respectively. The harmonic amplitudes for the axial force are non-dimensionalized with respect to the steady axial force, and the harmonic amplitudes for the tangential force are non-dimensioned with respect to the steady tangential force. The harmonic amplitudes for the moment are non-dimensioned with respect to the steady moment. The results for the jet angle of -45 degrees is shown with the symbol -✕-, for the jet angle of -30 degrees is shown with -▲-, for the jet angle -15 degrees is shown with -◆-, for the jet angle 0 degrees is shown with -■-, for the jet angle +15 degrees is shown with -✱-, for the jet angle +30 degrees is shown with -+-, and for the jet angle +45 degrees is shown with -●-.

These figures show that the higher-harmonic amplitudes of the unsteady forces and moments are smaller than the first and second harmonic amplitudes. For axial forces at the radial positions of 88% span and 100% span, the difference between the first harmonic amplitude and the second harmonic amplitude is 86% whereas the difference between the first harmonic amplitude and the third harmonic amplitude is 99%. The first and second harmonic amplitudes of the unsteady forces and moments are thus sufficient for the structural dynamics.

4.4 Pressure Difference Computed with UNSFLO

This section gives computed time averaged pressure differences between the inlet flow and exit flow of the rotor cascade. The pressure difference is non-dimensionalized with the density, and the square of the relative inflow velocity. Figure 4.29 gives the pressure difference versus jet angles for the non-dimensional jet velocity of 1.5 and 2.0 at 88% span, and Figure 4.30 gives the pressure difference for 100% span. The figures include the steady pressure dif-

ference for comparison.

From these figures it can be seen that when the jet actuation has a jet velocity equal to 1.5 times the free-stream velocity and a jet angle of 0 degrees, the pressure difference reduces by 3% from the steady solution. This reduction in pressure difference is caused by the addition of mass flow through the jet injection and because the compressor characteristic for the lowest flow coefficient of NASA Rotor 35 is negatively sloped. When the jet actuation has a jet velocity of 2.0 times the free-stream velocity and a jet angle of 0 degree, the pressure difference reduces by 8% from the steady solution.

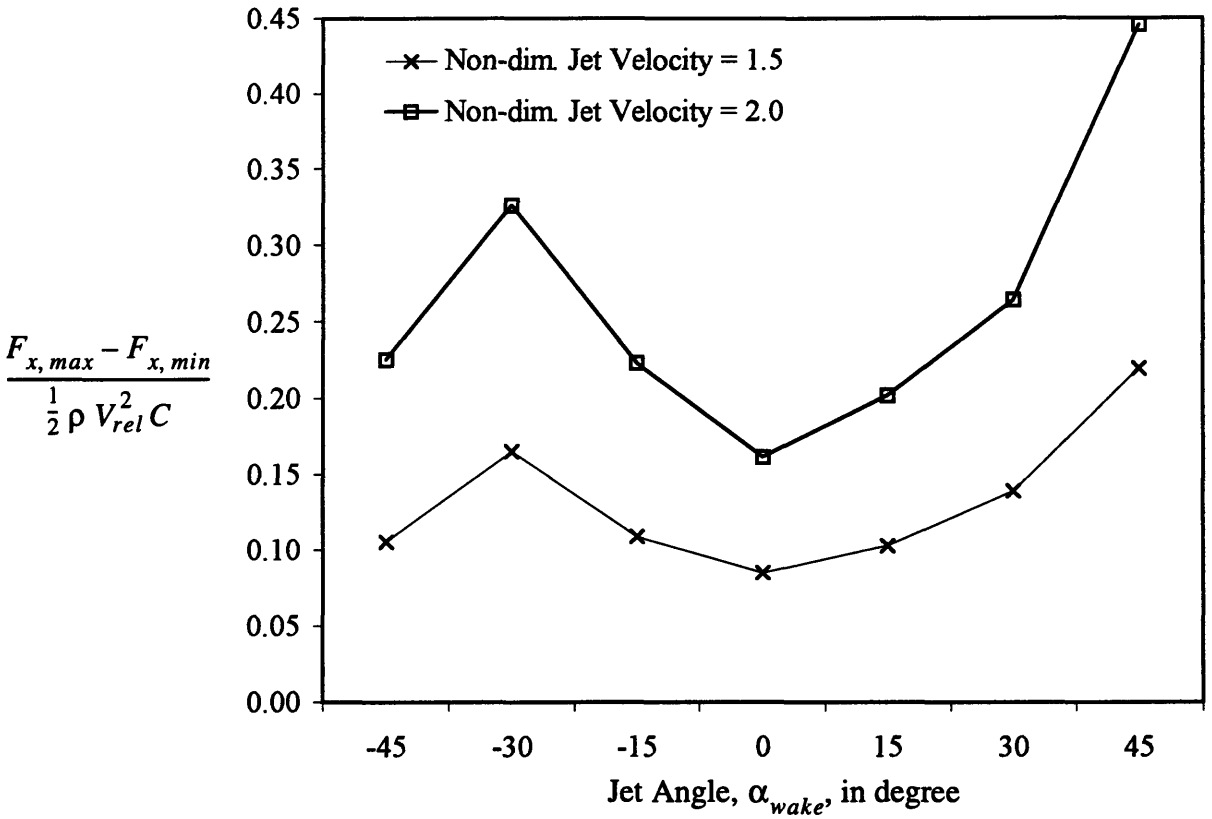

Figure 4.1: Axial force at 88% span for non-dimensional jet velocity equal to 1.5 and 2.0 versus jet angle

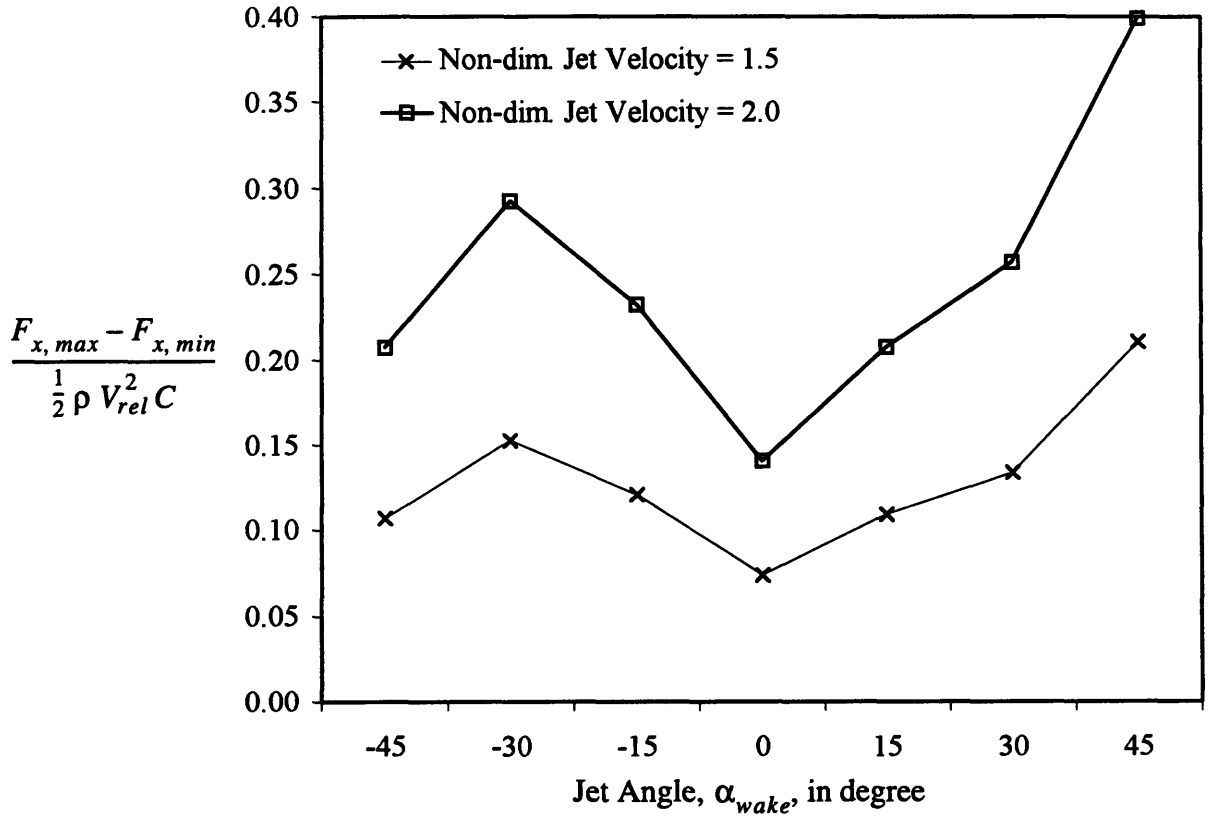

Figure 4.2: Axial force at 100% span for non-dimensional jet velocity equal to 1.5 and 2.0 versus jet angle

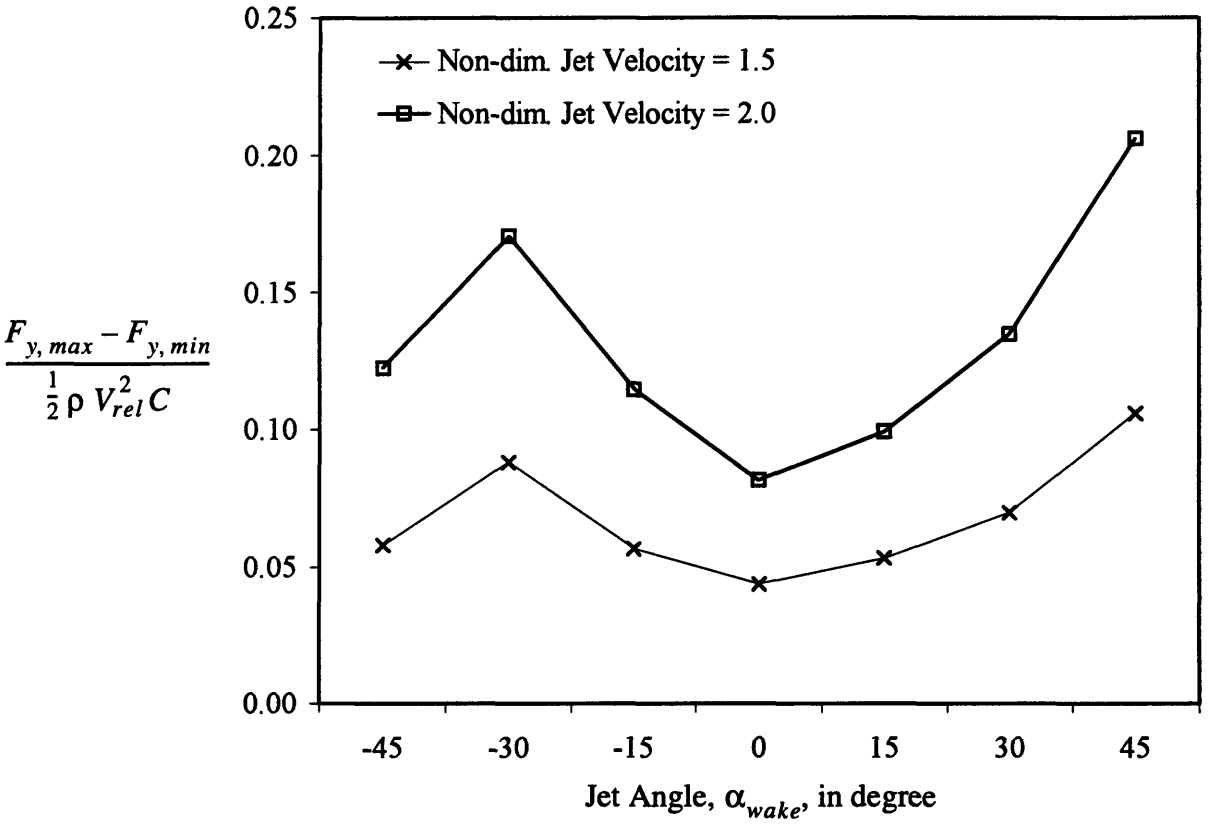

Figure 4.3: Tangential force at 88% span for non-dimensional jet velocity equal to 1.5 and 2.0 versus jet angle

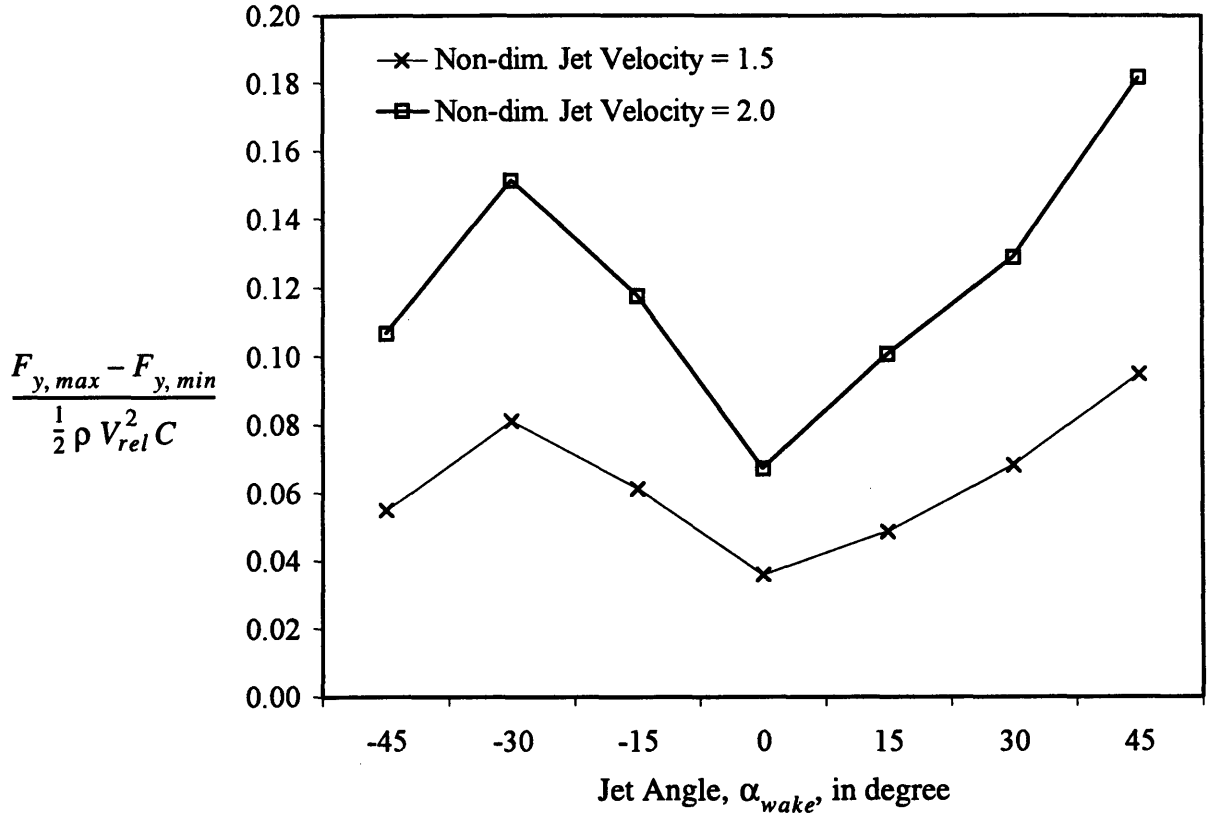

Figure 4.4: Tangential force at 100% span for non-dimensional jet velocity equal to 1.5 and 2.0 versus jet angle

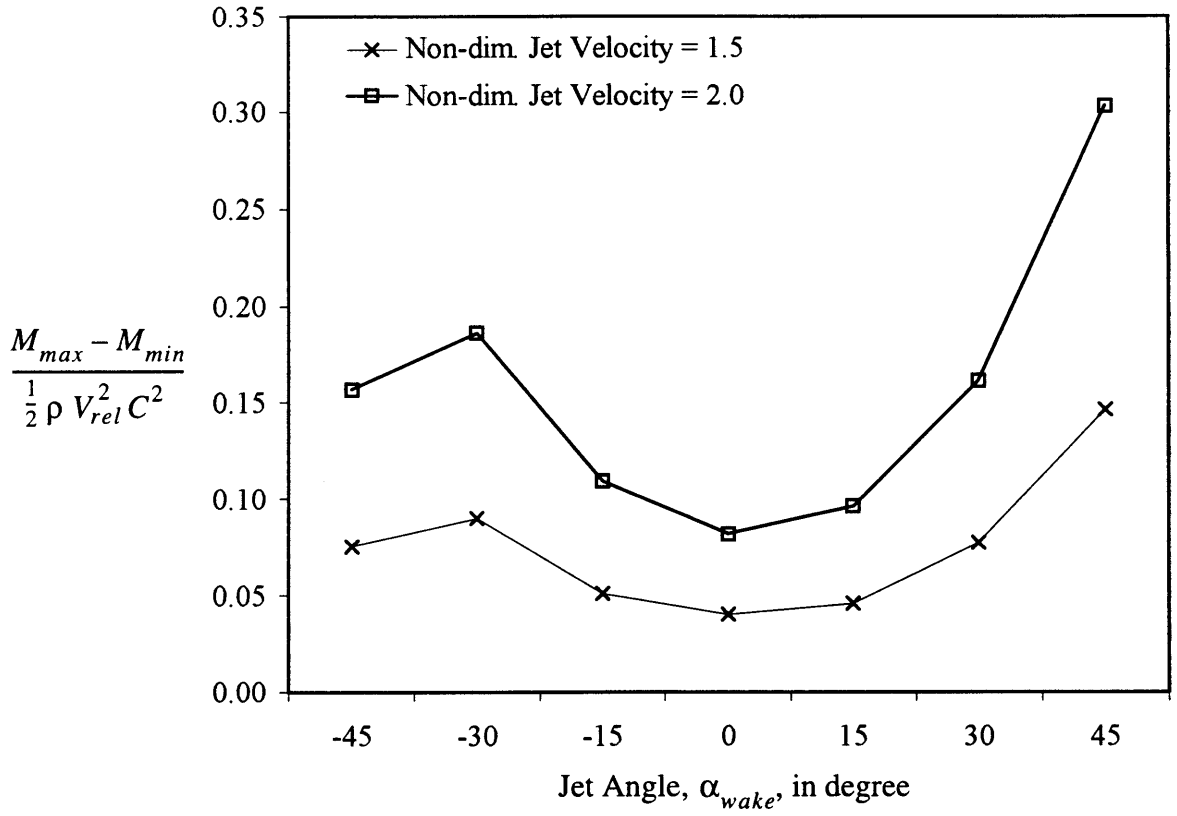

Figure 4.5: Moment at 88% span for non-dimensional jet velocity equal to 1.5 and 2.0 versus jet angle

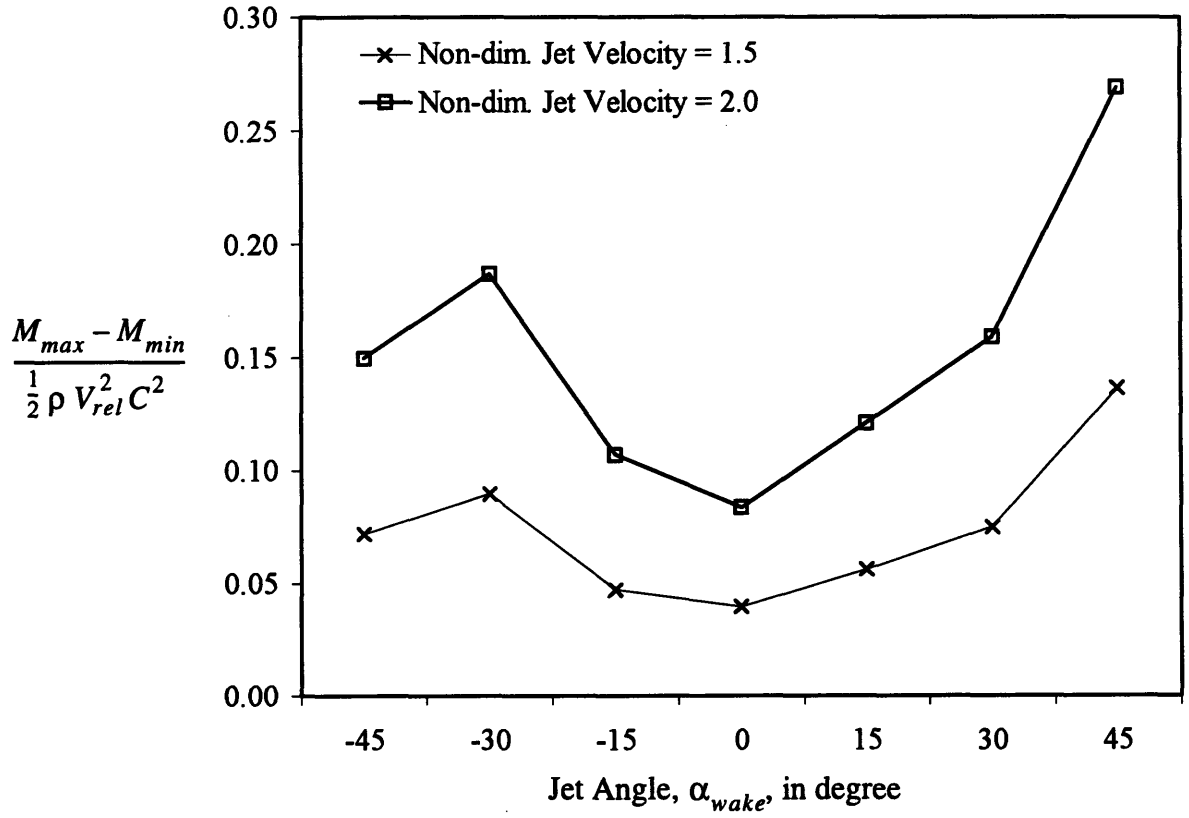

Figure 4.6: Moment at 100% span for non-dimensional jet velocity equal to 1.5 and 2.0 versus jet angle

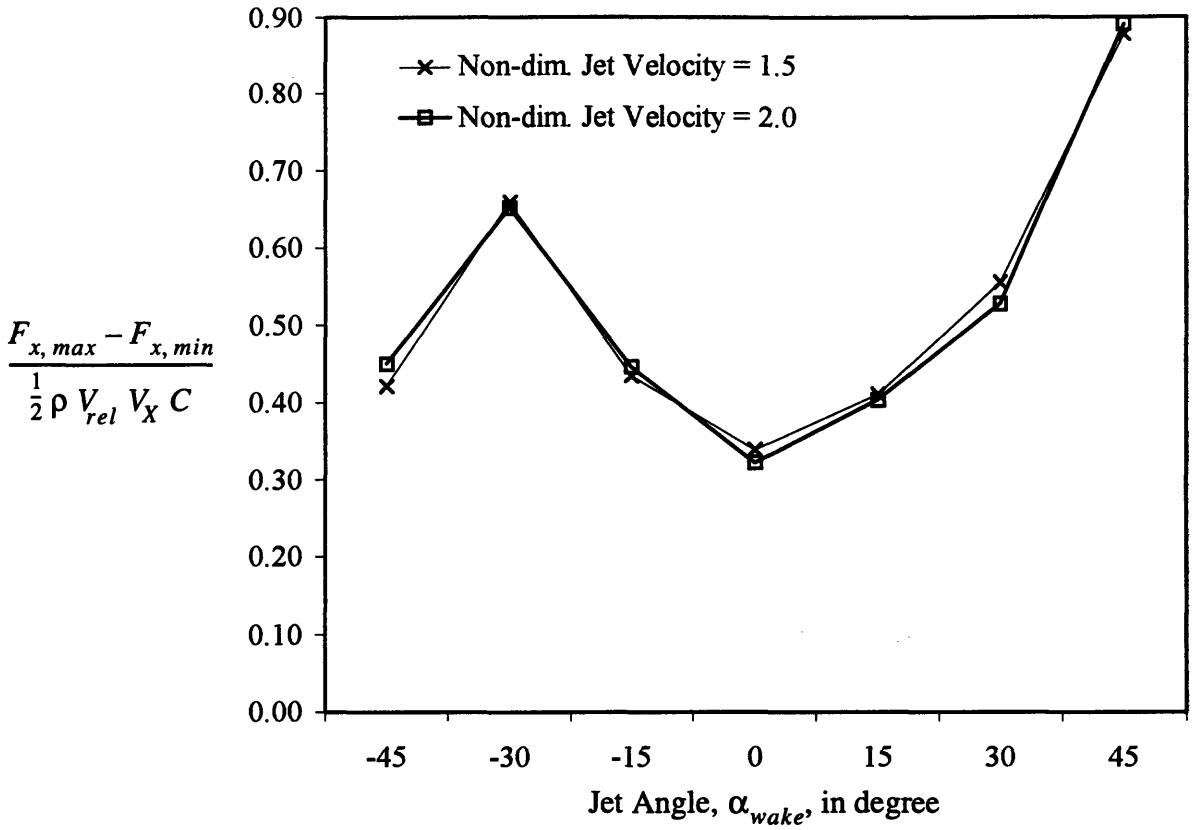

Figure 4.7: Axial force at 88% span for non-dimensional jet velocity equal to 1.5 and 2.0 versus jet angle

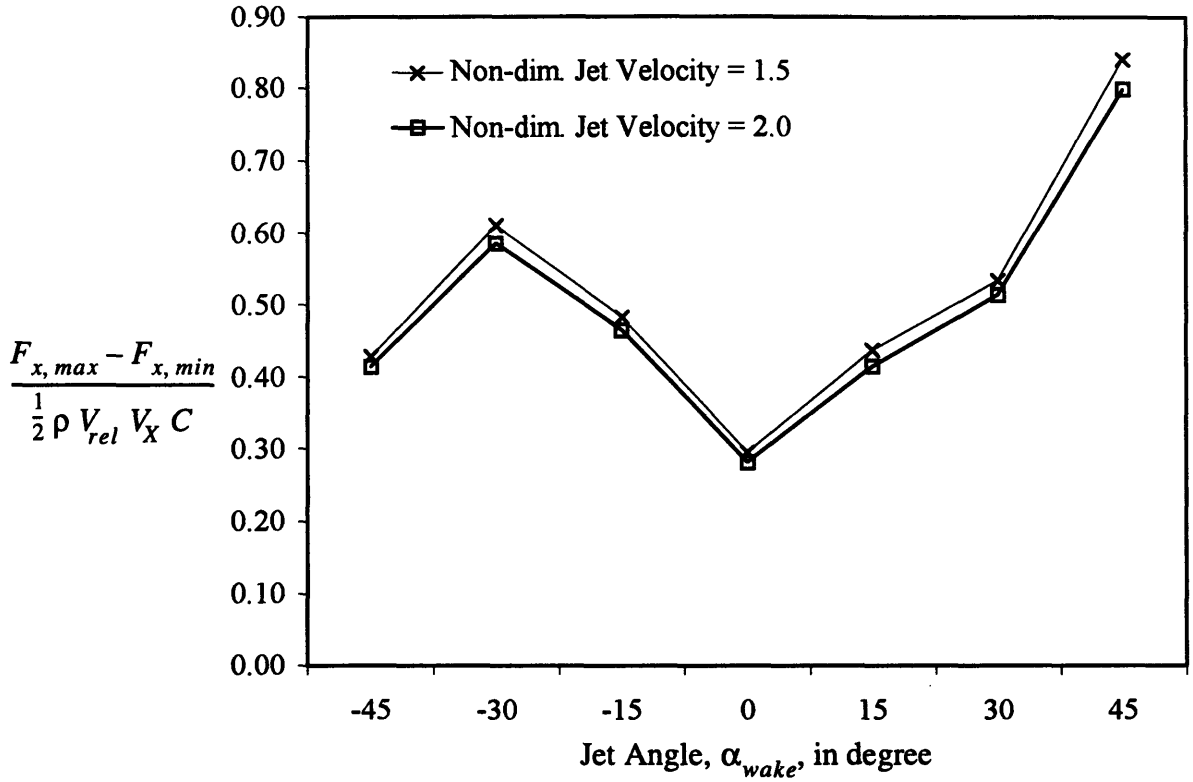

Figure 4.8: Axial force at 100% span for non-dimensional jet velocity equal to 1.5 and 2.0 versus jet angle

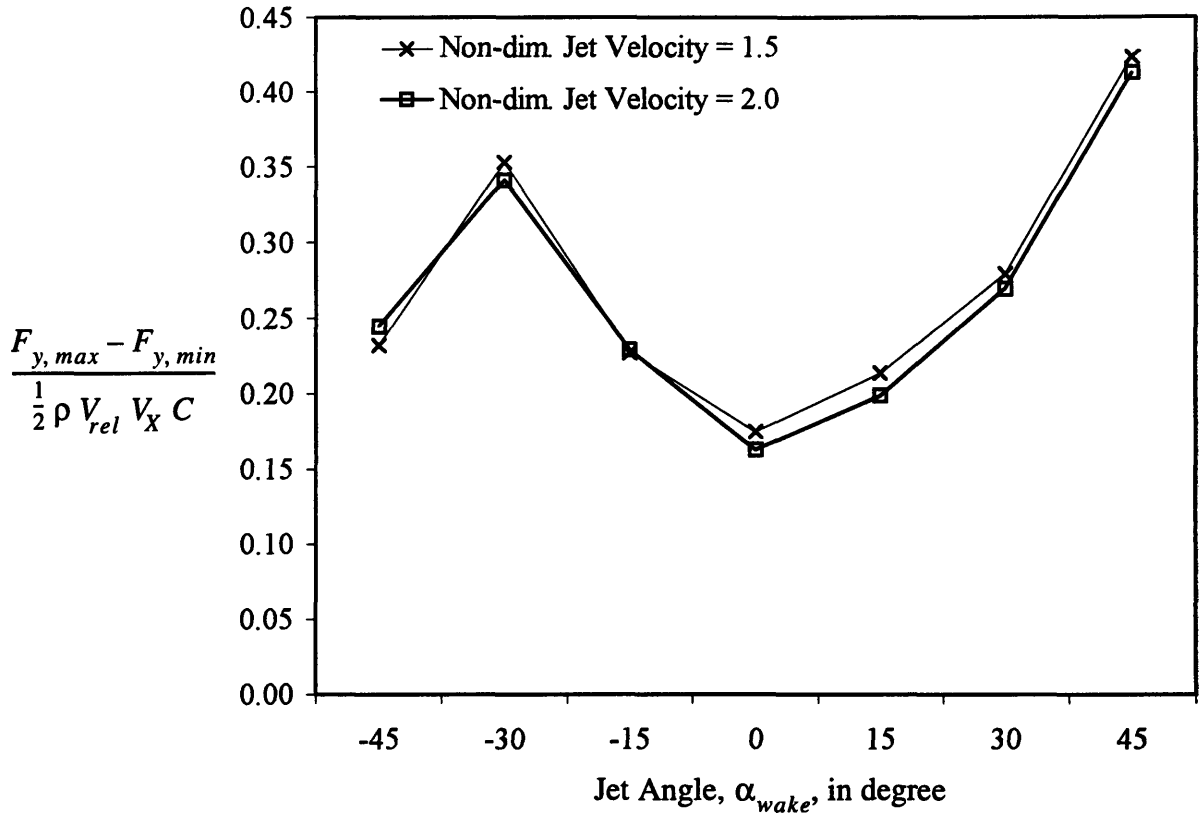

Figure 4.9: Tangential force at 88% span for non-dimensional jet velocity equal to 1.5 and 2.0 versus jet angle

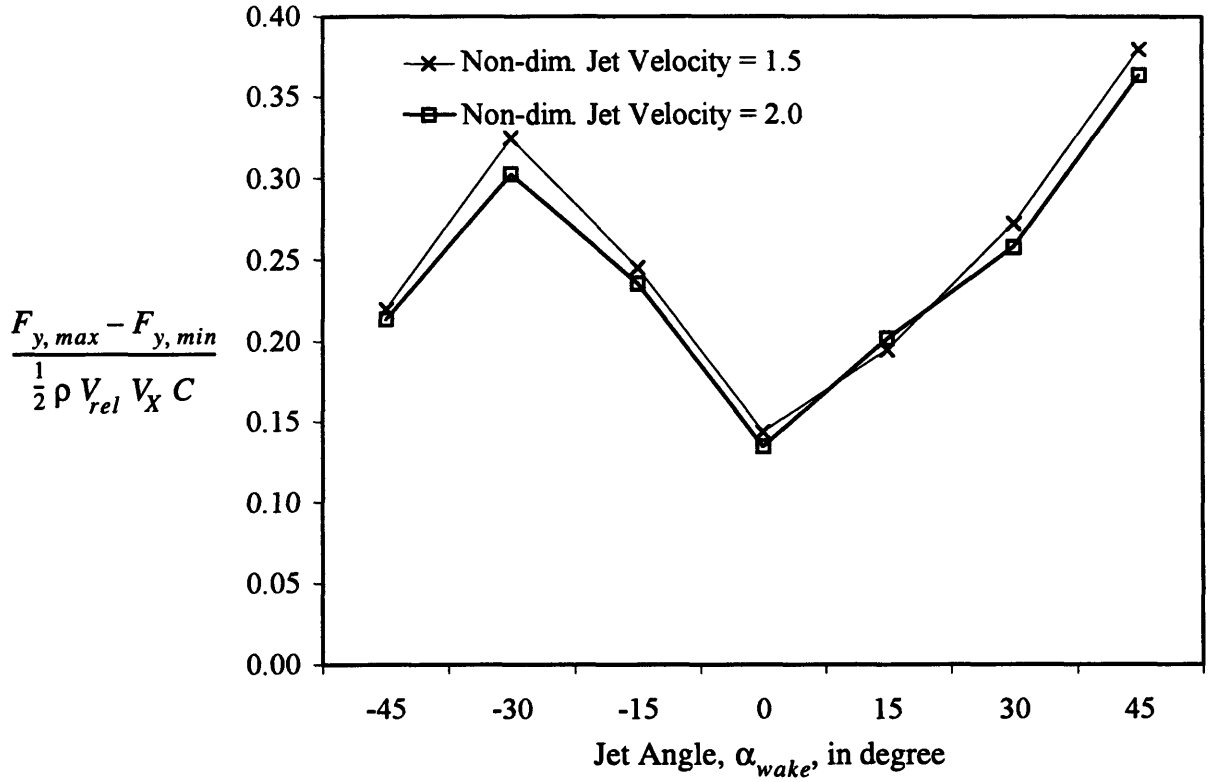

Figure 4.10: Tangential force at 100% span for non-dimensional jet velocity equal to 1.5 and 2.0 versus jet angle

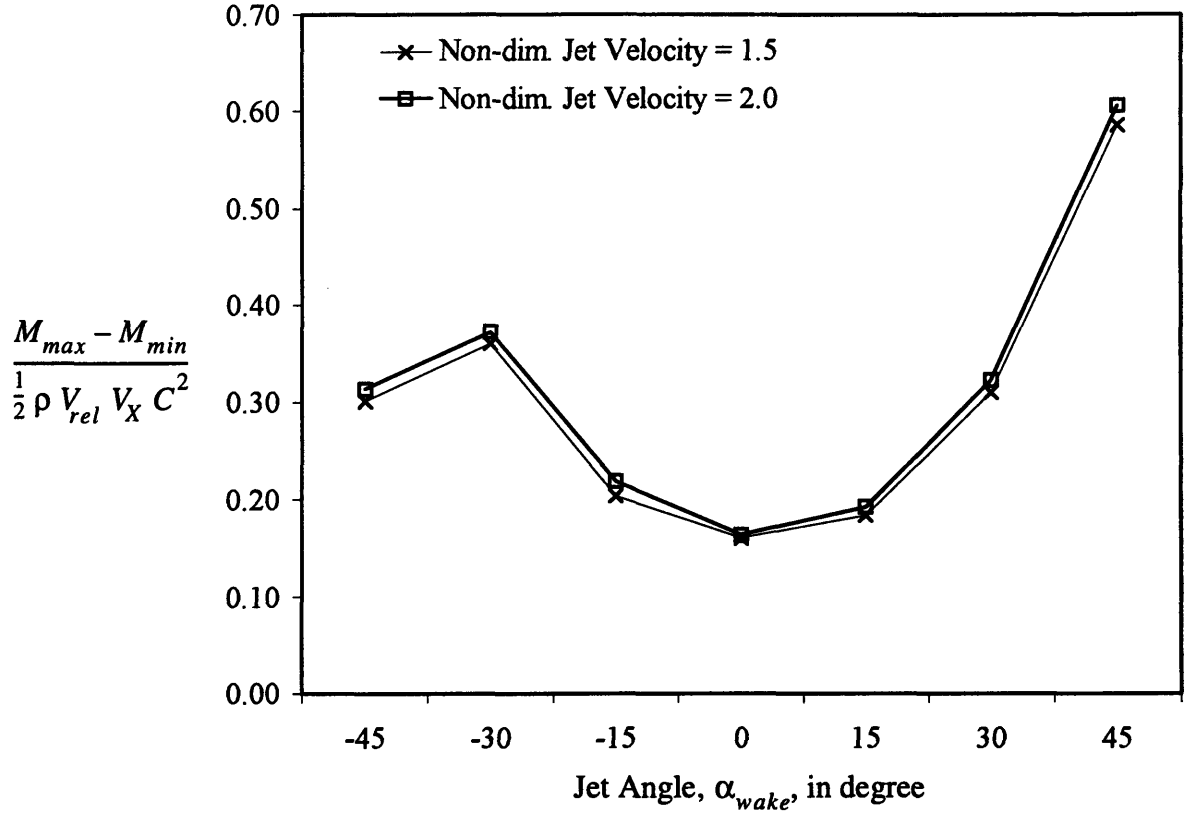

Figure 4.11: Moment at 88% span for non-dimensional jet velocity equal to 1.5 and 2.0 versus jet angle

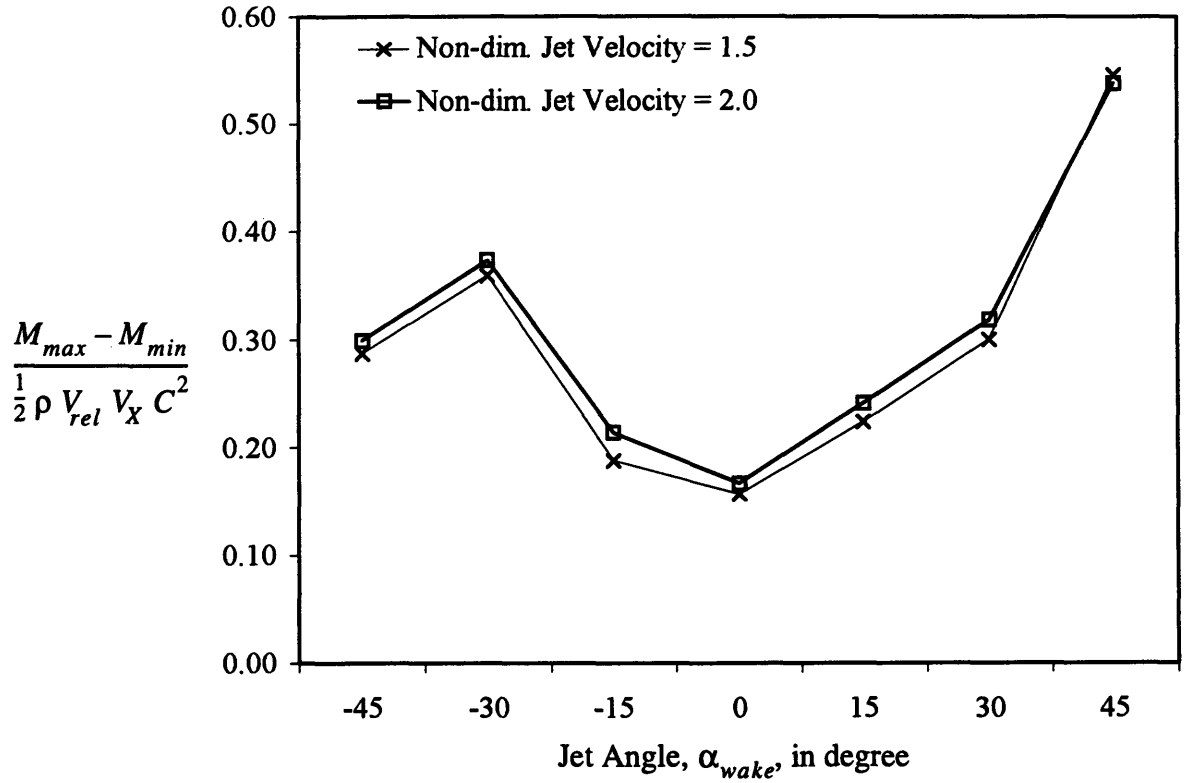

Figure 4.12: Moment at 100% span for non-dimensional jet velocity equal to 1.5 and 2.0 versus jet angle

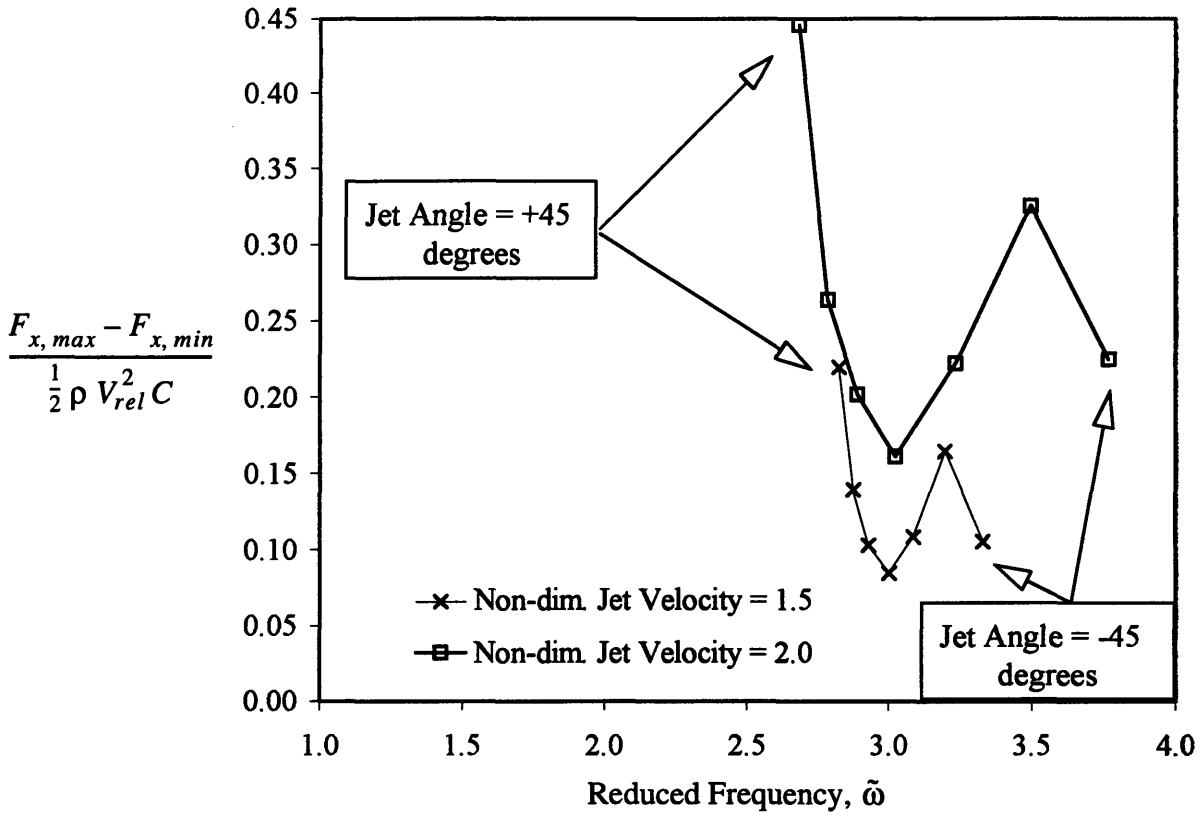

Figure 4.13: Axial force at 88% span for non-dimensional jet velocity equal to 1.5 and 2.0 versus reduced frequency for different jet angles

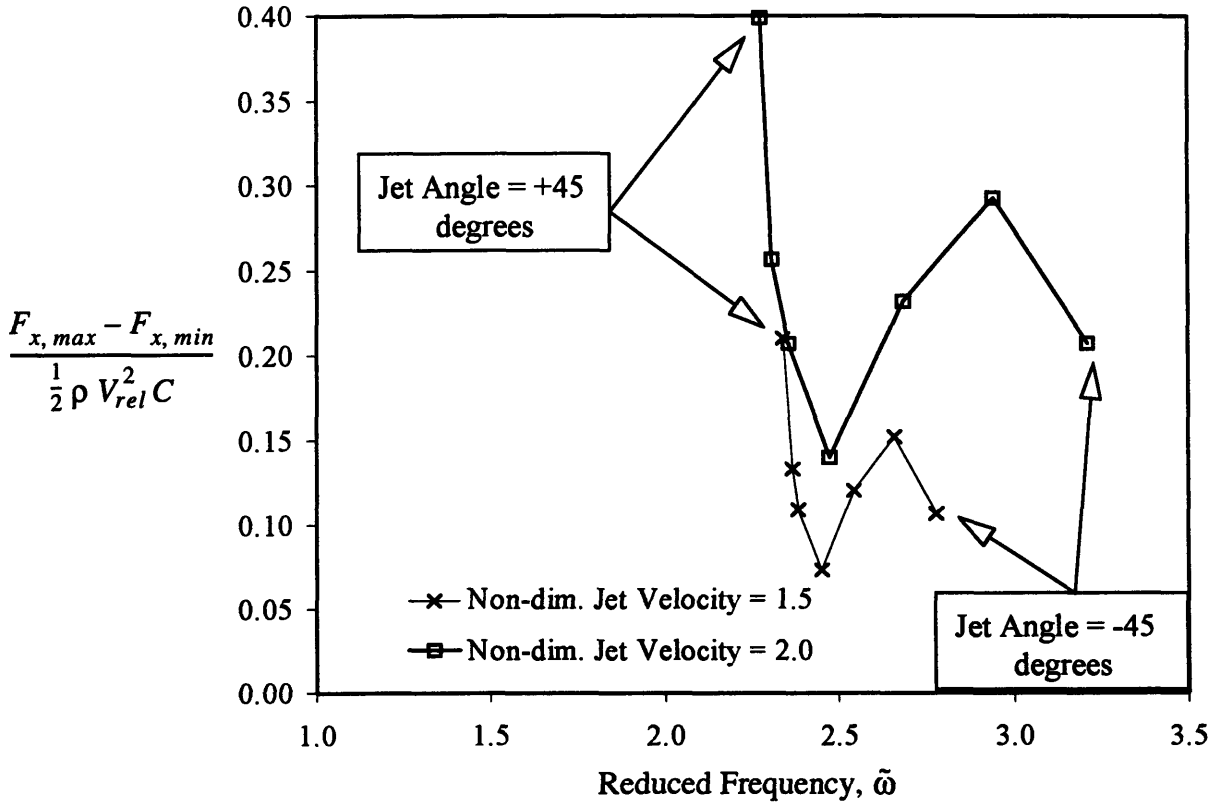

Figure 4.14: Axial force at 100% span for non-dimensional jet velocity equal to 1.5 and 2.0 versus reduced frequency for different jet angles

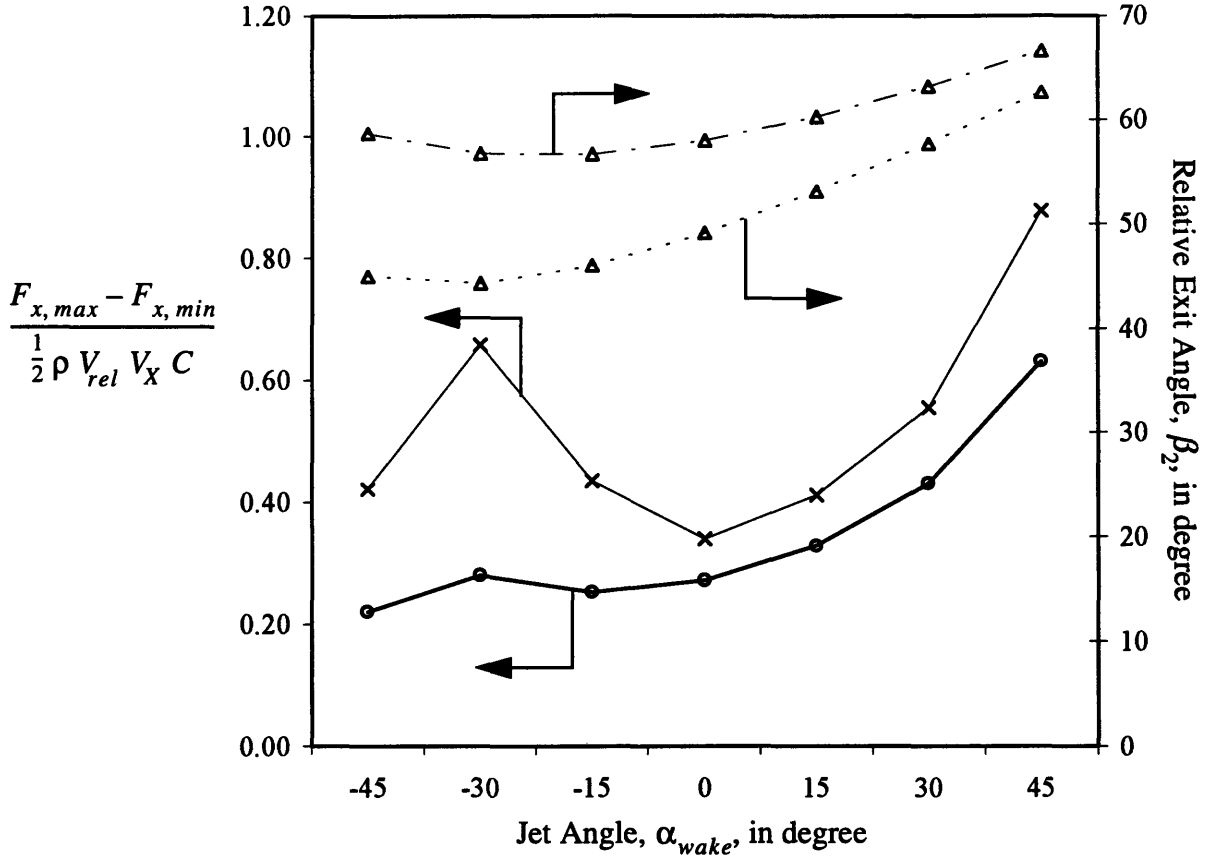

Figure 4.15: Axial force at 88% span for non-dimensional jet velocity equal to 1.5 and 2.0 versus jet angle. (UNSFLO... -✕-, quasi-steady analysis... -○-, exit angle for quasi-steady analysis... - △ -, inlet angle for quasi-steady analysis... -▲-)

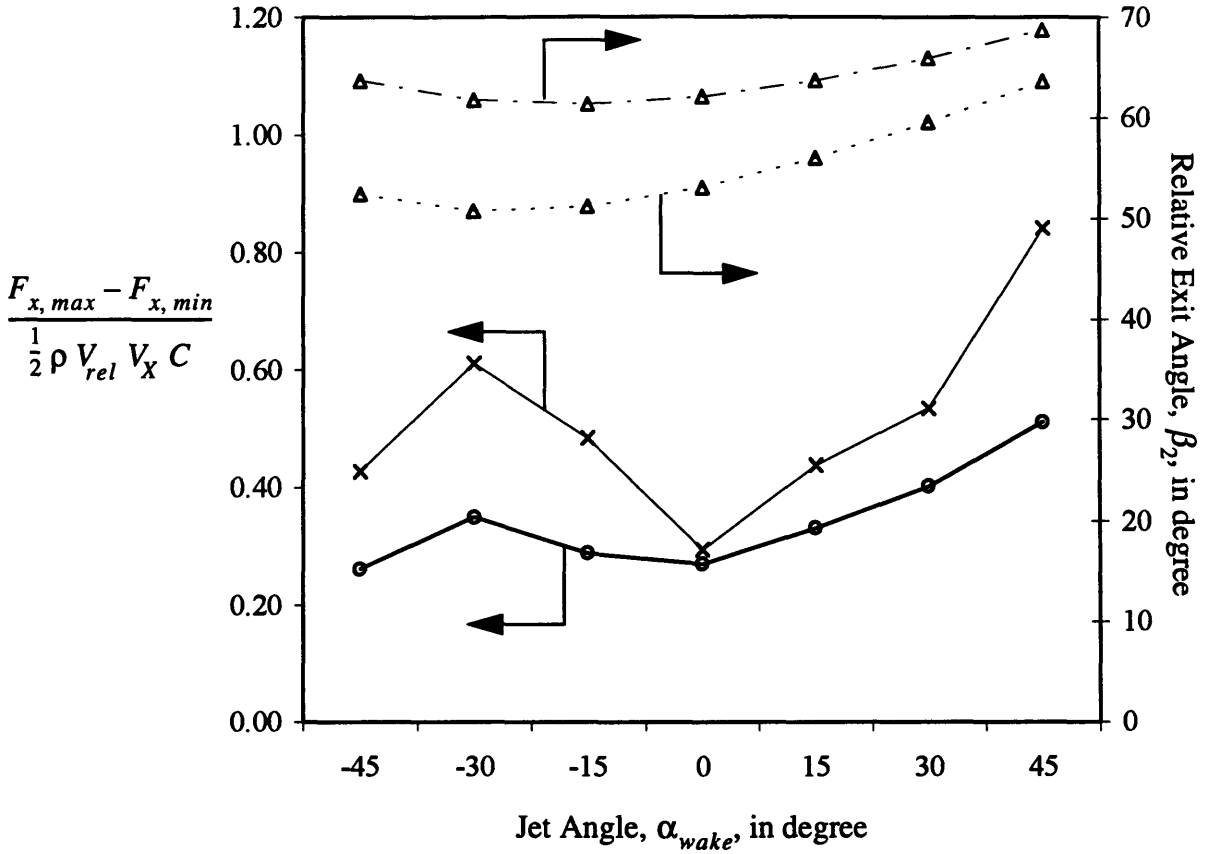

Figure 4.16: Axial force at 100% span for non-dimensional jet velocity equal to 1.5 and 2.0 versus jet angle. (UNSFLO... -✕-, quasi-steady analysis... -⊖-, exit angle for quasi-steady analysis... - Δ -, inlet angle for quasi-steady analysis... -Δ-)

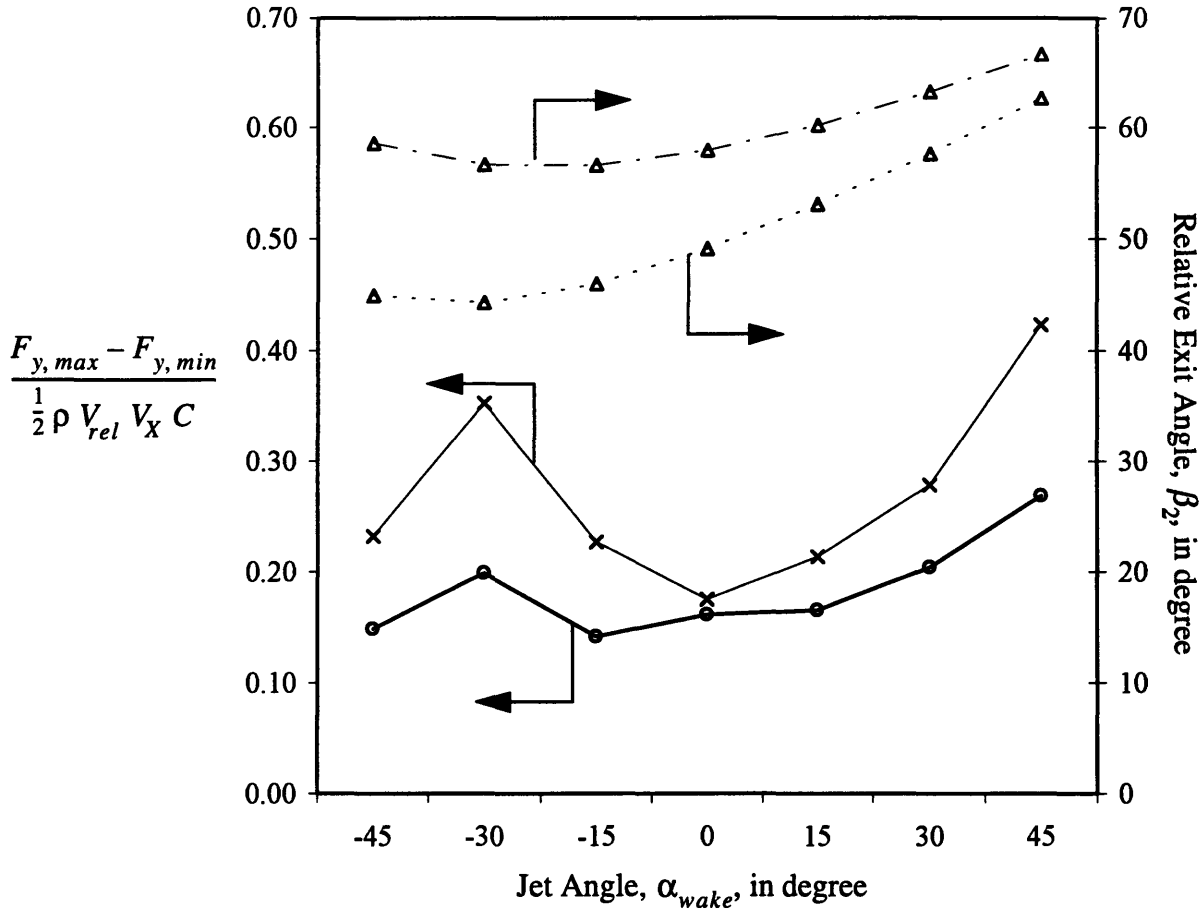

Figure 4.17: Tangential force at 88% span for non-dimensional jet velocity equal to 1.5 and 2.0 versus jet angle. (UNSFLO... -✕-, quasi-steady analysis... -⊖-, exit angle for quasi-steady analysis... - Δ -, inlet angle for quasi-steady analysis... -Δ-)

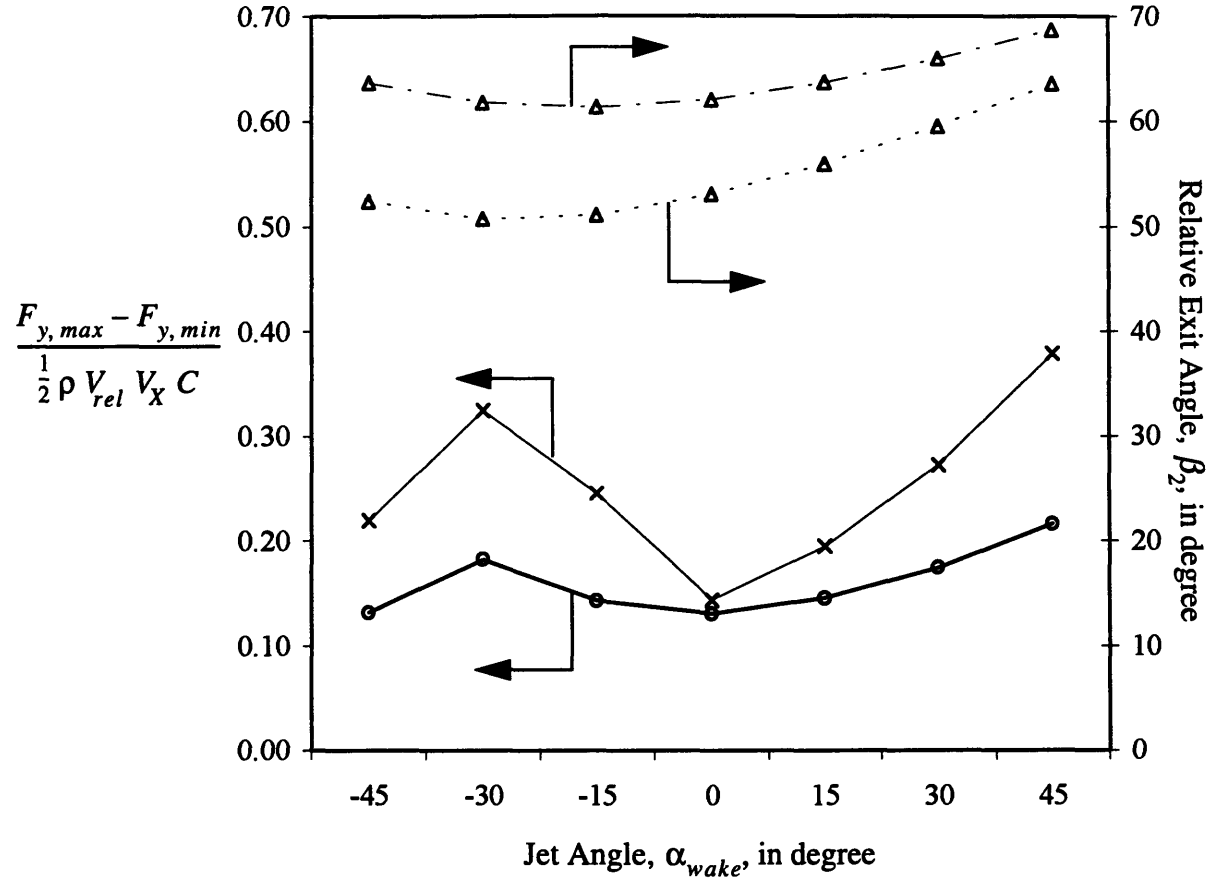

Figure 4.18: Tangential force at 100% span for non-dimensional jet velocity equal to 1.5 and 2.0 versus jet angle. (UNSFLO... -✕-, quasi-steady analysis... -⊖-, exit angle for quasi-steady analysis... - Δ -, inlet angle for quasi-steady analysis... -Δ-)

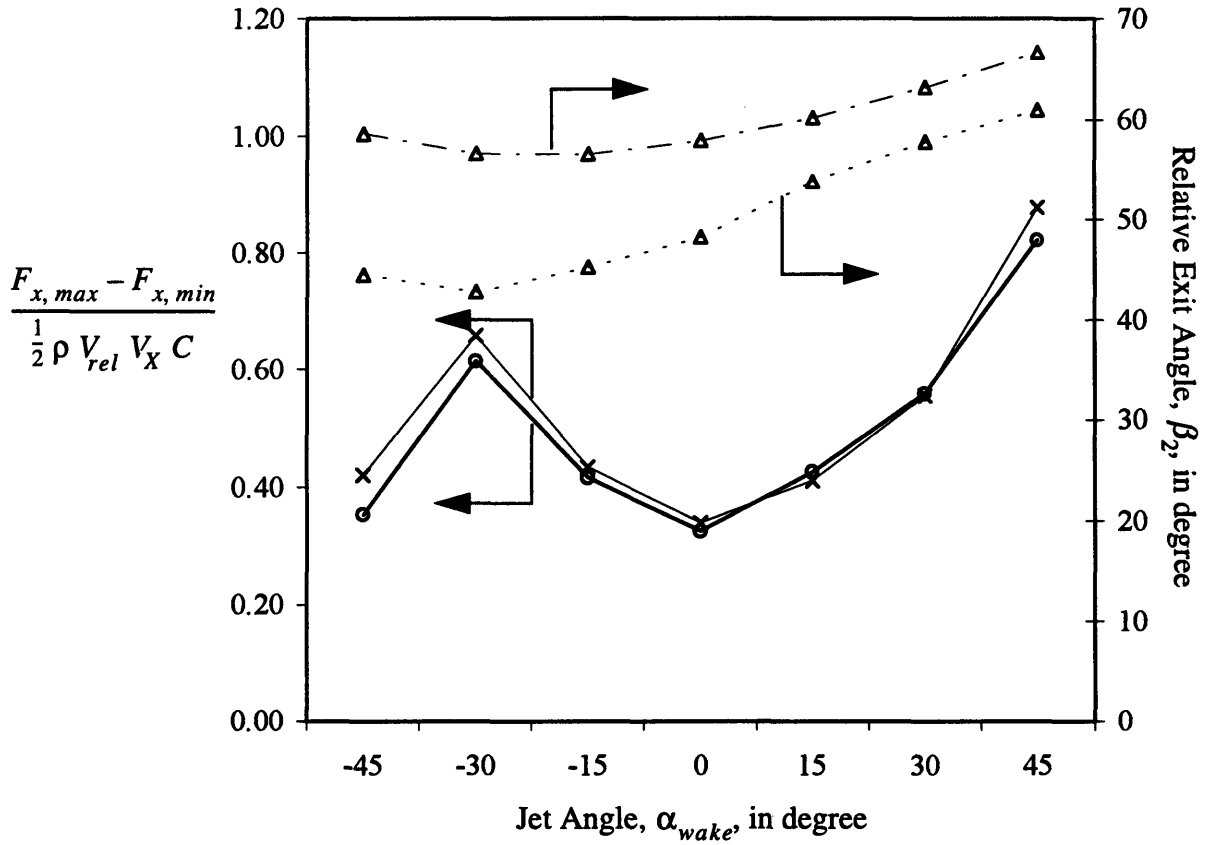

Figure 4.19: Axial force at 88% span for non-dimensional jet velocity equal to 1.5 and 2.0 versus jet angle. (UNSFLO... -✕-, quasi-steady analysis... -⊖-, exit angle for quasi-steady analysis... - Δ -, inlet angle for quasi-steady analysis... -Δ-)

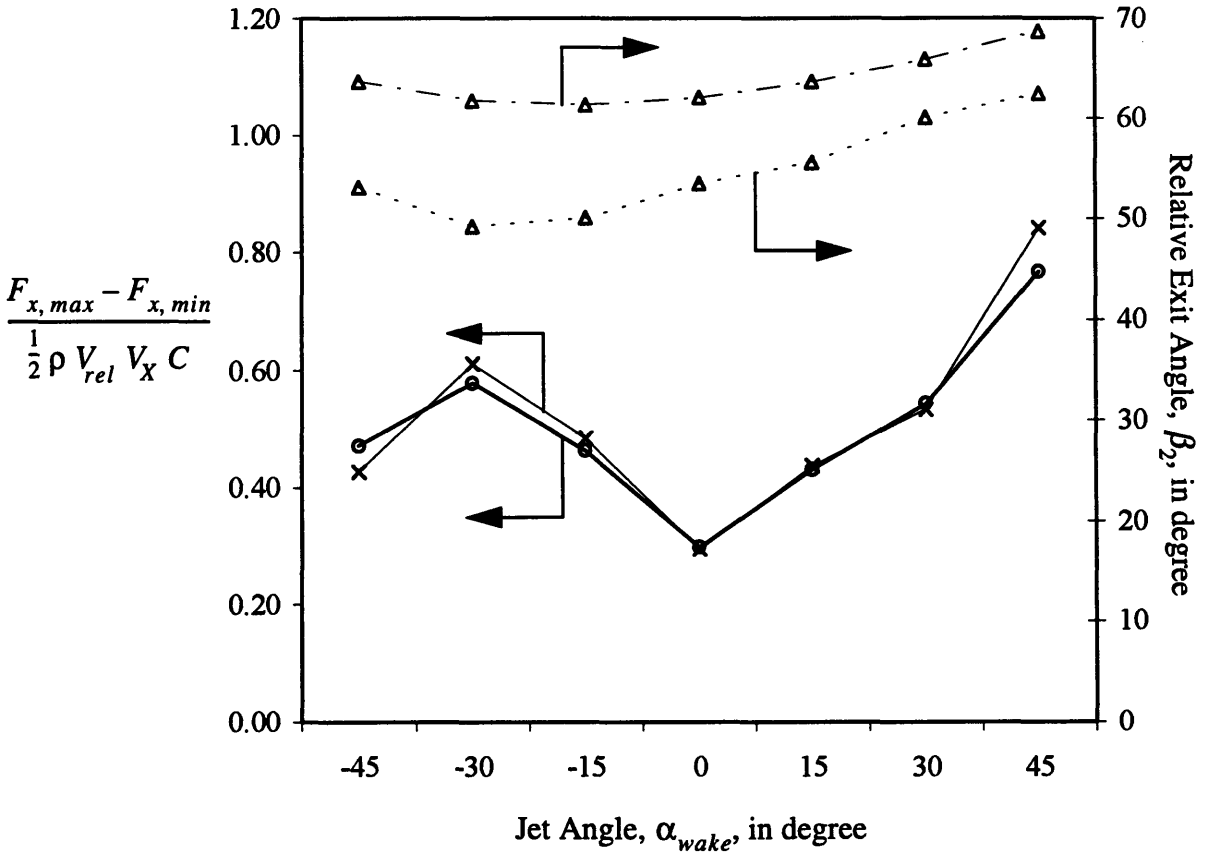

Figure 4.20: Axial force at 100% span for non-dimensional jet velocity equal to 1.5 and 2.0 versus jet angle. (UNSFLO... -✕-, quasi-steady analysis... -⊖-, exit angle for quasi-steady analysis... - Δ -, inlet angle for quasi-steady analysis... -Δ-)

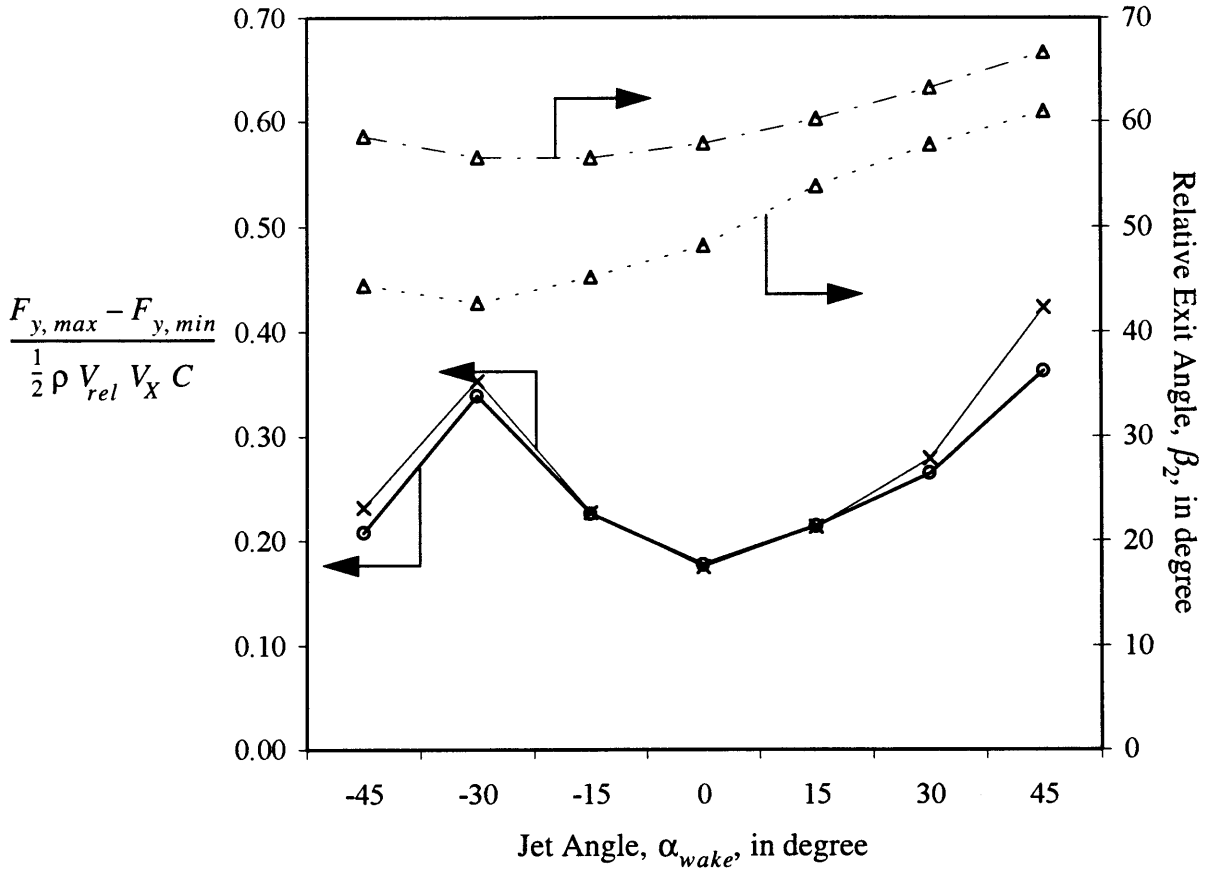

Figure 4.21: Tangential force at 88% span for non-dimensional jet velocity equal to 1.5 and 2.0 versus jet angle. (UNSFLO... -✕-, quasi-steady analysis... -○-, exit angle for quasi-steady analysis... - Δ -, inlet angle for quasi-steady analysis... -Δ-)

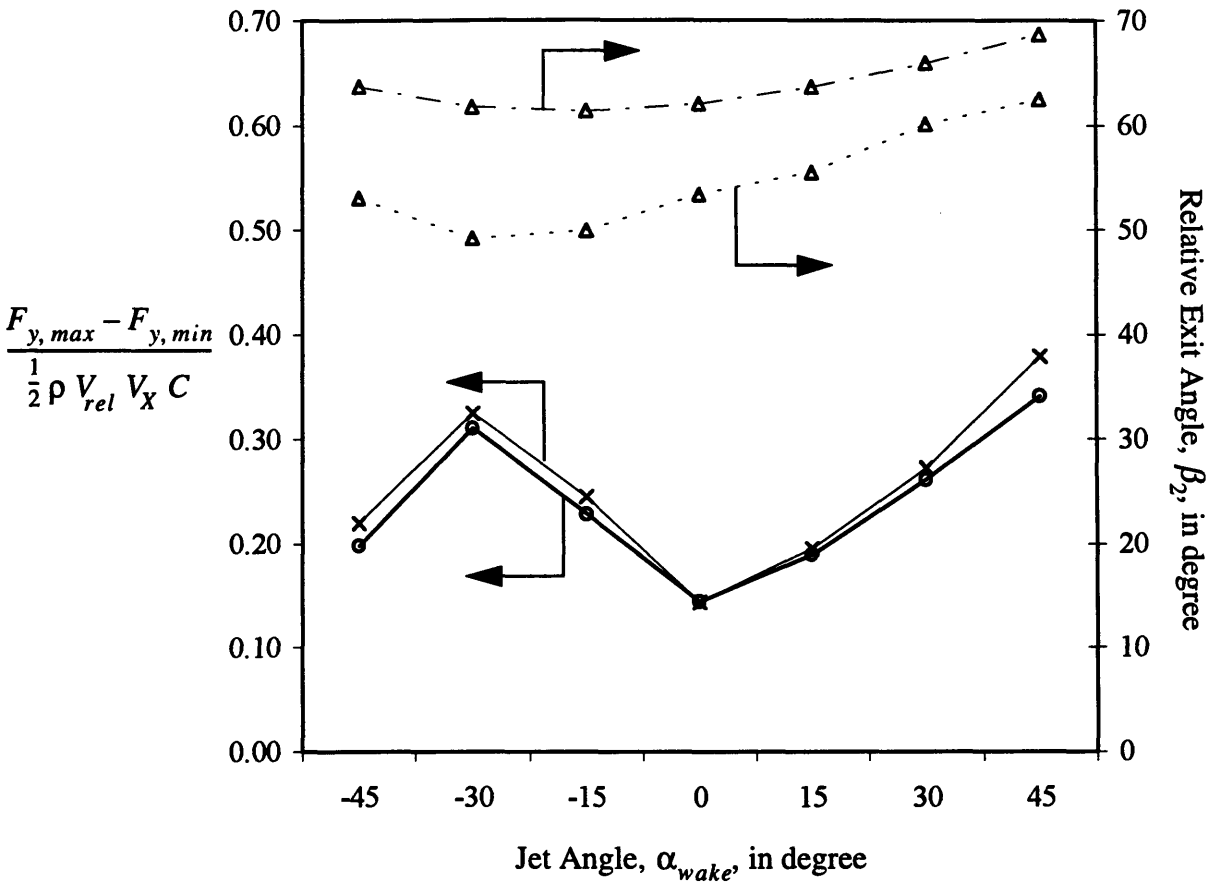

Figure 4.22: Tangential force at 100% span for non-dimensional jet velocity equal to 1.5 and 2.0 versus jet angle. (UNSFLO... -✕-, quasi-steady analysis... -⊖-, exit angle for quasi-steady analysis... - Δ -, inlet angle for quasi-steady analysis... -Δ-)

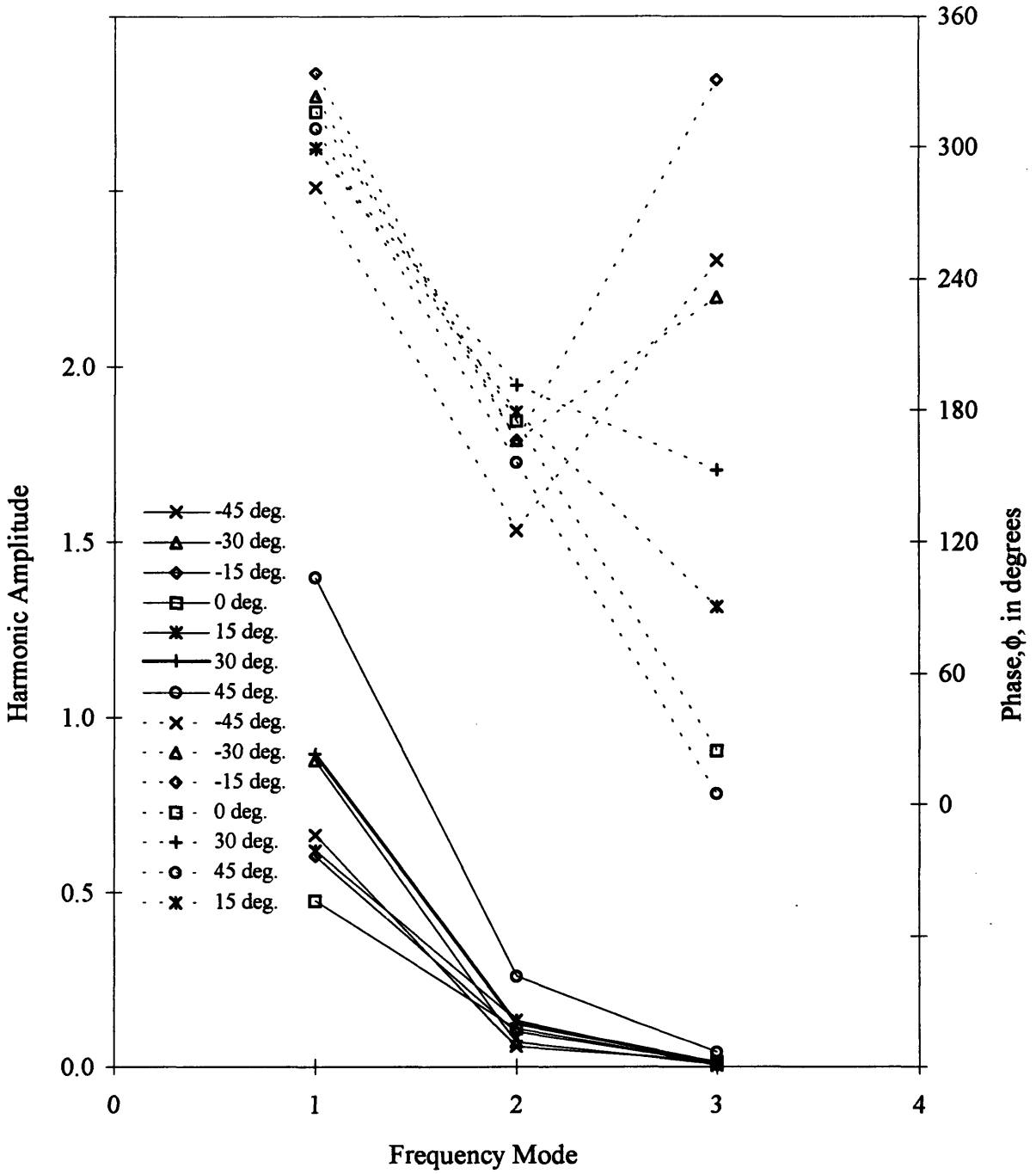

Figure 4.23: Amplitudes of Harmonics and Phase for the axial force at 88% span with a non-dimensional jet velocity equal to 1.5 versus frequency mode

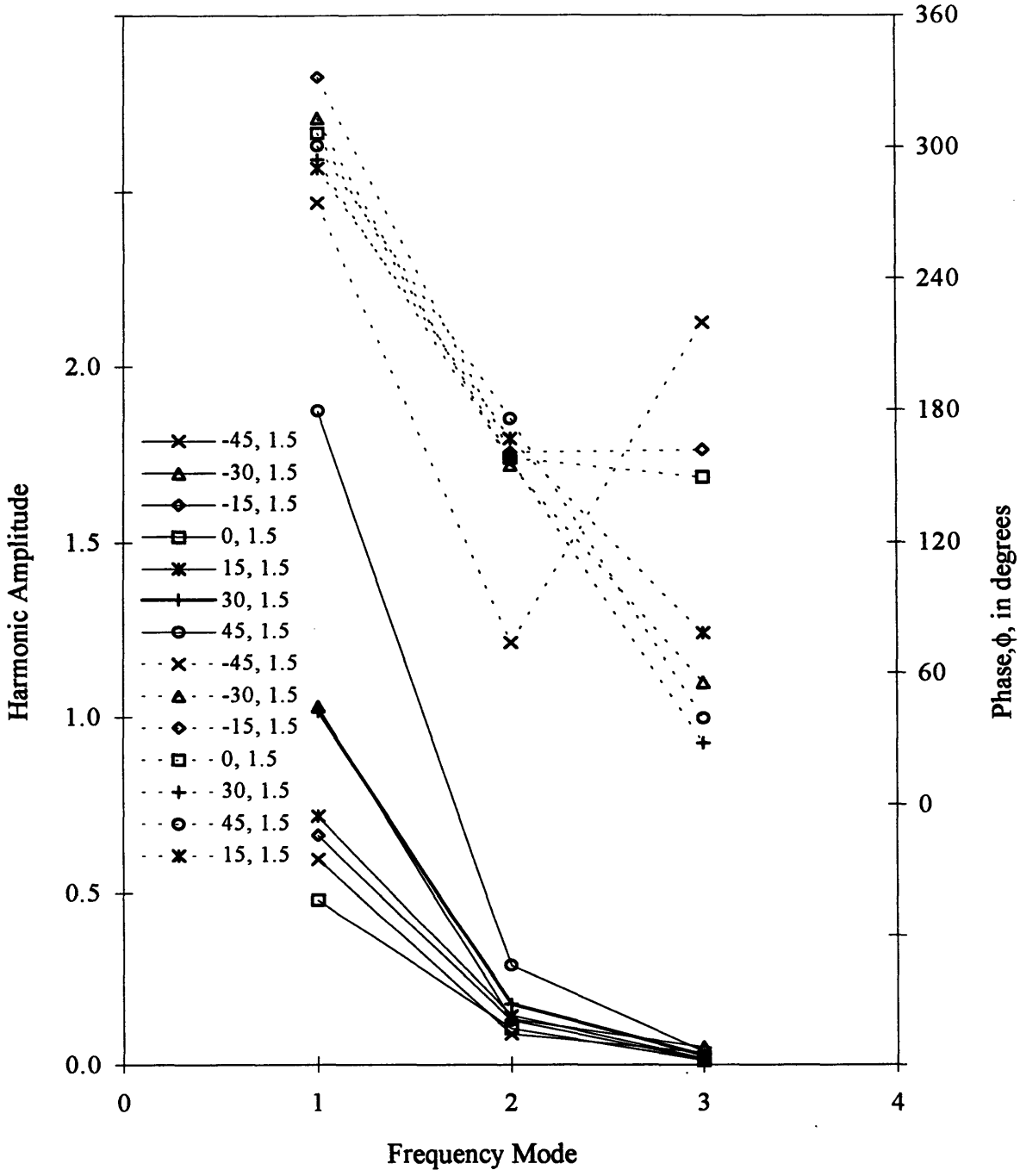

Figure 4.24: Amplitudes of Harmonics and Phase for the axial force at 100% span with a non-dimensional jet velocity equal to 1.5 versus frequency mode

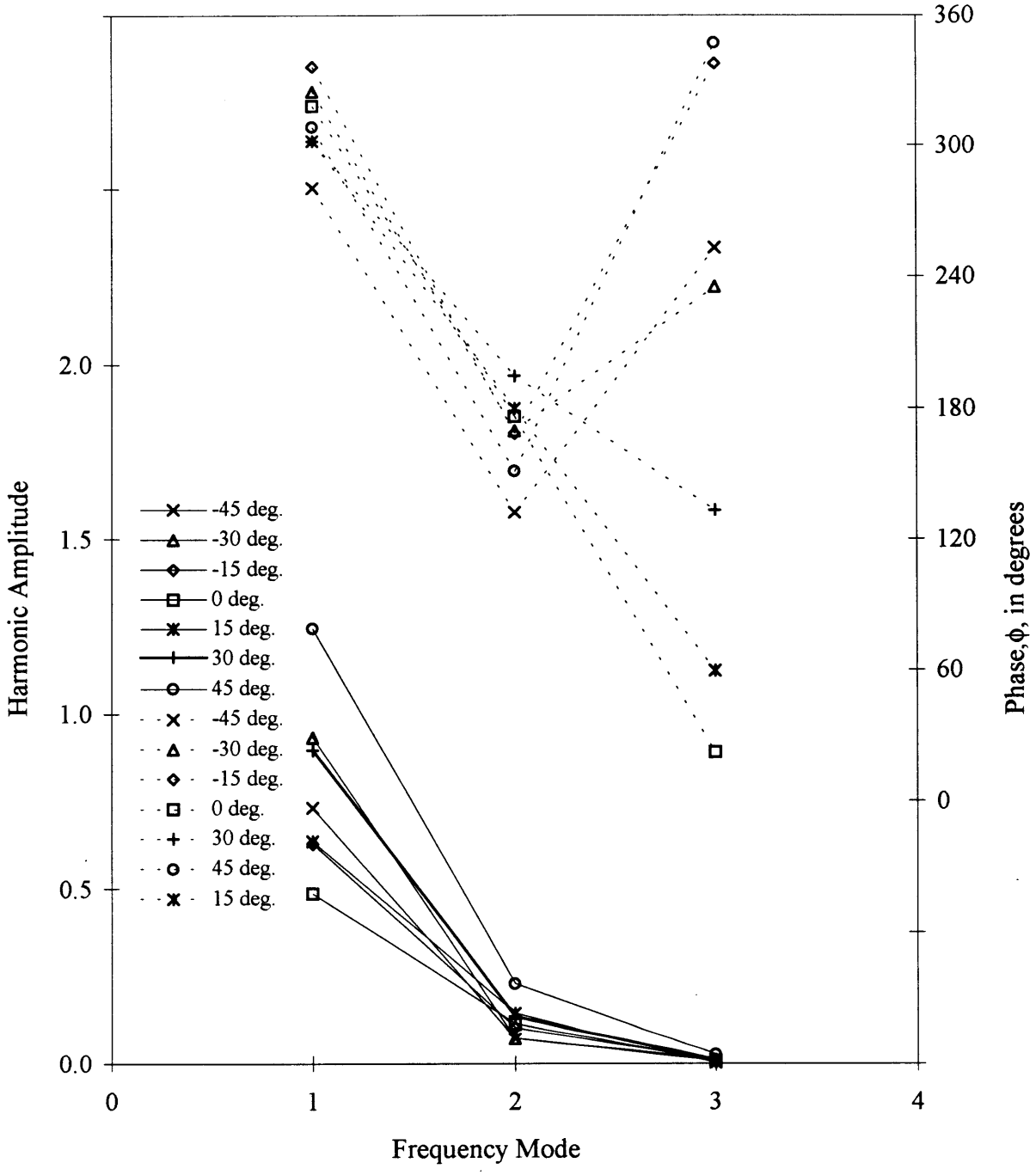

Figure 4.25: Amplitudes of Harmonics and Phase for the tangential force at 88% span with a non-dimensional jet velocity equal to 1.5 versus frequency mode

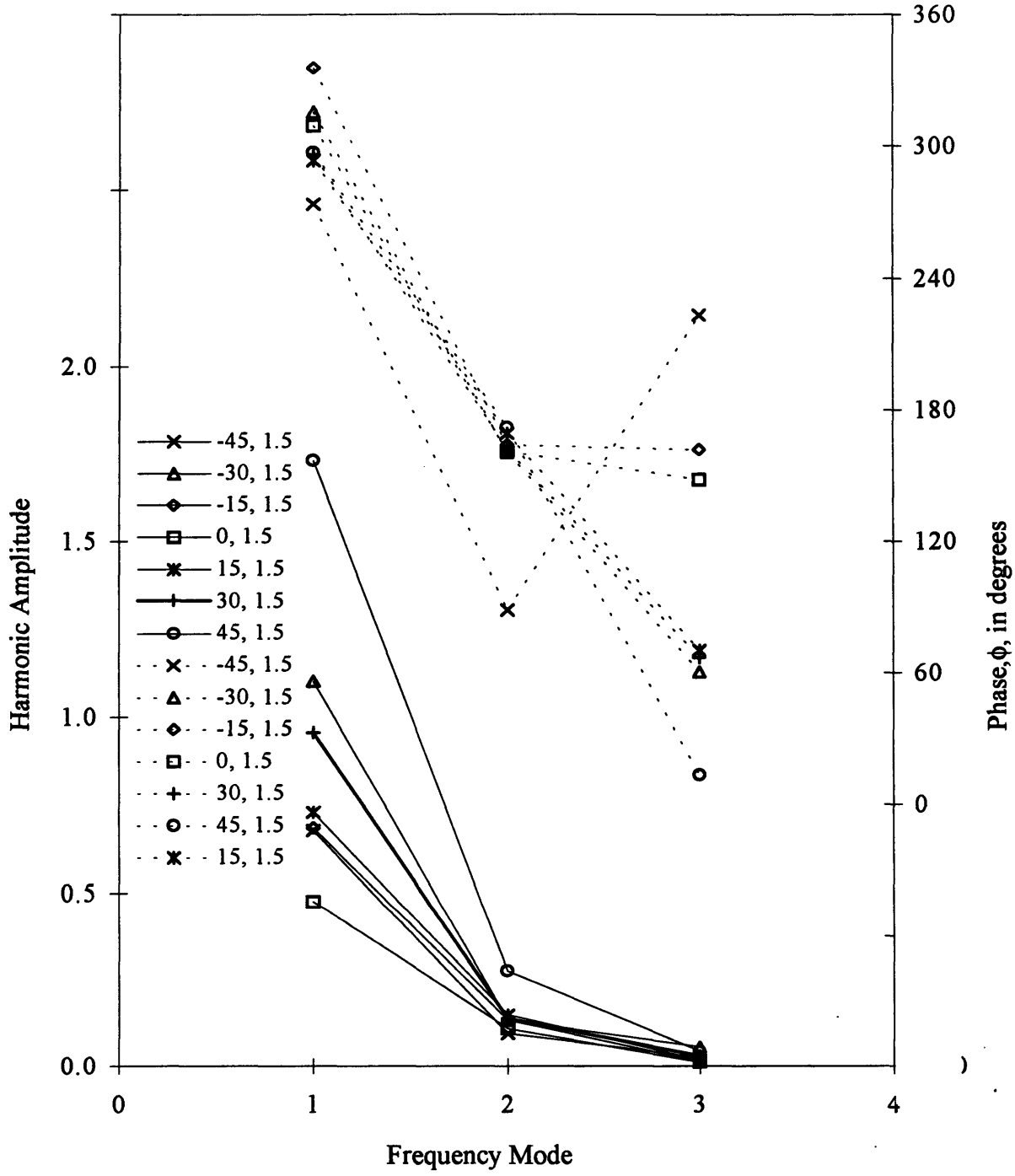

Figure 4.26: Amplitudes of Harmonics and Phase for the tangential force at 100% span with a non-dimensional jet velocity equal to 1.5 versus frequency mode

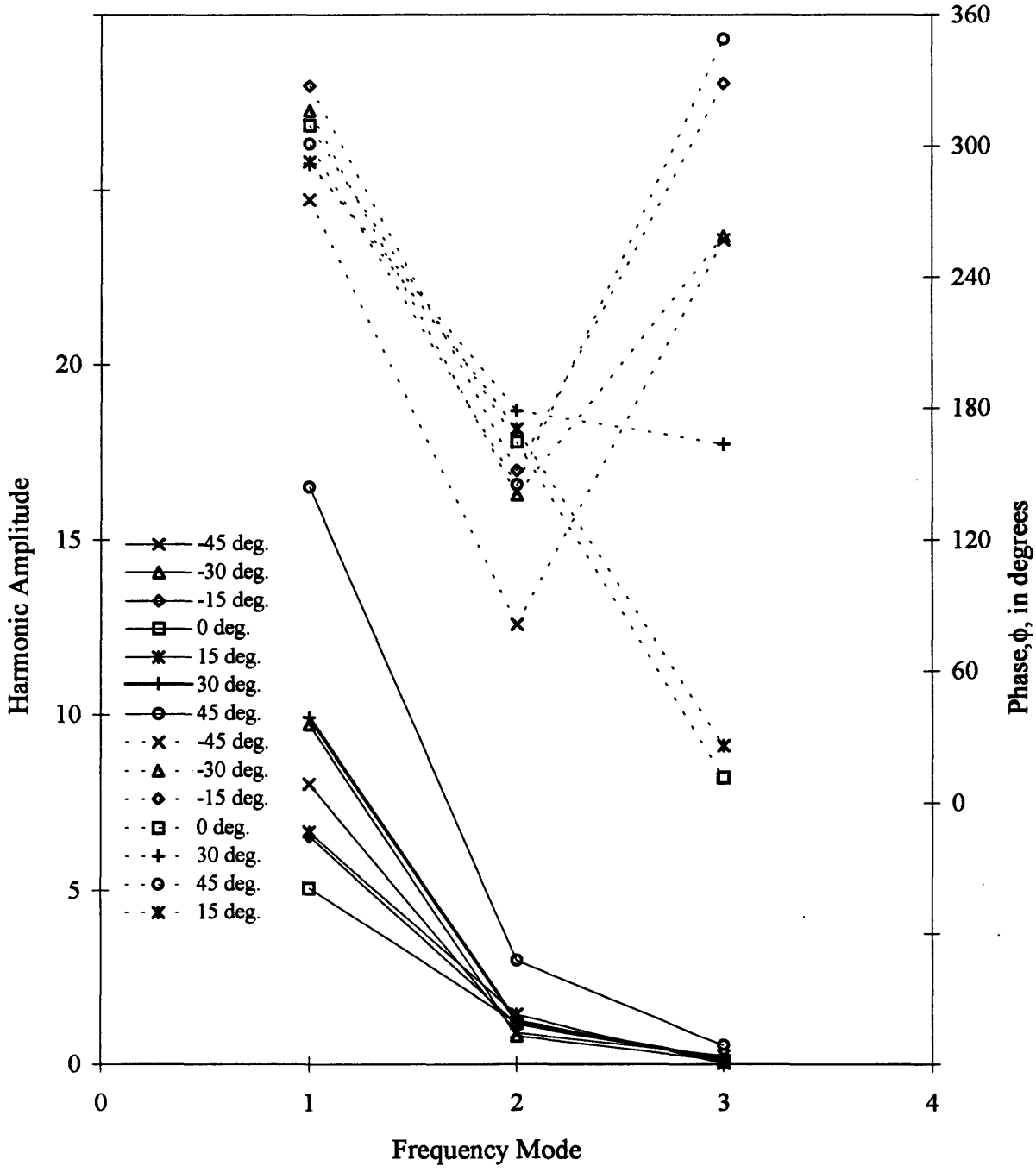

Figure 4.27: Amplitudes of Harmonics and Phase for the moment at 88% span with a non-dimensional jet velocity equal to 1.5 versus frequency mode

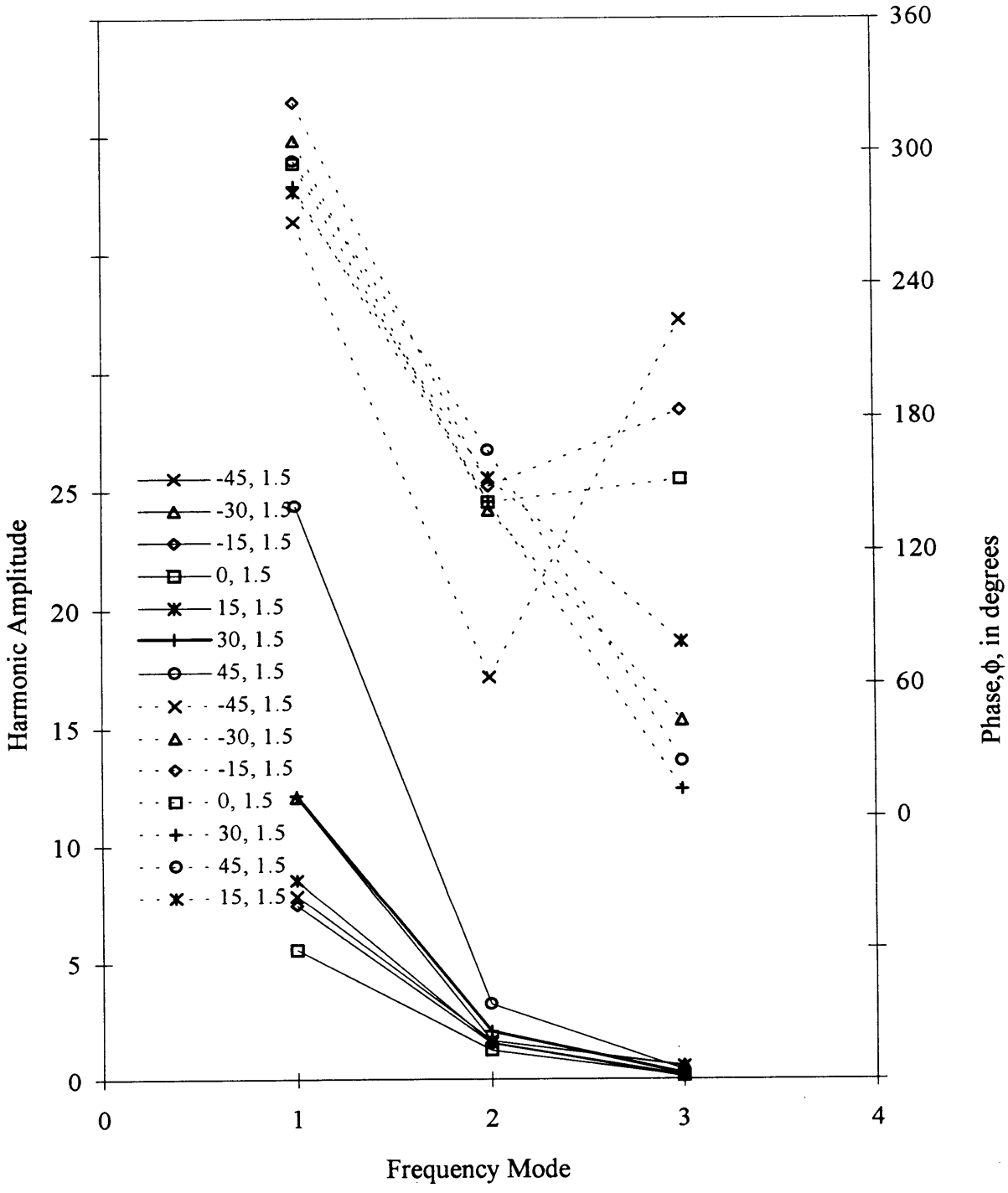

Figure 4.28: Amplitudes of Harmonics and Phase for the moment at 100% span with a non-dimensional jet velocity equal to 1.5 versus frequency mode.

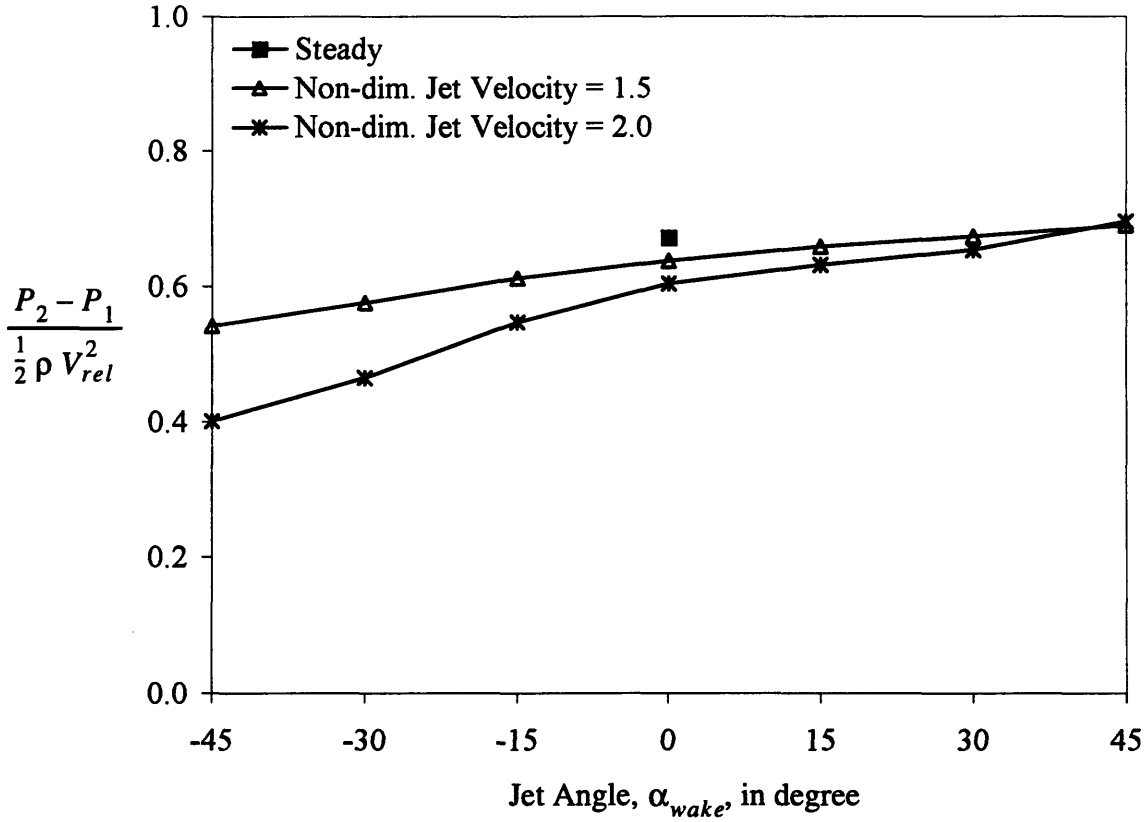

Figure 4.29: Pressure difference between exit and inlet at 88% span for non-dimensional jet velocity equal to 1.5 and 2.0 versus jet angle

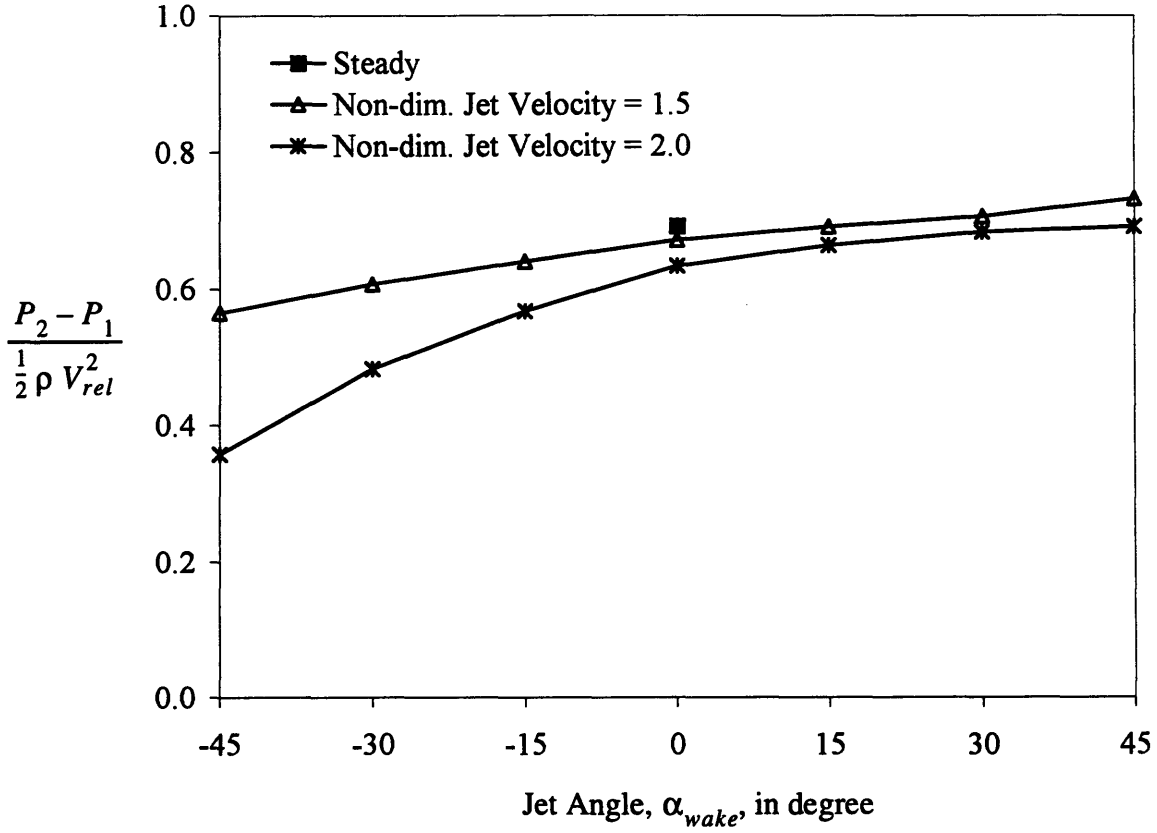

Figure 4.30: Pressure difference between exit and inlet at 100% span for non-dimensional jet velocity equal to 1.5 and 2.0 versus jet angle

Chapter 5

Conclusions and Recommendations

5.1 Summary and Conclusion

Axial forces, tangential forces, and moments were computed for a transonic rotor with jet velocities of 1.5 and 2.0 times the free-stream velocity, jet angles of ±45, ±30, ±15, and 0 degrees, and two radial positions (88% span and 100% span of NASA Rotor 35). For these cases, the reduced frequency was roughly 3. The specific findings are:

1. It is found that the unsteady axial forces are largest ($\frac{F_{max} - F_{min}}{1/2\,\rho\, V_{rel}\, V_x\, C} \sim 0.9$) at a jet angle of +45 degrees and minimum (~ 0.2) at a jet angle of zero degrees. The same trends are found for the unsteady tangential force, but the values of maximum and minimum are roughly 0.4 and 0.15, respectively. The unsteady moments have a maximum ($\frac{M_{max} - M_{min}}{1/2\,\rho\, V_{rel}\, V_x\, C^2} \sim 0.55$) at +45 degrees jet angle and minimum (~ 0.2) at zero degrees jet angle.

2. For a quasi-steady momentum analysis, the exit angle of an unsteady fluid flow needs to be known within a degree to calculate unsteady forces within 10%. A quasi-steady momentum analysis, where the exit angle is computed with a mixed compressible and incompressible iterative scheme, gives a good approximation of the unsteady forces and steady forces.

3. The first and second harmonic amplitudes of the unsteady forces and moments are sufficient for the structural dynamics. For the axial forces at radial positions of 88% span and 100% span, the difference between the first harmonic amplitude and the second harmonic amplitude is 86% whereas the difference between the first harmonic amplitude and the third harmonic amplitude is 99%.

4. For a jet velocity equal to 1.5 times the free-stream velocity and a jet angle of zero degrees, the time averaged pressure difference (difference between inlet pressure and exit pressure) is decreased by 3% from the steady solution. For a jet velocity of 2.0 times the free-stream velocity and a jet angle of zero degree, the time averaged pressure difference is decreased by 8% compared to the steady solution. The lowest pressure difference is at -45 degrees jet angle (reduction of 15% from zero degrees value) and the highest at +45 degrees jet angle (increase of 9% from zero degrees value).

Bibliography

[1] Berndt, R. G. "Actuation for Rotating Stall Control of High Speed Axial Compressors." *S.M. Thesis*, Massachusetts Institute of Technology, Department of Aeronautics and Astronautics, February 1995.

[2] Epstein, A. H., Ffowcs-Williams, J. E., and Greitzer, E. M. "Active Suppression of Compressor Instabilities." *Journal of Propulsion and Power* Vol. 5 (1989): 204-211.

[3] Paduano, J. D., Greitzer, E. M., Epstein, A. H., Guenette, G. R., Gysling, D. L., Haynes, J., Hendricks, G. J., Simon, J. S., and Valavani, L. "Smart Engines: Concept and Application", *Integrated Computer-Aided Engineering*. New York: Wiley, 1993. 3-28.

[4] AGARD Conference Proceedings No. 177 "Unsteady phenomena in turbomachinery." *46th Propulsion and Energetics Panel Meeting*, September 22-26, 1075. Published April 1976.

[5] Mikolajczak, A. A. "The Practical Importance of Unsteady Flow."AGRAD Conference Proceedings No. 177, *46th Propulsion and Energetics Panel Meeting*, September 22-26, 1975. Published April 1976.

[6] Reid, L., Moor, R. D. "Performance of Single-Stage Axial-Flow Transonic Compressor with Rotor and Stator Aspect Ratios of 1.19 and 1.26, Respectively, and with Design Pressure Ratio of 1.82." *NASA Technical Paper 1338*. 1978.

[7] Giles, M. B. "UNSFLO: A Numerical Method for the Calculation of Unsteady Flow in Turbomachinery." *GTL Report No. 205*, Massachusetts Institute of Technology, Department of Aeronautics and Astronautics, March 1991.

[8] Giles, M. B., Haimes, R. "UNSFLO User's Manual." Massachusetts Institute of Technology, Department of Aeronautics and Astronautics, Version 6.0, March 1995.

[9] Giles, M. B., Haimes, R. "UNSFLO Test Suite." Massachusetts Institute of Technology, Department of Aeronautics and Astronautics, Version 6.0, March 1991.

[10] Giles, M. B. "Calculation of Unsteady Wake Rotor Interaction." *AIAA Journal of Propulsion and Power*, 4(4):356-362, July/August 1988.

[11] Giles, M. B. "Non-Reflecting Boundary Conditions for Euler Equation Calculations." *AIAA Journal*, 28(12), December 1990.

[12] Ni, R. H. "A Multiple Grid Scheme for Solving the Euler Equations." *AIAA Journal*, 20(11):1565-1571, November 1981.

[13] Beam, R., Warming, R. "An Implicit Factored Scheme for the Compressible Navier-Stokes Equations." *AIAA Journal*, 16:393-403, June 1978.

[14] Roe, P. "Characteristic-Bases Scheme for the Euler Equations." *Annual Review of Fluid Mechanics*, 18:337-365, 1986.

[15] Dannenhoffer, J. F. "GRAFIC Version 3." Massachusetts Institute of Technology, Department of Aeronautics and Astronautics, 1989.

[16] Lindquist, D. R., Giles, M. B. "Generation and use of Unstructured Grids for Turbomachinery. *Proceedings of Computational Fluid Dynamics Symposium on Aeropropulsion*, NASA CP-10045, April 1990.

[17] Shapiro, A. H. "The Dynamics and Thermodynamics of Compressible Fluid Flow." New York: John Wiley & Sones, 1953.

[18] Anderson, J. D. "Fundamentals of Aerodynamics." New York: McGraw-Hill, Inc., 1991.

[19] Anderson, D. A., Tannehill, J. C., Pletcher, R. H. "Computational Fluid Dynamics and Heat Transfer." Hemisphere Publishing Corporation, 1984.

[20] Hirsch C. "Numerical Computation of Internal and External Flows" New York: John Wiley & Sones, 1988.

[21] Kreyszig, E. "Advanced Engineering Mathematics." 7th ed., John Wiley, New York, 1993.

[22] Hill, P., G., Peterson, C., R. "Mechanics and Thermodynamics of Propulsion." 2nd ed., Addison-Wesley, Massachusetts, 1992.

[23] Meirovitch, L. "Elements of Vibration Analysis."2nd ed., McGraw Hill, New York, 1986.

Appendix A

The Governing Equations

The purpose of this appendix is to summarize the inviscid and viscous compressible flow equations in the Eulerian and Lagrangian formulation and to stress the assumptions that lead to these equations. For a formal and detailed derivation of the equations refer to Shapiro [17] or Anderson [18], and for a detailed presentation of the numerical methods for the solution of these equation refer to Anderson, Tannehill, and Pletcher [19] or Hirsch [20].

A.1 Conservation Laws

Three conservation laws form the basis of the fluid dynamic equations. These three laws are the conservation of mass, conservation of momentum, and conservation of energy. Applying these laws to fluid in motion leads to the equation of fluid dynamics or equation of motion. In general there are two approaches that can be used to derive the equations of motion: the phenomenological approach, which is detailed in Shapiro [17], and the kinematic-theory approach, which is detailed in Anderson [18]. These two approaches derive the same fluid dynamic equations if equivalent assumptions are made in both approaches. The following subsections use the assumptions of uniform and homogeneous fluid without chemical reactions and give the resulting equations of motions.

A.1.1 Conservation of Mass

The physical principle of conservation of mass is: "Mass can be neither created nor destroyed." Applying this physical principle of conservation of mass to a finite control volume fixed in space gives the conservation of mass written as

$$\frac{\partial}{\partial t}\iiint_{V} \rho \, dV + \iint_{A} \rho \, \mathbf{V} \bullet \mathbf{dA} = 0. \tag{A.1}$$

Equation (A.1) expresses the continuity equation in integral form applied on a finite space. The advantage of this form is that aerodynamic phenomena over finite region of space can be related without being concerned about the details of precisely what is happening at a given distinct point in the fluid flow. This form will be used in Appendix C when a quasi-steady momentum analysis is performed on a finite control volume.

However, when a CFD analysis of a fluid flow is required, an equation that relates flow properties at a given point is needed. In that case, the integral form as expressed in Equation (A.1) is not practical and can be transformed into another form which does relate flow properties at a given point. Since the control volume that was used to obtain Equation (A.1) is fixed in space, the limits of integration are also fixed, and hence, the time derivative can be placed inside the integration. Now, applying the divergence theorem to the second term on the left hand side and rearranging the terms, Equation (A.1) becomes

$$\frac{\partial \rho}{\partial t} + \nabla \bullet (\rho \mathbf{V}) = 0. \tag{A.2}$$

Equation (A.2) is now the continuity equation in the form of a partial differential equation and relate the flow field variables at a point in the flow, as opposed to Equation (A.1), which deals with a finite space.

Note that in the derivation of the two equations above, the only assumption about the nature of the fluid is that it is a continuum. Therefore, Equation (A.1) and (A.2) hold in general for the three-dimensional and unsteady flow of any type of fluid, inviscid or viscous, compressible or incompressible.

A.1.2 Conservation of Momentum

The physical principle of conservation of mass is: "Force is equal to time rate of change of momentum." Applying the physical principle of conservation of momentum to a finite control volume fixed in space gives the conservation of mass, written as

$$\frac{\partial}{\partial t}\iiint_V \rho \mathbf{V}\, dV + \oiint_A \rho \mathbf{V}\, \mathbf{V}\bullet \mathbf{dA} = -\mathbf{F} - \oiint_A p\, \mathbf{dA} + \iiint_V \rho \mathbf{f}\, dV + \mathbf{F}_{\text{viscous}}, \qquad \text{(A.3)}$$

where **f** represents a vector of the net body forces per unit mass exerted on the fluid inside a finite control volume V. **F** denotes a vector of the forces exerted by the body on the fluid and $\mathbf{F}_{viscous}$ denotes a vector of the total viscous forces exerted on the control surface. The elemental surface force due to pressure acting on the element of area **dA** is $-p\mathbf{dA}$ where the negative sign indicates that the force is in the direction opposite of **dA**.

Equation (A.3) expresses the momentum equation in integral form applied on a finite space and is a vector equation. The advantage of this form, just as for the continuity equation, is that aerodynamic phenomena over finite region of space can be related without being concerned about the details of precisely what is happening at a given distinct point in the fluid flow. This form will also be used in Appendix C when a quasi-steady momentum analysis is performed on a finite control volume.

However, when we perform a CFD analysis of a fluid flow, as mentioned for the continuity equation, another vector equation is needed that relate flow properties at a given point. In that case, the integral form as expressed in Equation (A.3) is not practical and can be transformed into another form which does relate fluid flow properties at a given point. Equation (A.3) is a vector equation and can be written as three scalar equations. Also, since the control volume that was used to obtain Equation (A.3) is fixed in space, the limits of integration are also fixed, and hence, the time derivative can be placed inside the integration. Now, applying the gradient theorem to the first term on the right hand side, the divergence theorem to the second term on the left hand side, and after rearranging the terms, Equation (A.3) becomes

$$\begin{aligned}
\frac{\partial \rho u}{\partial t} + \nabla\bullet(\rho u\mathbf{V}) &= -\frac{\partial p}{\partial x} + \rho f_x + (F_x)_{\text{viscous}} \\
\frac{\partial \rho v}{\partial t} + \nabla\bullet(\rho v\mathbf{V}) &= -\frac{\partial p}{\partial y} + \rho f_y + (F_y)_{\text{viscous}} \\
\frac{\partial \rho w}{\partial t} + \nabla\bullet(\rho w\mathbf{V}) &= -\frac{\partial p}{\partial z} + \rho f_z + (F_z)_{\text{viscous}}
\end{aligned} \quad , \tag{A.4}$$

where the subscripts x, y, and z on $F_{viscous}$ denote the spatial components of the viscous shear stresses. Expressing the viscous forces explicitly in terms of the appropriate flow-field variables, Equation (A.4) becomes now

$$\begin{aligned}
\frac{\partial \rho u}{\partial t} + \nabla\bullet(\rho u\mathbf{V}) &= -\frac{\partial p}{\partial x} + \rho f_x + \frac{\partial \tau_{xx}}{\partial x} + \frac{\partial \tau_{yx}}{\partial y} + \frac{\partial \tau_{zx}}{\partial z} \\
\frac{\partial \rho v}{\partial t} + \nabla\bullet(\rho v\mathbf{V}) &= -\frac{\partial p}{\partial y} + \rho f_y + \frac{\partial \tau_{xy}}{\partial x} + \frac{\partial \tau_{yy}}{\partial y} + \frac{\partial \tau_{zy}}{\partial z} \\
\frac{\partial \rho w}{\partial t} + \nabla\bullet(\rho w\mathbf{V}) &= -\frac{\partial p}{\partial z} + \rho f_z + \frac{\partial \tau_{xz}}{\partial x} + \frac{\partial \tau_{yz}}{\partial y} + \frac{\partial \tau_{zz}}{\partial z}
\end{aligned} \quad . \tag{A.5}$$

Equation (A.4) gives now the x, y, and z component of the momentum equation in the form of a partial differential equation and relates the flow field variables at a point in the flow, as opposed to Equation (A.3), which deals with a finite space. These equations are scalar equations and are called the **Navier-Stokes** equations. The stress components τ_{ij} are related to the dynamic viscosity coefficient μ and the bulk viscosity coefficient $\lambda = -(2/3)\,\mu$ by the equations:

$$\begin{aligned}
\tau_{xx} &= \lambda(\nabla\bullet\mathbf{V}) + 2\mu\frac{\partial u}{\partial x} \\
\tau_{yy} &= \lambda(\nabla\bullet\mathbf{V}) + 2\mu\frac{\partial v}{\partial y} \\
\tau_{zz} &= \lambda(\nabla\bullet\mathbf{V}) + 2\mu\frac{\partial w}{\partial z} \\
\tau_{xy} &= \tau_{yx} = \mu\left(\frac{\partial v}{\partial x} + \frac{\partial u}{\partial y}\right) \\
\tau_{yz} &= \tau_{zy} = \mu\left(\frac{\partial w}{\partial y} + \frac{\partial v}{\partial z}\right) \\
\tau_{zx} &= \tau_{xz} = \mu\left(\frac{\partial u}{\partial z} + \frac{\partial w}{\partial x}\right)
\end{aligned} \tag{A.6}$$

Note that in the derivation of Equation (A.3) and (A.5) the only assumption about the nature of the fluid is that it is a continuum. Therefore, Equation (A.3) and (A.5) hold in general for the three-dimensional and unsteady flow of any type of fluid, inviscid or viscous, compressible or incompressible.

A.1.3 Conservation of Energy

The physical principle of conservation of energy is: "Energy can be neither created nor destroyed; it can only be changed in form." Applying the physical principle of conservation of energy to a finite control volume fixed in space gives the conservation of energy written as

$$\begin{aligned} &\iiint_V \dot{q}\rho dV + \dot{Q}_{viscous} - \oiint_A p\mathbf{V}\bullet\mathbf{dA} + \iiint_V \rho\,(\mathbf{f}\bullet\mathbf{V})\,dV + \dot{W}_{viscous} \\ &= \frac{\partial}{\partial t}\iiint_V \rho\left(e+\frac{V^2}{2}\right)dV + \oiint_A \rho\left(e+\frac{V^2}{2}\right)\mathbf{V}\bullet\mathbf{dA} \end{aligned} \quad , \qquad (A.7)$$

where $\dot{q}$ represents the volumetric rate of heat addition per unit mass, $\dot{Q}_{viscous}$ denotes the rate of heat addition to the control volume due to viscous effects, **f** is the net body forces per unit mass exerted on the fluid inside a finite control volume V, *e is* the internal energy, and $\dot{W}_{viscous}$ denotes the shear stresses on the control surface. To complete Equation (A.7), the rate of work delivered by a shaft can be added to the left side, and if the change in height is important, the potential energy per unit mass can be added to the total energy.

Equation (A.7) expresses the energy equation in integral form applied on a finite space and is a scalar equation. This equation is essentially the first law of thermodynamics. The advantage of this form, just as for the continuity equation and the momentum equation, is that aerodynamic phenomena over finite region of space can be related without being concerned about the details of precisely what is happening at a given distinct point in the fluid flow. This form will be used in Appendix C when a quasi steady analysis is performed on a finite control volume.

However, when we perform a CFD analysis of a fluid flow, as mentioned for the continuity equation and for the momentum equation, another equation is needed that relate flow prop-

erties at a given point. In this case, the integral form as expressed in Equation (A.7) can be transformed into another form which does relate flow properties at a given point by applying the divergence theorem to the surface integrals, collecting all terms inside the same volume integrals, and setting the integrand equal to zero. After rearranging the terms, Equation (A.7) becomes

$$\begin{aligned} &\frac{\partial}{\partial t}\left[\rho\left(e+\frac{V^2}{2}\right)\right]+\nabla\bullet\left[\rho\left(e+\frac{V^2}{2}\right)\mathbf{V}\right] \\ &=\rho\dot{q}-\nabla\bullet(p\mathbf{V})+\rho(\mathbf{f}\bullet\mathbf{V})+\dot{Q}'_{viscous}+\dot{W}'_{viscous} \end{aligned} \quad , \tag{A.8}$$

where $\dot{Q}'_{viscous}$ and $\dot{W}'_{viscous}$ represent the proper forms of the viscous term.

A.2 Equation of State

Six unknowns *u, v, w, p,* ρ and *e* appear in a problem with unknown heat transfer and body forces. The conservation laws provide five equations. In order to obtain the closure of these equations, one more equation is needed. Therefore, the equation from the thermodynamic state of the fluid is added. Also, the static enthalpy per unit mass h and the total enthalpy per unit mass h_t are defined by

$$h = e+\frac{p}{\rho} \qquad h_t = \left(e+\frac{V^2}{2}\right)+\frac{p}{\rho}. \tag{A.9}$$

For a perfect gas the following thermodynamic relations can also be written

$$\begin{aligned} &de = c_v dT \qquad dh = c_p dT \\ &c_v = \frac{R}{\gamma-1} \\ &c_p = \frac{\gamma R}{\gamma-1} \end{aligned} \quad , \tag{A.10}$$

where R is the gas constant, γ is the ratio of specific heat, c_v is the specific heat capacity under constant volume, and c_p is the specific heat capacity under constant pressure.

In order to derive the equation of state, it is required that the internal energy be zero when the absolute temperature is zero which means that

$$e = c_v T. \tag{A.11}$$

Now the equation of state takes the form of

$$p = \rho RT \qquad \text{or} \qquad p = \rho(\gamma - 1)e. \tag{A.12}$$

Thus, the six equations that solve the problem are the equations of conservation of mass, Equation (A.1) or Equation (A.2), the three equations of conservation of momentum, Equation (A.3) or Equation (A.4), the equation of conservation of energy, Equation (A.7) or Equation (A.8), and the equation of state, Equation (A.12).

A.3 The Navier-Stokes Equations

The Navier-Stokes equations are the equations of conservation of momentum, given by Equation (A.5). However, in CFD it is customary to combine the conservation of mass, conservation of momentum, and conservation of energy to the equation of fluid dynamics, also referred to as the Navier-Stokes equations and written in matrix form as

$$\frac{\partial \mathbf{U}}{\partial t} + \frac{\partial \mathbf{F}}{\partial x} + \frac{\partial \mathbf{G}}{\partial y} + \frac{\partial \mathbf{E}}{\partial z} = \mathbf{0}, \tag{A.13}$$

where **U**, **F**, **G**, and **E** are five-component vectors given by

$$\mathbf{U} = \begin{bmatrix} \rho \\ \rho u \\ \rho v \\ \rho w \\ \rho e_t \end{bmatrix} \qquad \mathbf{F} = \begin{bmatrix} \rho u \\ \rho u^2 + p - \tau_{xx} \\ \rho uv - \tau_{xy} \\ \rho uw - \tau_{xz} \\ (\rho e_t + p)\, u - u\tau_{xx} - v\tau_{xy} - w\tau_{xz} + q_x \end{bmatrix}$$

$$\mathbf{G} = \begin{bmatrix} \rho v \\ \rho vu - \tau_{yz} \\ \rho v^2 + p - \tau_{yy} \\ \rho vw - \tau_{yz} \\ (\rho e_t + p)\, v - u\tau_{yx} - v\tau_{yy} - w\tau_{yz} + q_y \end{bmatrix} \qquad \text{(A.14)}$$

$$\mathbf{E} = \begin{bmatrix} \rho w \\ \rho uw - \tau_{zx} \\ \rho vw - \tau_{zy} \\ \rho w^2 + p - \tau_{zz} \\ (\rho e_t + p)\, w - u\tau_{zz} - v\tau_{zy} - w\tau_{zz} + q_z \end{bmatrix}$$

Closure is obtained by the equation of state, Equation (A.12). The two-dimensional form of the equations in x and y can be obtained from the above three-dimensional equations be deleting the vector **E**, the fourth row in the remaining vectors, and all the terms containing w, τ_{zz}, τ_{zx}, and τ_{zy}.

The Navier-Stokes equations are a mixed set of hyperbolic-parabolic equations in time. If the unsteady terms are dropped, then the equations become a mixed set of hyperbolic-elliptic equations, which are much harder to solve. Thus, in most cases the unsteady form of the equations is used even for steady flow computations, and the solution is obtained by marching the solution in time until convergence is reached.

A.4 The Euler Equations

The Euler equations are also derived from the conservation of mass, conservation of momentum, and conservation of energy equations but with the assumption that the fluid is inviscid. These equations are now obtained from the Navier-Stokes equations, Equation (A.13) and (A.14), by deleting all the viscous and also the heat transfer terms, which are of the same magnitude. It is also customary to write the system of equations in matrix form:

$$\frac{\partial \mathbf{U}_E}{\partial t} + \frac{\partial \mathbf{F}_E}{\partial x} + \frac{\partial \mathbf{G}_E}{\partial y} + \frac{\partial \mathbf{E}_E}{\partial y} = \mathbf{0}, \tag{A.15}$$

where $\mathbf{U}_E$, $\mathbf{F}_E$, $\mathbf{G}_E$, and $\mathbf{E}_E$ are five-component vectors given by

$$\mathbf{U}_E = \begin{bmatrix} \rho \\ \rho u \\ \rho v \\ \rho w \\ \rho e_t \end{bmatrix} \qquad \mathbf{F}_E = \begin{bmatrix} \rho u \\ \rho u^2 + p \\ \rho uv \\ \rho uw \\ (\rho e_t + p)\, u \end{bmatrix} \tag{A.16}$$

$$\mathbf{G}_E = \begin{bmatrix} \rho v \\ \rho vu \\ \rho v^2 + p \\ \rho vw \\ (\rho e_t + p)\, v \end{bmatrix} \qquad \mathbf{E}_E = \begin{bmatrix} \rho w \\ \rho uw \\ \rho vw \\ \rho w^2 + p \\ (\rho e_t + p)\, w \end{bmatrix}$$

Closure is obtained by the equation of state, Equation (A.12). The two-dimensional form of the equations in x and y can be obtained from the above three-dimensional equations by deleting the vector $\mathbf{E}_E$ and the fourth row in the remaining vectors.

The Euler equations are a set of hyperbolic equations in time. If the unsteady terms are dropped, the equations become elliptic for subsonic flow and hyperbolic for supersonic flow.

A.5 The Solution of Fluid Dynamic Equations

The Navier-Stokes equations and the Euler equations do not have analytical solutions for most of engineering interest. The solutions of the above equations, or other equations derived from the above equations with various assumptions, are solved on a computational grid around the geometry of interest with the appropriate boundary conditions.

The field of CFD is progressing rapidly. In the past few years considerable advances have been made in methods for finding a solution for the Navier-Stokes equations and Euler equations. These methods employ finite-difference, finite-volume, finite-element, and spectral methods. However, the large majority of these methods deal with a steady flow field with time-marching to convergence. This means that although the unsteady and therefore time-dependent equations are used, the boundary conditions that are applied are for steady flow, and the solution converges to the steady flow solution.

Four problems appear in the implementation of numerical methods for the solution of unsteady flows in turbomachinery. The first problem, which also appears in steady flows and is the easiest to deal with, is the arrangement of the computational grid so that periodic conditions are applied to simulate the passages between blades in one cascade. The second problem is to find the correct boundary conditions at the inlet boundary and at the outlet boundary of the computational flow field. The third problem appears in the modelling of time-averaged periodically unsteady flows such as the shedding of the wakes from upstream blade rows. The spatial and temporal periods of these sources of unsteadiness are for general geometries different from the periodicity imposed for successive blades in one blade row. The fourth problem is the modelling of the random and chaotic unsteadiness due to the turbulent nature of the boundary layers. This problem is too complex for current computational methods and computer capabilities, but some attempts at modelling simple geometries have appeared.

Appendix B

Computation with UNSFLO

This appendix presents the non-dimensional analysis used in UNSFLO, the input variable needed for the computations, the file structure used in UNSFLO, and the programs needed to obtain the final plot of forces and moments used in the research. Therefore, the first section summarizes the reference quantities that are needed for the non-dimensional analysis, the dependent variables, and the second section gives the procedure for running UNSFLO with its file structure and program structure.

B.1 Non-Dimensional Analysis of the Equations

The reference quantities that are needed in the computer program UNSFLO for the non-dimensional analysis to solve the equation of fluid dynamics are given in Table B.1.

Reference Quantities		Defined as
L_{ref}	reference length	(left to the user)
u_{ref}	reference velocity	inlet relative stagnation speed of sound
ρ_{ref}	reference density	inlet relative stagnation density
p_{ref}	reference pressure	inlet relative stagnation pressure

Table B.1: Reference quantities needed to non-dimension the dependent variables

Reference Quantities		Defined as
$RE = \frac{\rho_{ref}\mu_{ref}L_{ref}}{\mu_{ref}}$	Reynolds number	reference quantities
μ_{ref}	reference viscosity	temperature that is nondimensioned by the inlet relative stagnation temperature
$\text{Period} = \frac{u_{ref}}{L_{ref}} \times \text{dim.period}$	period of oscillation	

Table B.1: Reference quantities needed to non-dimension the dependent variables

B.2 Flow of Data between Programs and Data Files

Table B.2 shows the flow of input and output data between the programs in the UNSFLO suite and their corresponding data files that were required for purpose of this study. Figure B.1 shows schematically the necessary input files and the sequence of the programs which must be executed to calculate an unsteady wake/rotor interaction.

Programs	Input		Output		Run by Typing
GRDINI	blade.xxx		grid.xxx		grdini p1 p2
UNSFLO	grid.xxx	input.yyy	flow.yyy (for steady)		unsflo p2 p3
HSTPLT	hist.yyy				hstplt yyy
FLOPLT	grid.xxx	flow.yyy			floplt p2 p3
FGMULT	grid.xxx	flow.xxx	grid.www	flow.zzz	fgmult p2 p3 p4 p5
UNSFLO	grid.www	flow.zzz	flou.zzz (for unsteady)		unsflo p4 p5
UNSFFT	grid.www	flou.zzz	four.zzz		unsfft p4 p5
UNSIFT	grid.www	four.zzz	flou.zzz		unsift p4 p5
UNSPLT	grid.www	flou.zzz			unsplt p4 p5

Table B.2: Programs in UNSFLO and the data files corresponding to the programs

- GRDINI is the grid initialization program which calculates the grid coordinates from the blade geometry.
- UNSFLO is the main program which calculates the steady or unsteady flow field for the grid coordinates and the input data.
- HSTPLT is a plotting program that displays the iteration history.
- FLOPLT is a plotting program which displays the steady flow field.
- FGMULT creates a multi-passage grid and a multi-passage flow field from a single-passage grid and flow field.
- UNSFFT calculates the Fourier transform of the unsteady flow field at each grid node.
- UNSIFT calculates the inverse Fourier transform which is the opposite to UNSFFT.
- UNSPLT is the plotting program which displays the unsteady flow field and the time-integrated quantities.

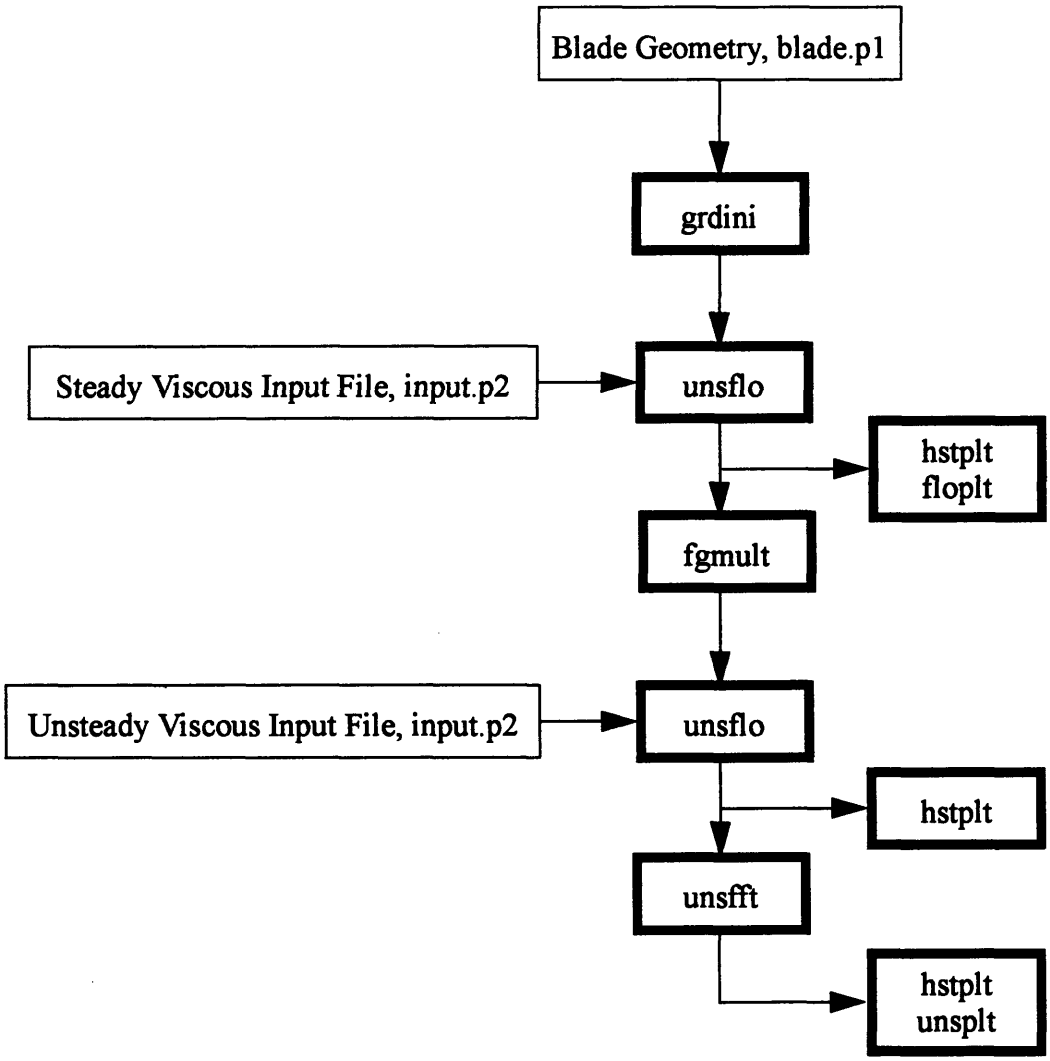

Figure B.1: Computational procedure and programs for the computer program UNSFLO

Appendix C

Detailed Derivation of Quasi-Steady Momentum Analysis

The purpose of this section is to give a detailed derivation including all the assumptions used to obtain the final equations that are used for the quasi-steady momentum analysis. The iterative procedure to solve these final equations is given in Section 3.2: Equation and Solution Procedure for Quasi-Steady Momentum Analysis.

Assuming that the **conservation of mass**, **conservation of momentum**, and **conservation of energy** holds, that the nature of the fluid is a **continuum**, that **no work is delivered through a shaft**, and the size of the control volume is small so that the **height is not important**, then Equation (A.1), Equation (A.3), and Equation (A.7) are obtained and are rewritten here once more.

$$\frac{\partial}{\partial t}\iiint_V \rho \, dV + \iint_A \rho \, \mathbf{V} \bullet \mathbf{dA} = 0 \tag{C.1}$$

$$\frac{\partial}{\partial t}\iiint_V \rho \mathbf{V} \, dV + \iint_A \rho \mathbf{V} \, \mathbf{V} \bullet \mathbf{dA} = -\mathbf{F} - \iint_A p \, \mathbf{dA} + \iiint_V \rho \mathbf{f} \, dV + \mathbf{F}_{viscous} \tag{C.2}$$

$$\iiint_V \dot{q}\rho dV + \dot{Q}_{viscous} - \iint_A p\mathbf{V}\bullet\mathbf{dA} + \iiint_V \rho\,(\mathbf{f}\bullet\mathbf{V})\,dV + \dot{W}_{viscous}$$
$$= \frac{\partial}{\partial t}\iiint_V \rho\left(e+\frac{V^2}{2}\right)dV + \iint_A \rho\left(e+\frac{V^2}{2}\right)\mathbf{V}\bullet\mathbf{dA} \tag{C.3}$$

Assuming that the flow is **steady**, so that the flow variables are a function of spatial location only, Equation (C.1) through (C.3) reduce to

$$\iint_A \rho\,\mathbf{V}\bullet\mathbf{dA} = 0, \tag{C.4}$$

$$\iint_A \rho\mathbf{V}\,\mathbf{V}\bullet\mathbf{dA} = -\mathbf{F} - \iint_A p\,\mathbf{dA} + \iiint_V \rho\mathbf{f}\,dV + \mathbf{F}_{\text{viscous}}, \tag{C.5}$$

$$\iiint_V \dot{q}\rho dV + \dot{Q}_{viscous} - \iint_A p\mathbf{V}\bullet\mathbf{dA} + \iiint_V \rho\,(\mathbf{f}\bullet\mathbf{V})\,dV + \dot{W}_{viscous}$$
$$= \iint_A \rho\left(e+\frac{V^2}{2}\right)\mathbf{V}\bullet\mathbf{dA} \tag{C.6}$$

Furthermore, assuming that the **body forces and surface forces except pressure forces are zero**, and that all the **viscous effects**, $_{viscous}$, **can be neglected**, then Equation (C.5) and (C.6) can be reduced to

$$\iint_A \rho\mathbf{V}\,\mathbf{V}\bullet\mathbf{dA} = -\mathbf{F} - \iint_A p\,\mathbf{dA}, \tag{C.7}$$

$$\iiint_V \dot{q}\rho dV - \iint_A p\mathbf{V}\bullet\mathbf{dA} = \iint_A \rho\left(e+\frac{V^2}{2}\right)\mathbf{V}\bullet\mathbf{dA}. \tag{C.8}$$

The energy equation (C.8) contains a rate of volumetric heating, and by assuming that there is **no heat addition**, $\dot{q} = 0$, Equation (C.8) can be reduced to

$$-\oiint_A p\mathbf{V}\bullet\mathbf{dA} = \oiint_A \rho\left(e+\frac{V^2}{2}\right)\mathbf{V}\bullet\mathbf{dA}. \tag{C.9}$$

When now the **flow is only allowed to cross the inlet and exit** of the rotor cascade and that the **density, velocity, and pressure are uniform across the inlet and exit**, the remaining of the continuity equation, Equation (C.4), the momentum equation, Equation (C.7), and the energy equation, Equation (C.9), reduce further to

$$A_2\cdot\rho_2\cdot V_{rel,2}\cdot\cos\beta_2 - A_1\cdot\rho_1\cdot V_{rel,1}\cdot\cos\beta_1 = 0, \tag{C.10}$$

$$\begin{aligned} F_x &= A_2\cdot[p_2+\rho_2\cdot(V_{rel,2}\cdot\cos\beta_2)^2] - A_1\cdot[p_1+\rho_1\cdot(V_{rel,1}\cdot\cos\beta_1)^2] \\ F_y &= A_2\cdot\rho_2\cdot V_{rel,2}^2\cdot\cos\beta_2\cdot\sin\beta_2 - A_1\cdot\rho_1\cdot V_{rel,1}^2\cdot\cos\beta_1\cdot\sin\beta_1 \end{aligned}, \tag{C.11}$$

$$\begin{aligned} &p_2\cdot V_{rel,2}\cdot\cos\beta_2 + \rho_2\cdot\left(e+\frac{V_{rel,2}^2}{2}\right)\cdot V_{rel,2}\cdot\cos\beta_2 \\ &= -p_1\cdot V_{rel,1}\cdot\cos\beta_1 + \rho_1\cdot\left(e+\frac{V_{rel,1}^2}{2}\right)\cdot V_{rel,1}\cdot\cos\beta_1 \end{aligned}, \tag{C.12}$$

where the cosine and sine of relative inlet and relative exit angles, β_1 and β_2, appear from the evaluation of the dot product of two vectors. F_x and F_y are the axial and tangential forces, respectively, $V_{rel,1}$ and $V_{rel,2}$ are the relative velocities for inlet and exit, respectively, and p_1 and p_2 are the static pressures at the inlet and exit, respectively. Also, in the previous equations it is assumed a **2-dimensional flow**.

The continuity equation, momentum equations, and energy equation give four equations which involve five dependent variables: ρ, p, V_{rel}, β, and e. A fifth equation can be obtained from a thermodynamic state relation for e. Therefore, it needs to be assumed that the temperatures are moderate (for air T < 1000K), so that the specific heats are reasonable constant which implies a **calorically perfect gas**; therefore,

$$e = c_v T, \tag{C.13}$$

where c_v is the specific heat capacity under constant volume as stated earlier. Equation (C.13), however, introduces temperature as yet another dependent variable, but the system can be

completed by using the **perfect gas equation of state**

$$p = \rho RT \tag{C.14}$$

where R is the gas constant as stated earlier. With the above two equations, Equation (C.12) can be simplified even more to

$$\rho_2 \cdot V_{rel,2} \cdot \cos\beta_2 \cdot \left(\frac{p_2}{\rho_2} \frac{\gamma}{\gamma - 1} + \frac{V_{rel,2}^2}{2} \right) = \rho_1 \cdot V_{rel,1} \cdot \cos\beta_1 \cdot \left(\frac{p_1}{\rho_1} \frac{\gamma}{\gamma - 1} + \frac{V_{rel,1}^2}{2} \right). \tag{C.15}$$

All four equations that were obtained from the above derivation, namely, the continuity equation, Equation (C.10), the momentum equations in x and y direction, Equation (C.11), the energy equation, Equation (C.15), which also include the equation of state, Equation (C.14), have 12 variables, $A_1, p_1, \rho_1, V_{rel,1}, \beta_1$, from the flow into the control volume at station 1, A_2, $p_2, \rho_2, V_{rel,2}, \beta_2$, from the flow out of the control volume at station 2, and the axial force, F_x, and tangential force, F_y. When the flow into the control volume is now prescribed, the 12 variables reduce to seven unknowns which are the variables from the exit flow of the control volume and the two forces.

For the derivation of the energy equation, Equation (C.15), we assumed that the flow is adiabatic, a process in which no heat is added or taken away. If we assume further that the flow is also reversible, a process in which no frictional or other dissipative effects occur, then the combination of adiabatic process and reversible process gives another equation which combines thermodynamics and compressible aerodynamics, namely, that of an **isentropic flow**. With this isentropic flow assumption the following equation can be written:

$$\frac{p_2}{p_1} = \left(\frac{\rho_2}{\rho_1} \right)^{\gamma} \tag{C.16}$$

where the pressure is directly related to density through the isentropic process. Now, to evaluate the fluid flow, five equations exist but there are still seven unknowns.

The inlet area, A_1, and the exit area, A_2, of the rotor cascade are parameters that are given by the geometry of the NASA Rotor 35 and which were presented in Section 2.3.1: Airfoil Geometry. Therefore, five equations for six unknowns are left, and one more variable from the unknowns need to be prescribed. This variable from the set of unknowns is the exit angle,

β_2, which means that the relative exit angle has to be known before the forces of the fluid flow can be calculated. For a description in how this exit angle is chosen refer to Section 3.2: Equation and Solution Procedure for Quasi-Steady Momentum Analysis. Now, there are as many equations as there are unknowns, and the fluid flow can be solved.

Appendix D

Computed Results from UNSFLO

This appendix presents the results of the unsteady forces, in the x and y direction, and unsteady moment, in the z direction, computed and exported from UNSFLO for each of the radial positions, 88% span and 100% span. The unsteady forces of these figures are non-dimensioned with the density, ρ, the square of wheel speed , $(r\Omega)^2$, and the aerodynamic cord, C. The unsteady moments of these figures are non-dimensioned with the density, ρ, the square of relative inflow velocity, $(r\Omega)^2$, and the square of aerodynamic cord, C^2. These results are discussed in Chapter 4: Results and Discussion.

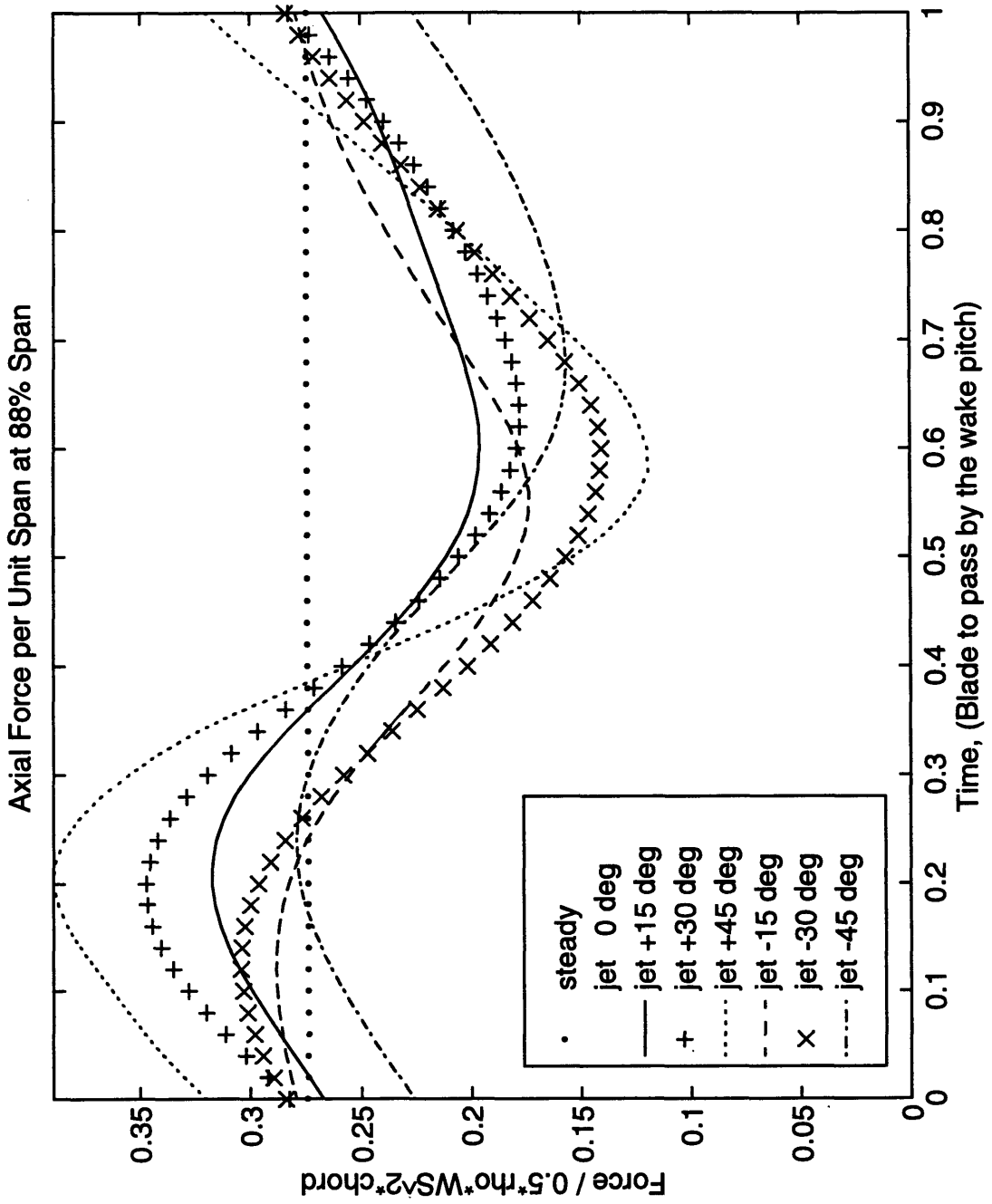

Figure D.1: Axial force at a radial position of 88% span and a jet velocity equal to 1.5 times the free-stream velocity

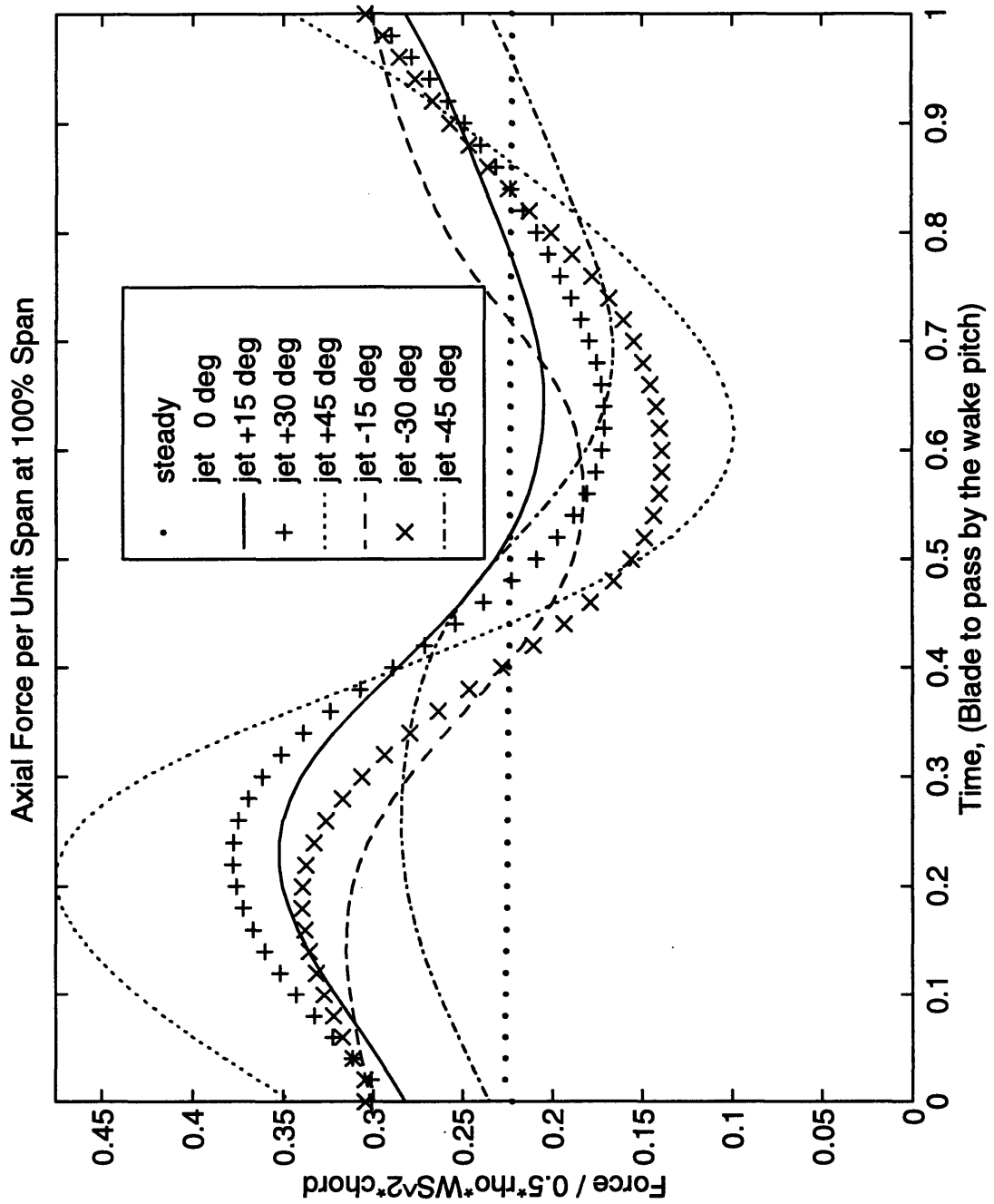

Figure D.2: Axial force at a radial position of 100% span and a jet velocity equal to 1.5 times the free-stream velocity

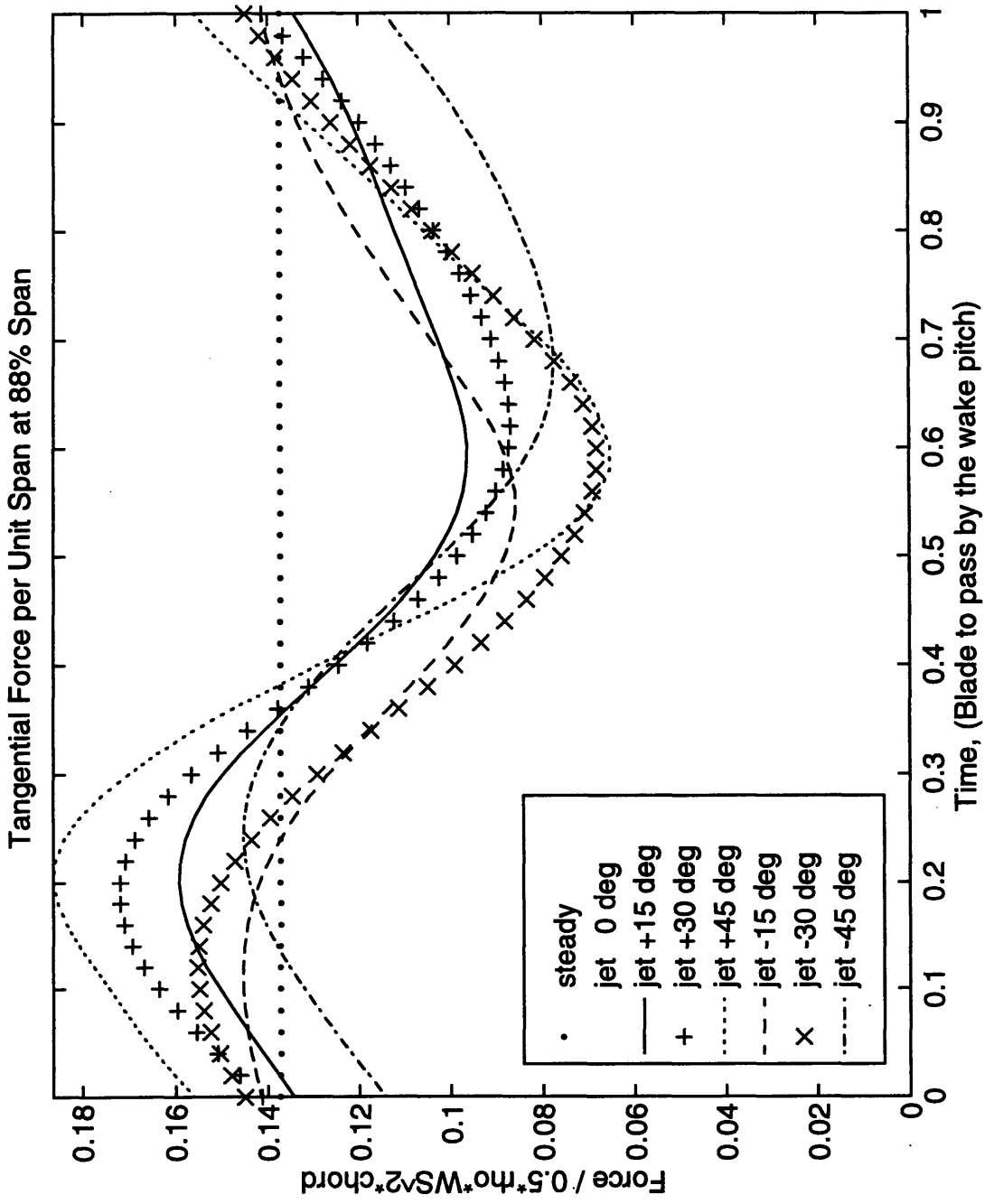

Figure D.3: Tangential force at a radial position of 88% span and a jet velocity equal to 1.5 times the free-stream velocity

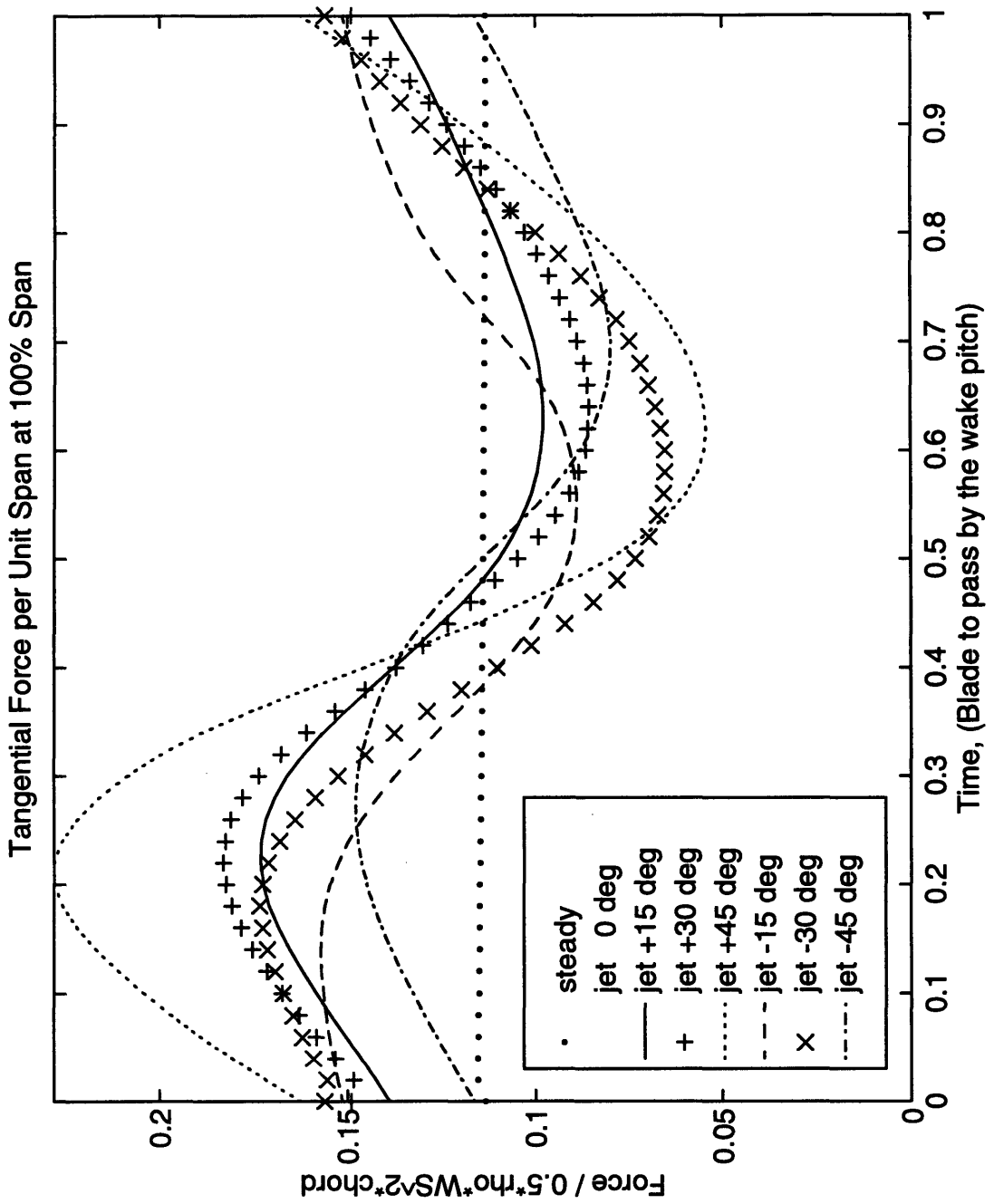

Figure D.4: Tangential force a radial position of 100% span and a jet velocity equal to 1.5 times the free-stream velocity

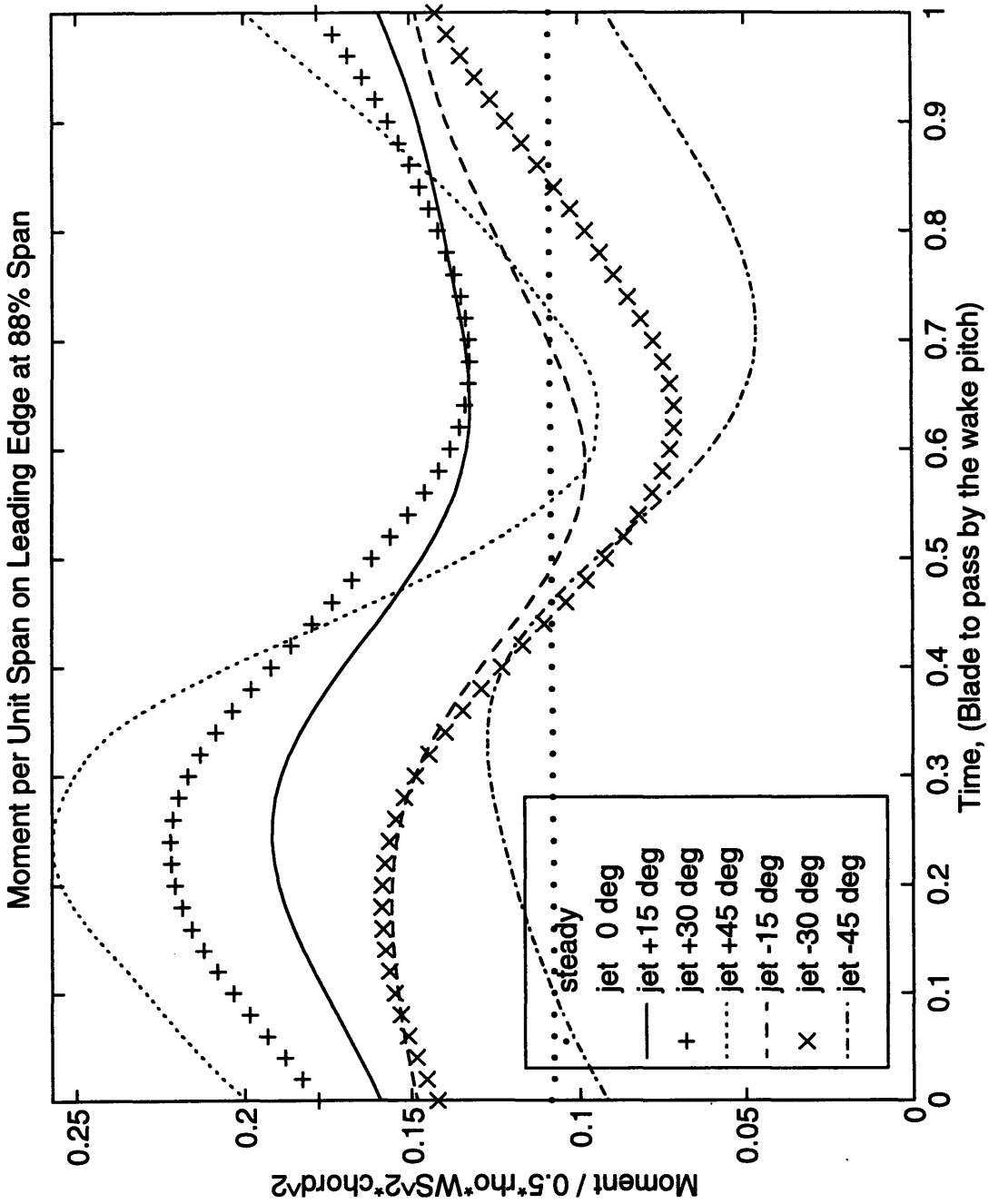

Figure D.5: Moment at a radial position of 88% span and a jet velocity equal to 1.5 times the free-stream velocity

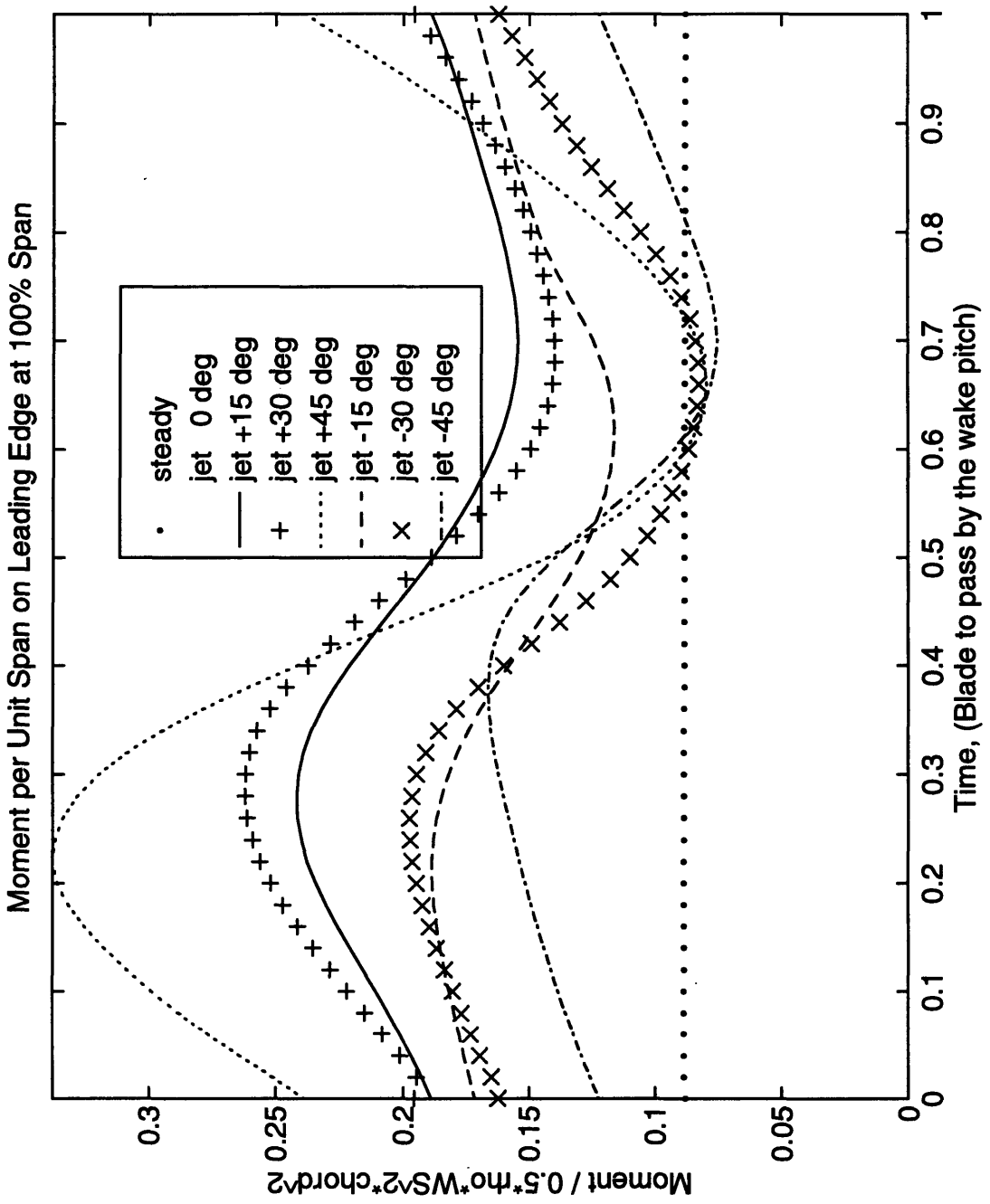

Figure D.6: Moment at a radial position of 100% span and a jet velocity equal to 1.5 times the free-stream velocity

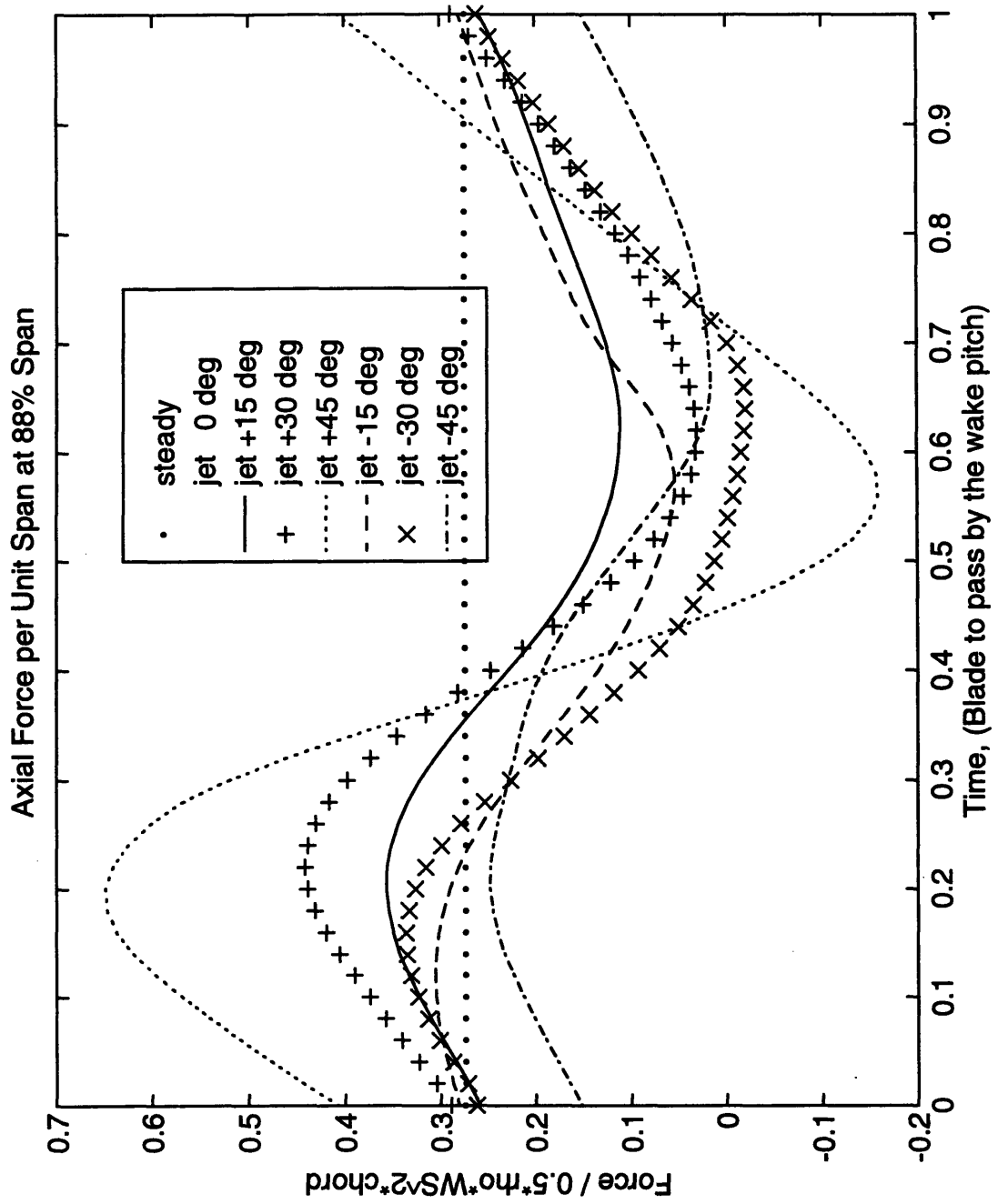

Figure D.7: Axial Force at a radial position of 88% span and a jet velocity equal to 2 times the free-stream velocity

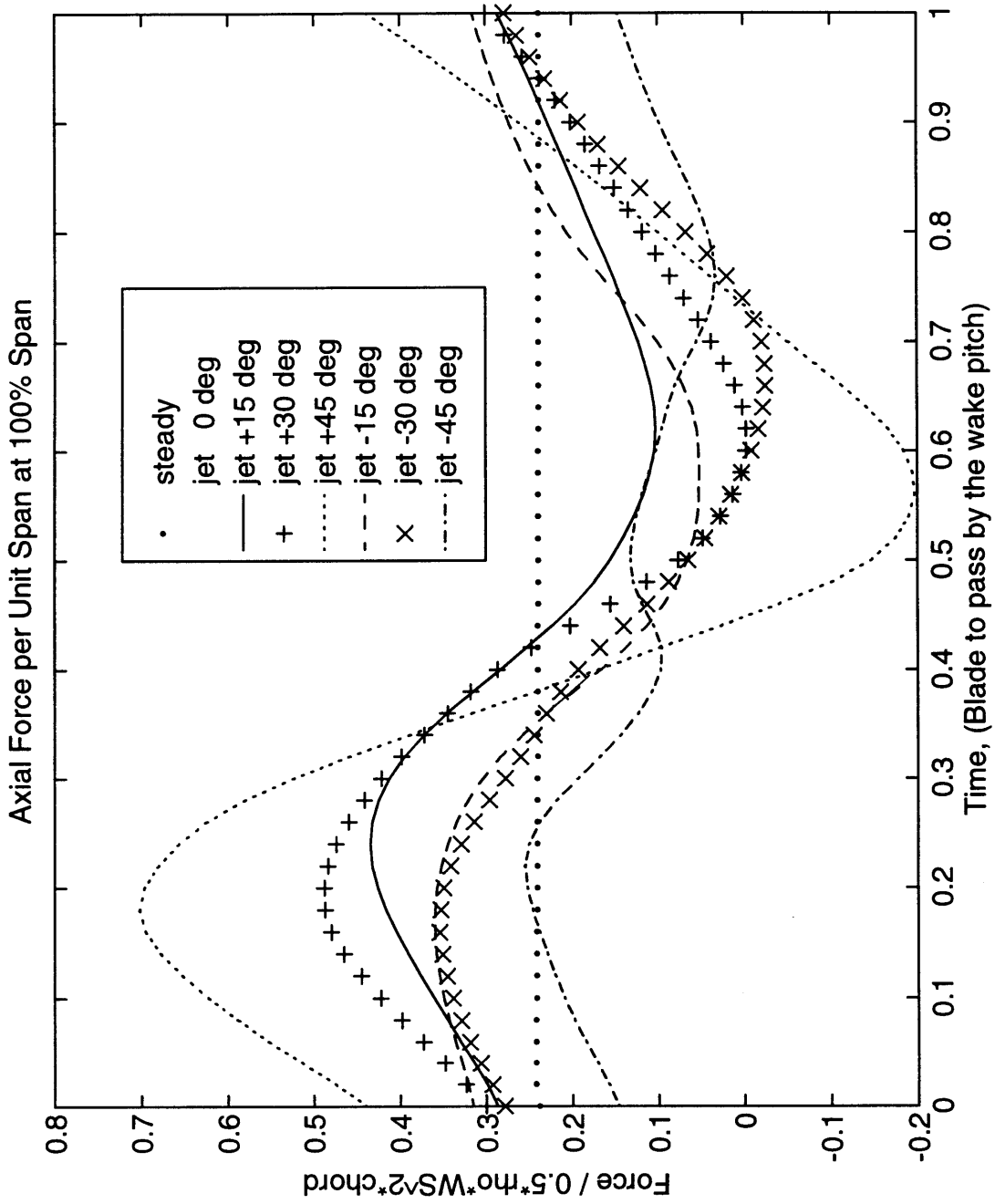

Figure D.8: Axial Force at a radial position of 100% span and a jet velocity equal to 2 times the free-stream velocity

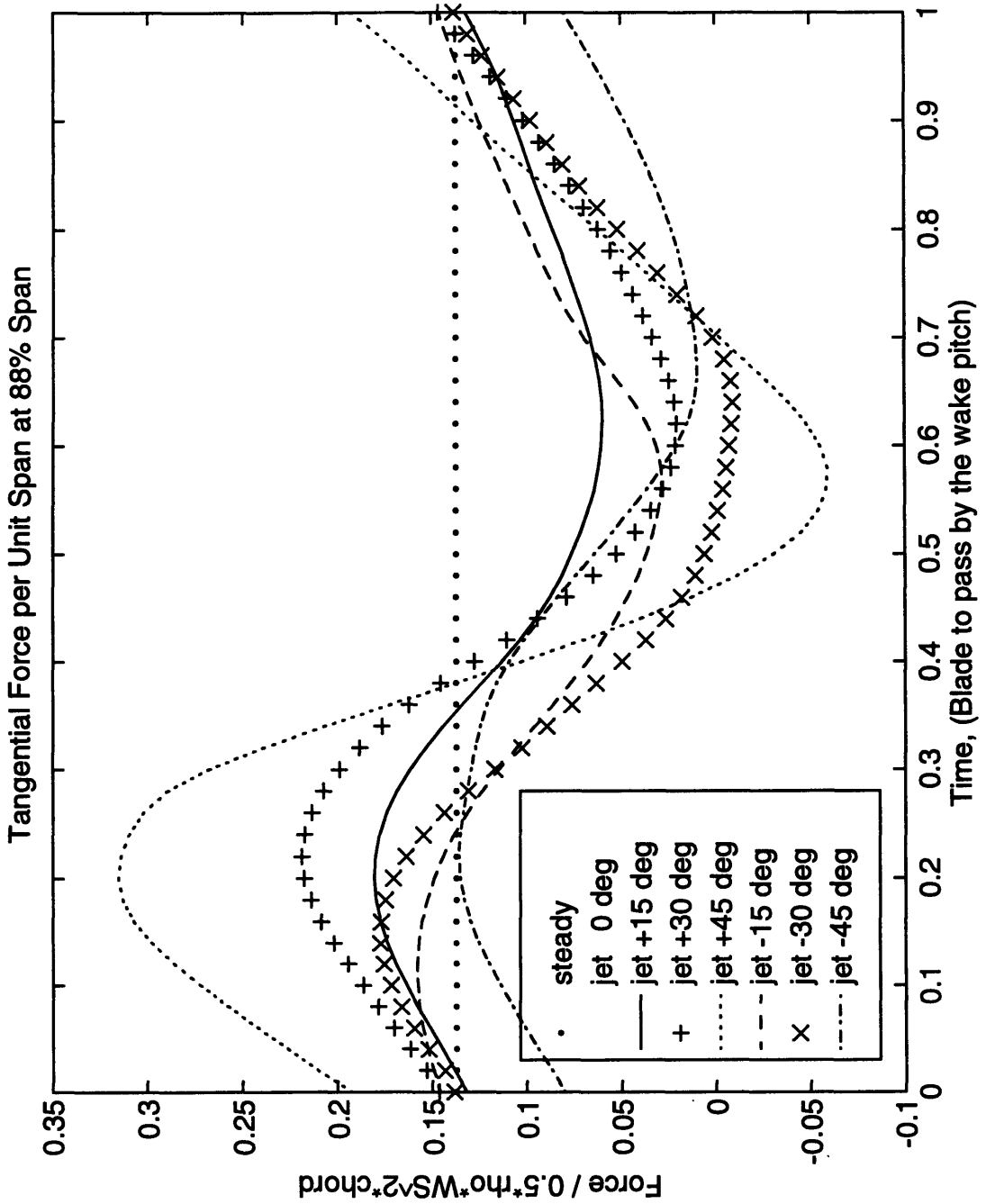

Figure D.9: Tangential Force at a radial position of 88% span and a jet velocity equal to 2 times the free-stream velocity

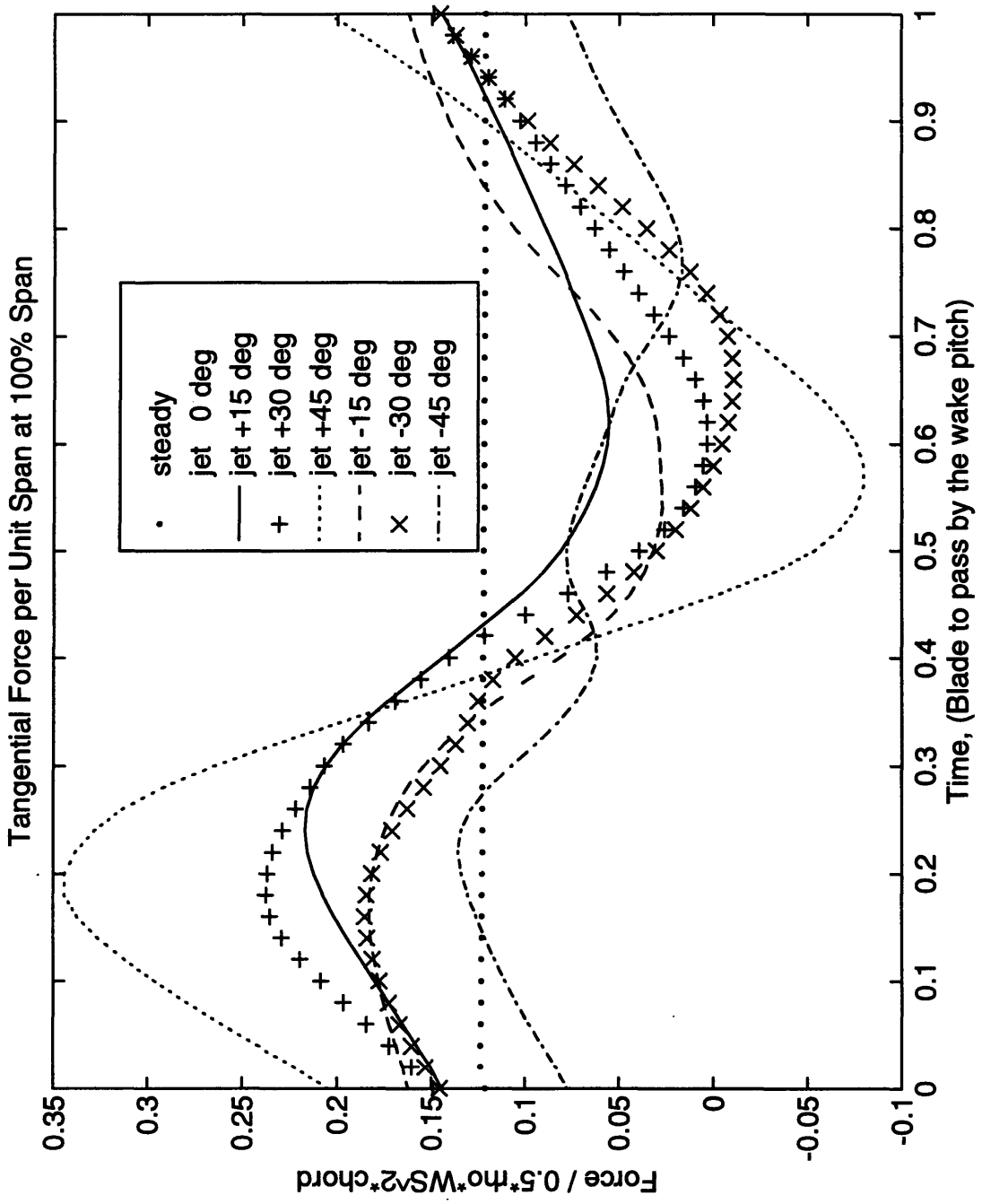

Figure D.10: Tangential Force at a radial position of 100% span and a jet velocity equal to 2 times the free-stream velocity

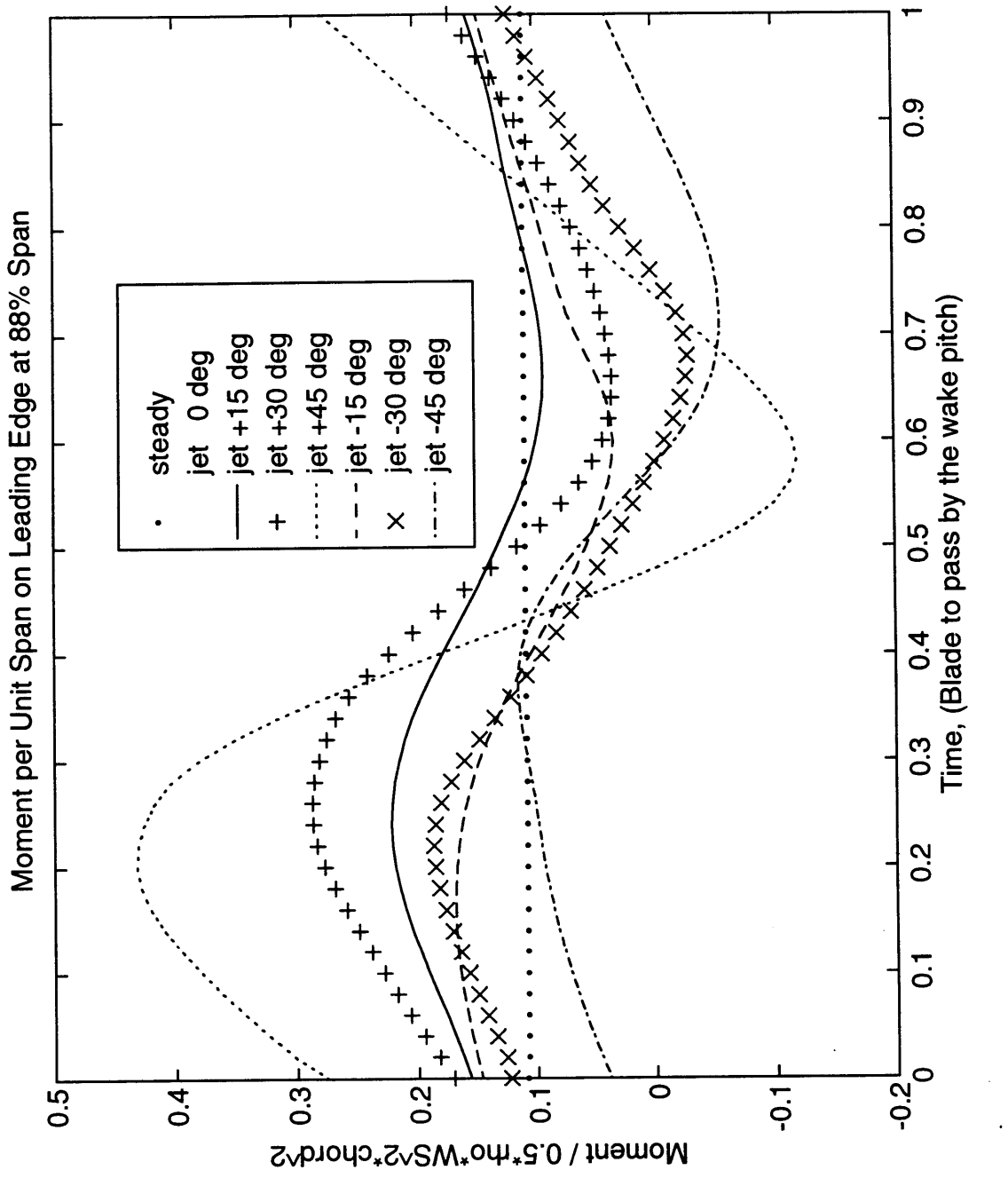

Figure D.11: Moment at a radial position of 88% span and a jet velocity equal to 2 times the free-stream velocity

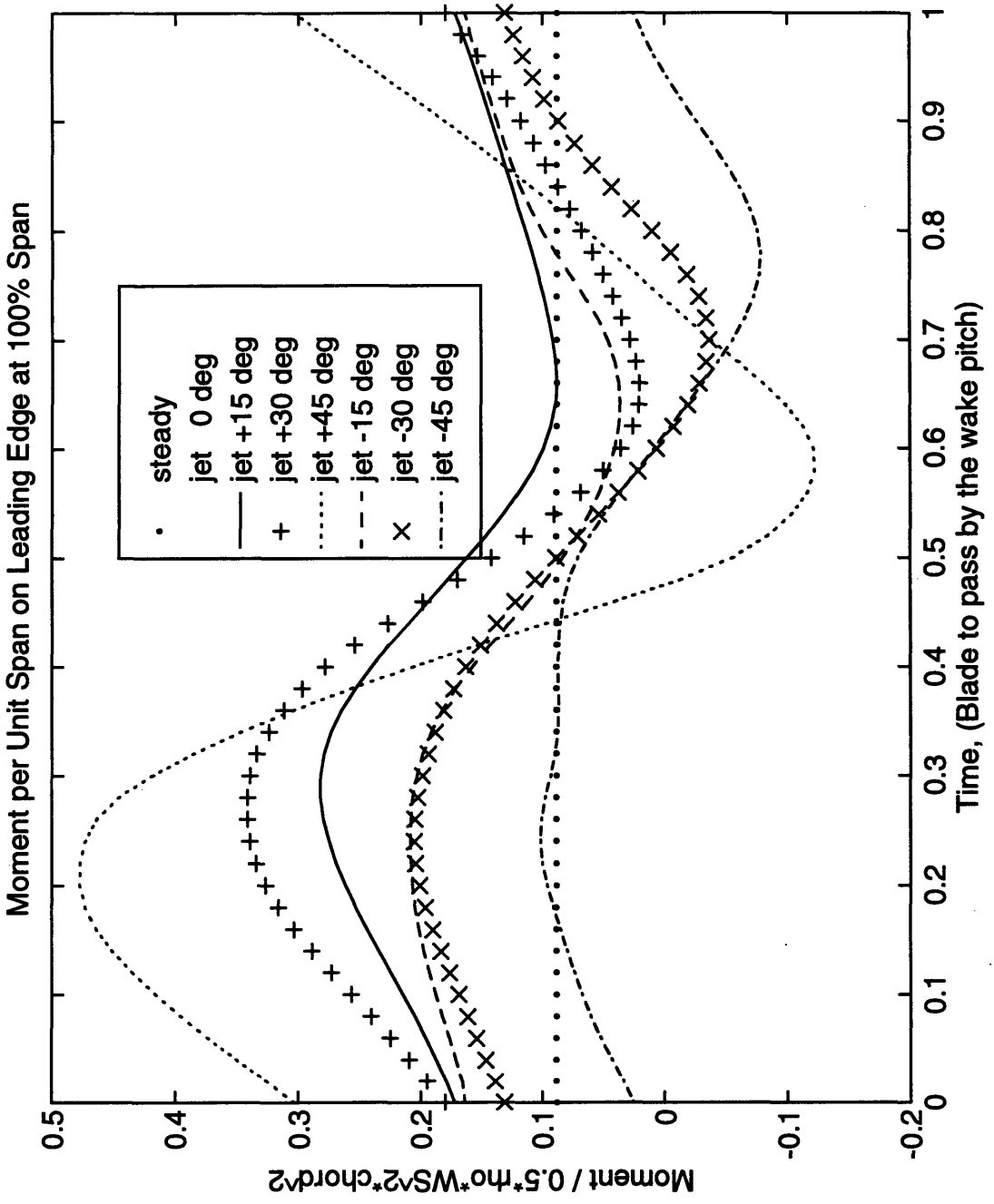

Figure D.12: Moment at a radial position of 100% span and a jet velocity equal to 2 times the free-stream velocity